DIPLOMARBEIT

Titel der Diplomarbeit

Akquisitionsdesign für die seismische Erkundung des tiefen Wiener Beckens auf Basis eines 3D-Untergrundmodells

angestrebter akademischer Grad

Magister der Naturwissenschaften (Mag. rer. nat.)

Verfasser:	Martin Fuchsluger
Matrikel-Nummer:	0503584
Studienrichtung	A416
Betreuer:	O. Univ. Prof. Dipl.-Ing. Dr. Ewald Brückl Institut für Geodäsie und Geophysik Technische Universität Wien

Wien, im Februar 2011

ZUSAMMENFASSUNG

Unterhalb der neogenen Sedimentschichten des Wiener Beckens befinden sich in circa drei bis sieben Kilometer Tiefe die nördlichen Kalkalpen der vorneogenen Alpin-Karpatischen Überschiebungsdecken. Durch einige tieferreichende Bohrungen wurden bereits wirtschaftliche Mengen an saurem Erdgas erkundet. Ein seismisches Abbild der komplexen Untergrundstrukturen ist sowohl für die Kohlenwasserstoffindustrie als auch für die genauere Erforschung der Alpen- und Beckenentwicklung von großem Interesse. Die Reflexionsseismik wird hier sicherlich gefordert sein, wodurch eine zielgerichtete Akquisition notwendig ist.

Diese Arbeit hat das Ziel, die wichtigsten Akquisitionsparameter mit Hilfe einer modernen Akquisitions- und Modellierungssoftware zu bestimmen, wobei ein dreidimensionales strukturelles Modell vom Zielgebiet zur Verfügung steht. Dieses Modell beinhaltet die seismischen Intervallgeschwindigkeiten und die Dämpfungen (Q-Werte).

Drei wichtige Horizonte, die vom Boden des Beckens in circa 3 Kilometer Tiefe bis zur Basis der Kalkalpen in ca. 6-7 Kilometer Tiefe reichen, werden analysiert und die wichtigsten Akquisitionsparameter berechnet und diskutiert. Die Parameter sind dabei: Bin Größe, maximale Frequenz, minimaler und maximaler Offset, horizontale und vertikale Auflösung, Amplitudendämpfung, Migrationsapertur, Stations- und Linienintervall sowie maximale Aufnahmezeit und zeitliches Samplingintervall.

Ein weiterer Schwerpunkt liegt in der, auf Ray-Tracing basierenden, Illuminationsanalyse. Dafür muss das Geschwindigkeitsmodell mit Schichten konstanter Geschwindigkeit approximiert und somit neu gebildet werden. Die Ray-Tracing Optionen der Software werden getestet und mit einem gut erprobten Ray-Tracing Algorithmus verglichen. Durch einen Kompromiss von Rechenzeit und Genauigkeit werden die optimalen Einstellungen ermittelt und eventuelle Limitationen festgestellt. Das Ergebnis wird schlussendlich verwendet, um die notwendige Auslagegeometrie

und somit den notwendigen maximalen Offset zu ermitteln damit die Kosten für eine Umsetzung minimiert werden.

Im Auftrag der OMV

3D model based acquisition design for the seismic exploration of the deep Vienna Basin

ABSTRACT

Beneath the *Neogene Basin Fill* of the Vienna Basin the *Northern Calcareous Alps* of the *Pre-Neogene Alpine-Carpathian thrust sheets* appears at about three to seven kilometer depth. Some deep wells have already delivered profitable amounts of sour gas. A seismic image of the complex subsurface structure is therefore of great interest for the hydrocarbon industries, as well as for a more detailed understanding of the development of the basin and the Alps. Due to the deep lying, complex-folded thrust sheets, the standard seismic reflection method will likely reach its limit. Therefore a target-orientated acquisition design is necessary.

One objective of this work is to determine the most important acquisition parameters with the aid of a modern acquisition and modeling software. From a preceding thesis a three dimensional subsurface model of the investigation area is available, including the seismic interval velocities and attenuation for different two way travel times.

Three main horizons are selected, reaching from the *Neogene Basin Floor* at about three kilometer depth to the base of the *Pre-Neogene Alpine-Carpathian thrust sheets* at about six to seven kilometer depth. The three horizons are analyzed and important acquisition parameters are determined and discussed. These parameters are bin size, maximum frequency, minimum and maximum offset, vertical and horizontal resolution, attenuation, migration apron, station and line interval, as well as maximum recording time and temporal sampling interval.

A further objective is to calculate the illumination of the horizons, which is based on ray tracing. For applying the illumination analysis the subsurface model has to be rebuilt and thus approximated with layers of constant velocities. The ray tracing options of the software are tested and compared with a well proven algorithm.

Accepting a compromise between calculation time and accuracy the best adjustments for this work are determined and unavoidable limitations are detected. Finally the result is used to determine the required pattern size and hence the minimal required maximum offset, which can help decreasing the survey costs.

An Investigation conducted on behalf of OMV

OMV

ACKNOWLEDGEMENT

I want to thank OMV Exploration & Production and the Vienna University of Technology for providing and supporting me with this topic. Special thanks go to Mag. Werner Chwatal for mentoring me in technical and linguistic challenges and to Dr. Christian Stotter and Dr. Roman Spitzer for guiding me through the practical work. And of course, I am grateful, to the supervisor of this project: Prof. Dr. Ewald Brückl.

TABLE OF CONTENTS

1 INTRODUCTION AND MOTIVATION

For imaging the deep buried structures of the *Northern Calcareous Alps* beneath the *Neogene Basin Floor* of the Vienna Basin it is essential to design a target oriented three dimensional (3D) seismic acquisition configuration. A detailed acquisition design is the key to success of any seismic survey, especially in complex geology such as the *deep Vienna Basin.* Therefore OMV has initiated a technology project to investigate this matter. The study was separated in two parts. In the **first part** of the project Stefan Pfeiler has constructed a comprehensive structural/geophysical model, which includes the seismic velocity and attenuation and is based on the preliminary understanding of geological structures in the basin.

The **second part** of the study, which is described in this thesis, uses this model to find out several key parameters to design a suitable acquisition design. Moreover three dimensional ray tracing is applied on the subsurface model to get the illumination (migrated fold) of the deeper horizons. This analysis works with ray tracing and should determine the dimension of the seismic survey as well as the maximum required offset. The ray tracing algorithm of the used software is analyzed and compared with a well known algorithm, thus the optimal options for the computationally intensive ray tracing will be determined.

This introducing chapter describes 3D survey design in general, gives some selected references for relevant works in seismic acquisition and talk about previous seismic projects in the investigation area. Further the possibilities, challenges and motivation for imaging the deep Vienna Basin are discussed.

Chapter 2 gives an overview of the development and the geology of the Vienna Basin with focus on the investigation area.

In chapter 3 important 3D seismic terms are defined and the acquisition parameters are treated theoretically and discussed.

Chapter 4 starts with the *wave equation* and derives the *first* and *second ray tracing equation* with the aid of the *Eikonal equation*.

In chapter 5 the available data and used software tools are presented in detail.

Chapter 6 and 7 are the practical parts of this work, where the parameters are determined and ray tracing is applied to get the illumination of the selected horizons.

Finally, the conclusion is presented in chapter 8.

1.1 3D SURVEY DESIGN IN GENERAL

To determine the parameters of a seismic survey design at first all available underground information about the investigation area has to be collected. Primarily some velocity and frequency information of the subsurface is required. These can be information from wells, like sonic logs or VSP data, or information from an already existing seismic data in two or three dimensions. Also available geologic information from other geophysical exploration in the investigation area, e.g. gravimetric, geo-electric, magnetic or electromagnetic results can deliver suitable information for the seismic acquisition. In general, more geologic information leads to a more detailed acquisition work and hence to a more successful seismic investigation.

Sonic logs deliver one dimensional velocity information and may be sufficient for a survey design in horizontal layered geology. The more sophisticated the subsurface geology is expected, the more geologic information is required and some pre-measurements, e.g. a seismic 2D-line or VSP (vertical seismic profiling) may be necessary.

The implementation of a large 3D survey is associated with high costs. For example: A dense spatial sampling interval of the sources and receivers increases the recorded data quality, but also the survey costs. The business of acquisition work is survey planning and optimizing it to obtain sufficient data quality with minimized survey costs. Hence, it is always a compromise, between the expectations of the interpreter and what the budget will permit.

1.2 HISTORY OF 3D SEISMIC AQUISITION

In the following some selected references, which should show the technical development of acquisition techniques in the last decades, are mentioned:

LASTER, 1985 gives a view of the state of seismic data acquisition in 1985. He makes a brief review of the techniques of the mid-1980s, where the increasing number of data channels leads to the development of digital telemetry systems. He discusses shear wave information and sees a distinct trend to three dimensional seismic acquisition and recording.

SAVIT, 1989 makes a public-opinion poll to all SEG members, who use seismic data acquisition equipment. The practical number of simultaneous recordable channels is about 400.

ASHTON et al., 1994 deals with 3D seismic offshore survey design and integrates borehole data to survey simulation in three dimensions and compares increased acquisition costs by decreased survey costs.

VERMEER, 1998 invents a comprehensive theory to define what constitutes a good 3D geometry and how it can be designed. He calls this theory *3D symmetrical sampling* which is an extension of his *2D symmetrical sampling* criteria: equal shot and receiver intervals, and equal shot and receiver patterns.

LINER et al., 1999 extends the formula of bin size and related parameters designed for constant velocities to media with linear, with depth increasing velocity.

QUIGLEY, 2000 makes some exploration scenarios onshore in Abu Dhabi, by improving spatial distribution of the source energy which yield to an increased CMP fold and an improved offset distribution in respect to survey costs.

CORDSEN et al., 2000 imparts the tool to start planning a 3D seismic survey considering practical aspects.

VERMEER, 2003 describes an optimization of three dimensional seismic survey design in case of an orthogonal geometry.

ALVAREZ et al., 2004 deals with model-based three dimensional survey design. He shoots rays from different grid points on the target reflector and shows, that it's possible to reduce the number of sources considerably to get affordable results.

COOPER, 2004 published a tutorial in two parts: "Designing land 3D programs for signal, noise, and prestack migration", focusing on bin size and he strongly encourages the use of prestack migration and midpoint scatter.

GALBRAITH, 2004 introduces a new methodology for 3D survey design by taking well logs to determine the maximum receivable frequency and VSP data to estimate attenuation. Hence, parameters as S/N ratio, the required fold, bin size, minimum and maximum offset can be determined. At the end some field tests are performed to achieve the final parameters.

XIE et al., 2006 and 2008 shows a new method for a full-wave-equation-based seismic illumination by using the full-wave finite difference method.

1.3 PREVIOUS SEISMIC INVESTIGATIONS IN THE VIENNA BASIN

Several previous investigations in the Vienna Basin, made by OMV, yield to a good image of the *Neogene Basin Fill* down to the *Neogene Basin Floor* at about three to four kilometer depth (detailed geology see chapter 2). These seismic surveys were subdivided in several projects and all together cover nearly the whole Austrian part of the basin. The surveys were carried out in the 1980`s, when three dimensional surveys were in their infancy and the maximum number of active receivers was about 500. At this time it seemed impossible to image structures of the *deep Vienna Basin*, but nowadays the technique has developed, the maximum number of simultaneously recordable traces are up to 10000 or even more, computer power has increased and data processing has new techniques and possibilities.

In 2007 a 2D line with three component geophones was tested in the Vienna Basin, which has demonstrated the possibility of achieving signals from the deep basin.

1.4 MODEL BASED SURVEY DESIGN

The provided velocity model, which has been constructed in the first part of the project by Stefan Pfeiler, contains all available information of the investigation area combined in a three dimensional velocity and Q-value model. The model includes the first floor (*Neogene Basin Fill*) and the second floor (*Pre-Neogene Alpine-Carpathian thrust sheets*) of the investigation area, located in the Vienna Basin (see chapter 2).

For the first floor subsurface information from previous three dimensional seismic explorations (PSDM[1] and CRS[2] velocity fields) and from well data is available, thus the first floor has detailed velocity information and represents real underground structure very well.

The second floor, the real target of the seismic survey, is mainly based on some deep reaching wells and on the preliminary understanding of the geological structures. Especially the deep nappes, e.g. the *Base of the Calcareous Alps (BaseNCA)* and the base of the *Giesshübl Monocline* (see chapter 2.3) are partly estimated.

1.5 CHALLENGES IN THE DEEP VIENNA BASIN

Imaging the deep steep events beneath the *Neogene Basin Floor* (geology details see chapter 2) is certainly a challenge. The amplitude of the source signal will be reduced significantly on its way to the receiver and may be hard to be separated from noise. It can be expected that there is the need of big offsets, where the reflection events are out of the ground roll cone, which allows proper migration of the steep events.

Simultaneously the spatial sampling should be as small as possible to record small wavelengths and respectively big wavenumbers. Thus the ground roll (surface waves) is fully recorded, spatial aliasing is avoided and can be filtered out in seismic processing afterwards.

---

[1] Pre Stack Depth Migration

[2] Common Reflection Surface

On the other hand the high frequency content of the source signal will likely get lost on the long journey through the rocks. This will lead to a narrow frequency spectrum, which lowers resolution and will result in a more blurred image.

All these factors lead to the need of a more sophisticated acquisition work. So this work will focus on software developed in the recent past to find out the possibilities, limitations and benefits of three dimensional, model based survey design.

1.6 OBJECTIVES

A primary aim of this work is to determine several key parameters, like spatial sampling interval, vertical and horizontal resolution, maximum achievable frequency, the minimum and maximum offset, attenuation and migration apron with the aid of the provided 3D velocity model. The further purpose of this model-based survey design is to illuminate and image selected horizons of the model in an optimum way by using ray tracing. A good result of illumination is therefore dependent on the used ray tracing algorithm and also the time factor for the calculation may play a major role. This work will focus on the possibilities of 3D survey design by using GEDCO`s software "OMNI - 3D survey design and modeling". Especially the ray tracing based illumination analysis is studied, tested and compared to get the optimal adjustments.

2 GEOLOGY OF THE VIENNA BASIN & THE INVESTIGATION AREA

This chapter describes the Vienna Basin, its geographical location and its tectonic and stratigraphic development. Further, the area of investigation is defined and a short description of hydrocarbon resources in the basin will be provided.

2.1 GEOGRAPHY

The Vienna Basin, which is embedded between the *Eastern Alps*, the *Western Carpathians* and the western part of the *Pannonian Basin*, was formed rhombohedral due to a pull-apart mechanism (ROYDEN, 1985; WESSELY, 1988). It ranges from *Gloggnitz* in Lower Austria (SSW) to *Napajedla* in Czech Republic (NNE) and has an extension of about 200 km length and max. 50 km breadth. The main part is located in Austria with a smaller Czech-Slovakian part. From north to south the eastern margin of the Alps (*Waschberg Zone, Greywacke Zone, Northern Calcareous Alps, Flysch Zone, Central Zone*) build the border to the basin. The four hills *Rosaliengebirge, Leithagebirge, Hainburger Berge* and the *Little Carpathian Mountains* borders from South over East to North. All four hills belong to the *Alpine-Carpathian Central Zone*. The Hainburger Pforte (also known as Bruckner Pforte, like in Figure 2-1) in the SE connects the Basin with the *Little Hungarian Basin* and the *Wiener Neustädter Pforte* builds the connection to the *Eisenstadt Basin*, which can be considered as a sub-basin of the *Vienna Basin* (PILLER, 1999).

2.2 TECTONIC AND STRATIGRAPHIC DEVELOPMENT

The following geological features are mainly described after KRÖLL, 1980 and HAMILTON et al., 2000.

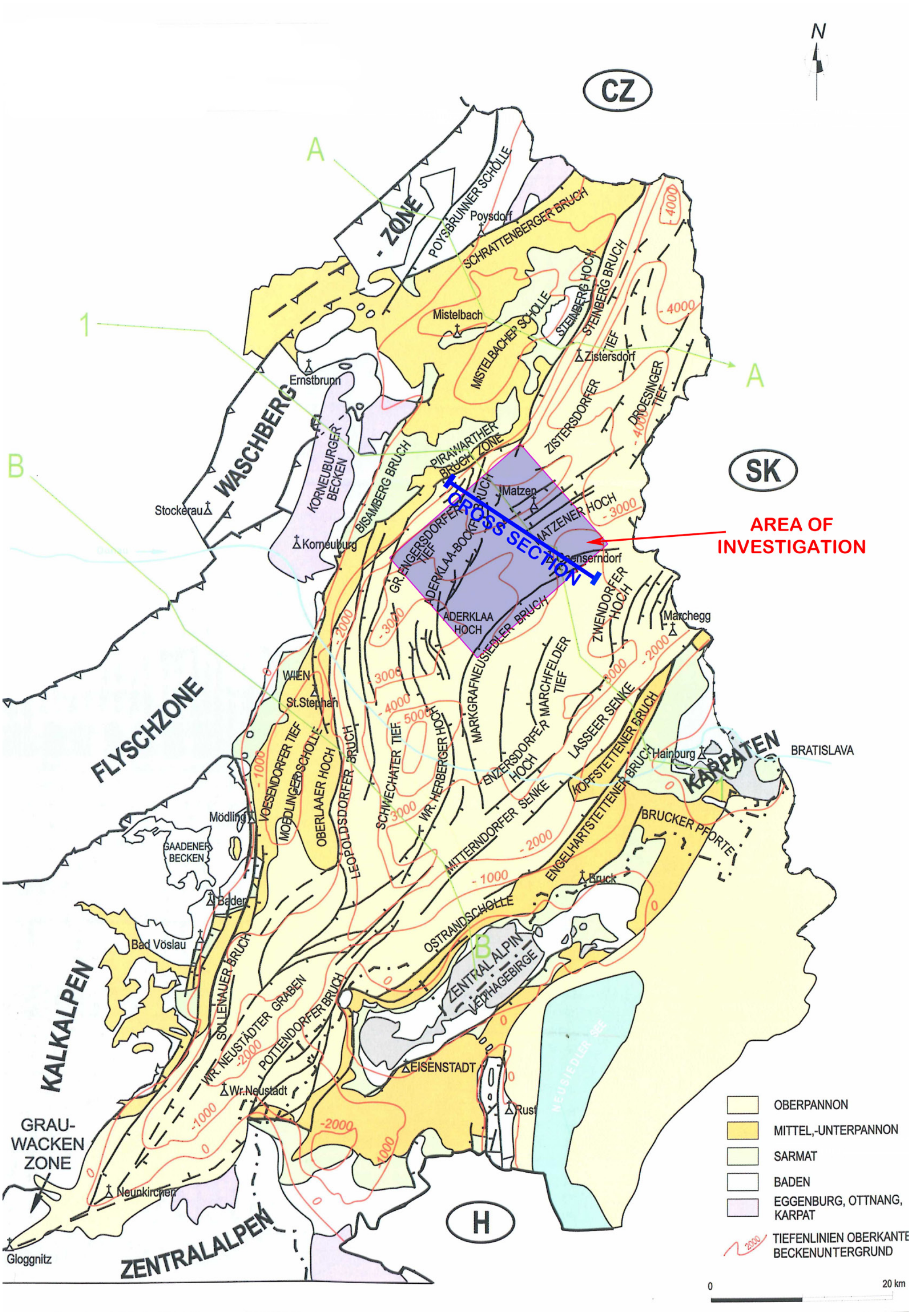

Figure 2-1: Surface geology map of the Austrian part of the Vienna Basin [WESSELY et al., 2006, mod.] The red lines are iso-depth lines of the Neogene Basin Floor, the blue rectangle is the investigation area, the blue line is the cross section shown in Figure 2-3 and the black lines are the main fault.

In general, the Vienna Basin can be vertically parted in the following three geological main floors:

Floor 1: the **Neogene Basin Fill**

Floor 2: the allochthonous **Pre-Neogene Alpine-Carpathian thrust sheets**, and

Floor 3: the autochthonous **basement**

The *Alps* and the *Carpathians* were formed due to tectonic movements of the *African plate* against the *European plate*. This process began in the late *Jurassic* period (150 million years ago) and ended in the early *Neogene* period about 15 to 20 million years ago. At the end of this process the Alps and Carpathians built a continuing unit, so they were not separated. Then the pull-apart mechanism began which resulted in a great subsidence of the allochthonous Alpine-Carpathian thrust sheets. At this time the *Paratethys* and the *Mediterranean Sea* was already formed after the *Tethys* was vanished. The areas under sea level were flooded by the *Paratethys*, which was more or less isolated from the *Mediterranean Sea*, hence a regional stratigraphic stage system was established (RÖGL & STEININGER, 1983; STEININGER et al., 1990; RÖGL, 1996; Fig 14). For the Vienna Basin the *Central Paratethys Stages* are used (see Figure 2-2). The oldest sediments in the northern Vienna Basin are from *Eggenburgian - Ottnangian*, the pull-apart mechanism began in *Karpatian* and the upper layers of the basin were sedimented in *Badenian, Sarmatian* and *Pannonian* Stage (PILLER, 1999). All these sediments were deposited in the *Neogene* period, that's why they are called *Neogene Basin Fill.*

Many faults occurred during the pull apart and sedimentation process, which are also mapped in Figure 2-1, and they are mainly orientated southwest to northeast. The most impressive faults are on the northwestern border of the Vienna Basin: *The Steinberg fault* and the *Leopoldsdorfer fault* with a vertical displacement up to six kilometers.

The significance of the subsidence can be concluded from the thickness of the *Neogene Basin Fill*, which is up to 5500 m in the "*Schwechater Tief*" (see Figure 2-1).

The *Pre-Neogene Alpine Carpathian thrust sheets* are geologically completely different from the *Neogene Basin Fill*. The deposits are much older and were mainly sedimented in the *Mesozoic* period, thus they have a different facies. The adjacent Alps in the west of the basin consists of several geological units: The *Flysch zone ("Flysch Zone")*, *Calcareous Alps ("Kalkalpen")*, *Greywacke zone ("Grauwackenzone")* and *Central Alps ("Zentralalpen")*, see Figure 2-1. These zones cross the basin in the subsurface, under the *Neogene Basin Fill*, and partially arise to the surface in the *Western Carpathians*. The units were displaced by tectonic forces from their place of deposit (allochthon). Inside of the units thrust faulted nappes are characteristic in the Vienna Basin.

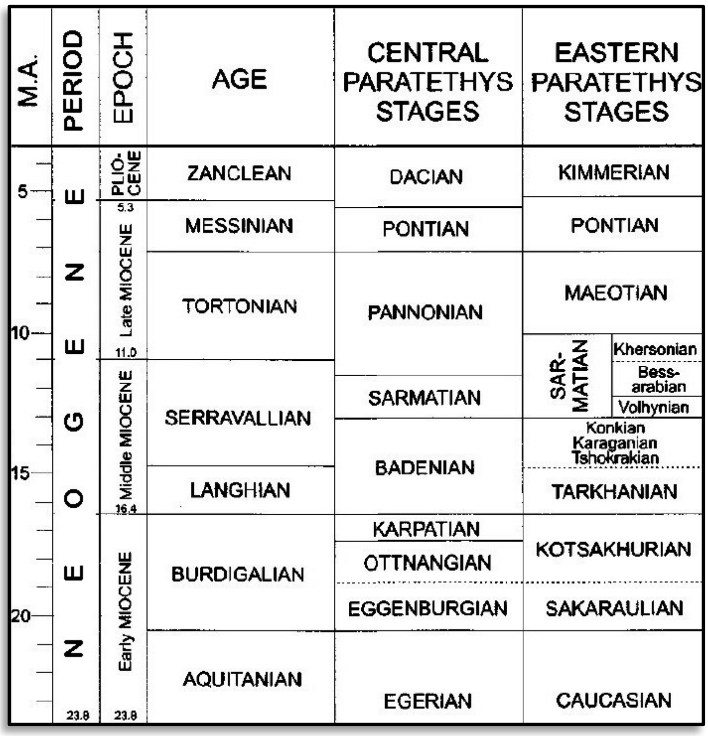

Figure 2-2: Chronostratigraphy of the Neogene Basin Fill (PILLER, 1999, mod.). The oldest sediments in the northern Vienna Basin are from Eggenburgian - Ottnangian. The pull-apart mechanism began in Karpatian. The upper layers of the basin were sedimented in Badenian, Sarmatian and Pannonian stage.

The third floor of the Vienna Basin is the *autochthonous basement*, including the crystalline *bohemian massif*, the *Mesozoic* cover and the tertiary *Molasse* below the *Alpine-Carpathian thrust sheets*.

2.3 THE INVESTIGATION AREA

Figure 2-1 shows the geographical location and Figure 2-3 a cross section of the investigation area.

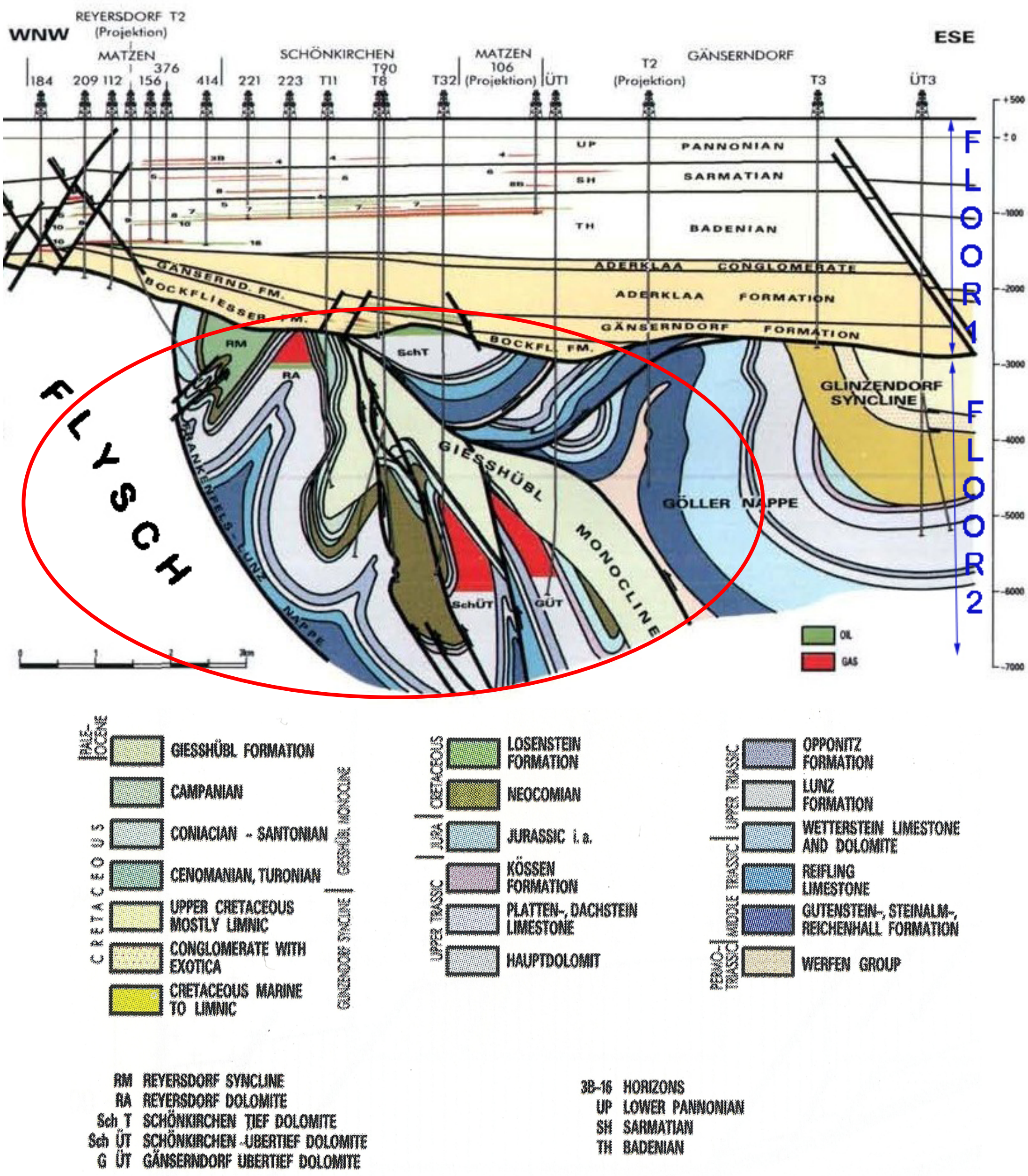

Figure 2-3: Cross section (HAMILTON et al., 2000, mod.) through the investigation area (red circle) in the deep Vienna Basin at the blue line in Figure 2-1.

The investigation area is part of the second floor of the Vienna Basin and includes the *Flysch Zone* and the *Northern Calcareous Alps*. The complex folded nappes of the *Northern Calcareous Alps*, e.g. the *Frankenfels-Lunz* nappe as the border to *Flysch*, the

Giesshübl Monocline, the dolomitic *Schönkirchen* nappe (SchT), the *Reyersdorf dolomite* (RA) and the *Göller* nappe are imaged. Moreover, some known oil and gas fields are illustrated in the first and second floor.

In the following some terms are defined, which are often used in this work: The term *Neogene Basin Floor* is used for the Bottom of the *Neogene Basin Fill*. The seismic main target in this work are the *Northern Calcareous Alps* (part of the second floor of the Vienna Basin in the investigation area - without the *Flysch zone*) and is also called *deep Vienna Basin*. The bottom of the second floor is called *BaseNCA* (Base of the *Northern Calcareous Alps).*

In Figure 2-4 the investigation area, some deep wells and the seismic 2D line, used for frequency information, are located within a satellite image.

Figure 2-4: Location overview; symbol for deep wells: ⊙

2D seismic line in red; the black rectangle is the contour of the velocity model; views in 3D are from north east

2.4 HYDROCARBONS IN THE VIENNA BASIN

Hydrocarbons can be found in all three floors of the Vienna Basin. The *Neogene Basin Fill* holds the main part of multi-horizon oil/gas fields, where the field of *Matzen* is the most productive (NACHTMANN, 2007). The *Pre-Neogene Alpine-Carpathian Thrust Sheets* include reservoirs of thick upper *Triassic* dolomites *("Hauptdolomit")* and dolomitic limestone (e.g. *Dachstein Limestone*). The traps for the hydrocarbons range from flat to very steep, e.g. in the *Schönkirchen* nappe, where vertical gas columns of several hundred meters were found (WESSELY, 1999 and HAMILTON et al., 2000).

From the seismic measurements in the 1980's there is already a good image of the *Neogene Basin Fill*. After OMV has found some important gas resources beneath the Neogene Basin Floor (e.g. well *"Straßhof T4",* April 2005 and well *"Ebenthal T1"* December 2005, produces gas from dolomite layers of the Calcareous Alps) the question of the feasibility of a big 3D seismic project arised to get a good image of the structures of the second floor.

3 DEFINITION OF IMPORTANT 3D TERMS

In this chapter the most important terms of three dimensional seismic are firstly defined and then parameters, which are important for the acquisition, are described. Moreover the equations to determine the parameters in chapter 6 are defined and discussed.

3.1 DEFINITION OF TERMS

Designing a 3D survey implies the right layout of receivers and sources in the field. There are several different layout geometries (orthogonal, areal, parallel, zigzag, slanted). The most common one is the orthogonal survey, where the receivers are plugged in lines over the measuring area and the source lines are orthogonal to them (see Figure 3-1). VERMEER, 2002 discusses the different layout geometries and states: *"In general, the orthogonal geometry is the geometry of choice for land data".*[3]

The direction of the receiver line is called *inline* and the direction of source line is called *crossline*. In orthogonal geometry all shot-receiver azimuths are present.

In the following tables the main terms are defined and described.

Term	**Description**
Receiver Line Interval (RLI)	Distance between two receiver lines
Receiver Interval (RI)	Distance between two receivers (inline)
Source Line Interval (SLI)	Distance between two source lines
Source Interval (SI)	Distance between two source stations (crossline)

For common practice $RI = SI$ and $RLI = SLI$, otherwise unsymmetrical effects can be a disadvantage in processing (see chapter 4.4).

---

[3] (VERMEER, 2002, p.69, chapter 4.1)

Term	**Description**
CMP, CDP	A *CMP (Common Mid Point)* is the geometrical midpoint of a source-receiver pair at the surface. A *CDP (common depth point)* is the reflection point on a layer in the subsurface for one source-receiver pair. The CMP is directly above the CDP for a horizontal layer, but not for a dipping layer. Migration moves the CMP of a source-receiver pair to the CDP.
bin, **bin size (B)**	The area of the orthogonal survey is partitioned in *bins* (respectively CMP bin in Figure 3-1), which size is dependent on source- and receiver interval $[(RI/2) \times (SI/2)]$. One length of this area is called *bin size* (precondition: $RI = SI$).
grid node **grid bin** **grid bin size**	A digitized layer in the subsurface has to every (x, y) - pair one z value with a constant $x - y$ raster. The distance between the *grid nodes* is called *grid bin size* and the enclosed area between four neighbored *grid nodes* is called *grid bin.*
fold **migrated fold**	Every source-receiver pair has one CMP. The number of CMPs, which fall in one bin is called *fold* (in literature also *fold of coverage* or *stacking fold*). The number of CDPs, which are falling in one *grid bin,* is *called migrated fold* (or *illumination*), e.g. if 20 points fall in one bin, this bin has a fold of 20. All recorded traces with the same CMP are stacked in seismic processing, and the higher the fold, the better is the S/N (signal to noise) ratio.

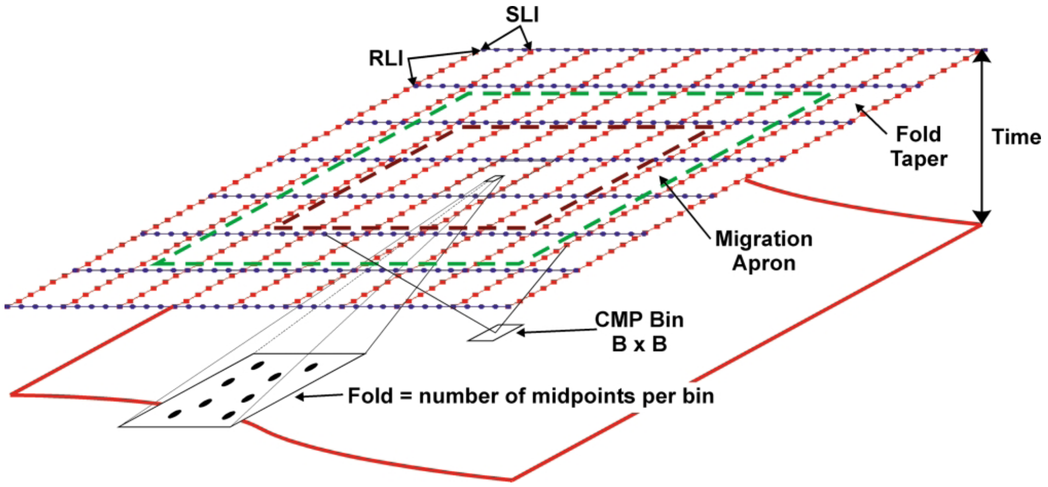

Figure 3-1 (CORDSEN et al., 2000): Bin size B of one CMP bin, fold, migration apron and fold taper of an orthogonal 3D survey

Term	Description
nominal fold, **migration apron,** **fold taper**	In an orthogonal survey the bins on the edges have low fold. From a specific fold the S/N ratio[4] will be high enough for the interpreter. This fold is called *nominal fold*. In Figure 3-1, the inner dotted box is the area of interest and can be interpreted after seismic processing. To allow proper migration of this area, the survey has to be extended to the green dotted line. This extension area is called *migration apron*. To ensure, that all bins in the green area of Figure 3-1 has the *nominal fold*, and hence a sufficient S/N ratio, the survey area has to be extended further. This extension area is called *fold taper*.
migration aperture **migration angle**	The *migration aperture* is defined as the distance (offset) on the surface, which will be essential for proper migration (e.g. collapsing the diffraction curve to the minimum wavelength). Usually a *migration angle* of 30° is sufficient to record 95% of the reflection energy of the diffraction point. The migration aperture is therefore larger for greater depths.
pattern, **all live pattern**	All receivers, which are active (live) for a given shot and which are recording data, belong to a *pattern*. The dimension of a pattern can be e.g. 10 x 200 and stand for 10 receiver lines with 200 channels per line are active per shot. This pattern is normally "travelling" in line steps over the whole survey. By default, the active shot is in the middle of the pattern (called split spread in 2D). If all receives of the survey are active for each shot the pattern is called *all live pattern*. This kind of pattern is for theoretical considerations. Therefore in praxis many receivers are required and the survey costs are exploding. On the other hand a small pattern dimension generally leads to a small maximum offset and hence to a shallow depth that can be imaged.

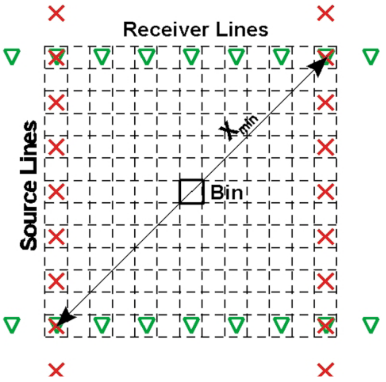

Figure 3-2 (CORDSEN et al., 2000): A box with definition of bin and X_{MIN}. The red crosses are shot points and the green rectangles receiver stations.

---

[4] The S/N ratio can also be improved by vertical stacking or with multiple/stronger sources, see ch. 3.3

Term	Description
box	The area, which is enclosed between two receiver lines and two source lines is called *box*. Hence, one box has an area of RLI x SLI and is illustrated in Figure 3-2.
minimum offset (X_{MIN})	In literature it is also called the *largest minimum offset (LMOS)* and is defined as the largest offset of a box (see Figure 3-2). Its size depends on the line spacing and corresponds approximately to the depth of the shallowest event that wants to be imaged.
maximum offset (X_{MAX})	The maximum offset (maximum distance of a source receiver pair) of a survey depends on the dimension of the pattern and the shooting strategy. Usually (the shot points are in the middle of the pattern) it is half of the diagonal of the pattern size and corresponds approximately to the depth of the deepest event that wants to be imaged.

3.2 BIN SIZE AND SPATIAL SAMPLING

The *bin size* is controlled by RI and SI and since they have same size the *bin* has a quadratic form. RI and SI define the spatial sampling interval, which is one the most important factors in a seismic survey. RI and SI are determined in acquisition and cannot be repaired in processing time, in case they are too large. A small receiver and source interval is an advantage in any case for the seismic data quality but effects the survey costs significantly (EBROM et al., 1995).

Three factors control the bin size (after CORDSEN et al., 2000):

- target size
- lateral resolution and
- maximum unaliased frequency due to a dipping reflector

First the bin size with all three factors must be calculated: As one third of the desired lateral *target size* or as same size as the *lateral resolution* or to get the maximum achievable frequency without spatial aliasing with formula (3.2). Then the factor, which is giving the smallest value, dictates the final bin size for the survey.

In most literature only the third factor is seen as the crucial one. Further some tests in the investigation area (the deep Vienna Basin) have confirmed that the *maximum unaliased frequency* is giving the smallest bin size. Hence, in the following, the factor to record the maximum achievable frequency in respect to a dipping reflector, without spatial aliasing, is discussed.

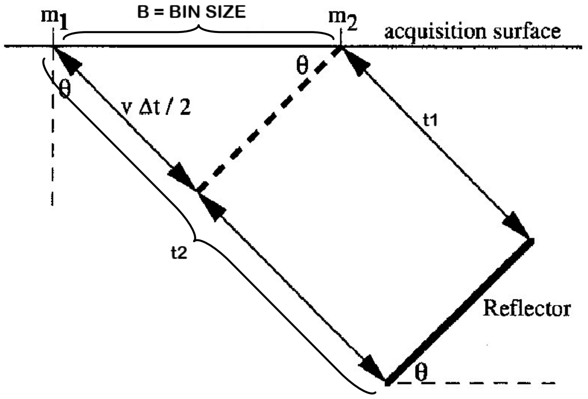

Figure 3-3 (LINER et al., 1999, mod.): Geometry to derive the equation for the bin size, where m_1 and m_2 are the midpoints of two adjacent bins, Θ is the dip of the reflector, v the constant velocity and Δt the delay of the two way travel time from t2 in comparison to t1.

Figure 3-3 shows the geometry for spatial aliasing in a constant velocity earth and a dipping reflector. It can be considered as two adjacent traces in a CMP stack, where m_1 and m_2 are midpoints of two neighbored bins. Because of the dipping reflector, m_1 "sees" the reflection with Δt (two way travel time) later then m_2. With the aid of trigonometric functions the following equation, in dependence of the velocity v and the bin size B, is given (LINER et al, 1999):

$$\boldsymbol{sin(\theta) = \frac{v \cdot \Delta t}{2 \cdot B}} \tag{3.1}$$

Applying the aliasing condition, which means that at least two samples per wavelength has to be recorded, or in other words, that the delay Δt may not be larger than one half of a period T of a given frequency f, where $T = 1/f$, the bin size is derived:

$$\boldsymbol{B \leq \frac{v}{4 \cdot f \cdot sin(\theta)}} \tag{3.2}$$

Equation (3.2) is derived for a constant velocity earth and a single frequency.

LINER et al. 1999 considers a linear, with depth increasing velocity earth, where the maximum frequency f_{MAX} and the velocity at the target should be used. In his paper two practical examples are tested by using once the average velocity (v_{AVG}) and once the interval velocity (v_{INT}). In the common case ($v_{INT} > v_{AVG}$) the bin size is calculated too small by using the average velocity. If the interval velocity is applied to equation (3.2) the horizons below the target will be adequately sampled, but those above will be, more or less, spatially aliased. To avoid this situation the shallowest target must be considered for bin size determination or the bin size is calculated in variable depths. Thus taking the smallest value is giving the final bin size for survey designing.

Hence, the bin size for the shallowest target, to record the maximum frequency f_{MAX} without spatial aliasing effects in respect to the maximum dip θ, is given by:

$$\boldsymbol{B = \frac{v_{INT}}{4 \cdot f_{MAX} \cdot sin(\theta)}} \tag{3.3}$$

where B is the bin size and v_{INT} the interval velocity at the reflector.

Further $v/\sin(\theta)$ can be seen as the *apparent velocity* which is recorded by the vertically plugged receivers. Then the sampling interval can be determined by simply measuring the apparent velocity, where θ can be interpreted as the largest of the maximum dip angle and the *migration aperture angle*. The *migration aperture angle* is usually $30°$ (VERMEER, 2002). In other words: The bin size is equal to one quarter of the *apparent wavelengh* (see Figure 3-4 and Figure 3-5), but since the equation is derived from two way travel time, two samples per wavelength are recorded.

CORDSEN et al., 2000 interprets θ as dip and names B as *maximum unaliased bin size* ***before*** *migration*. Hence, the formula for the *maximum unaliased bin size* ***after*** *migration* is given by:

$$\boldsymbol{B} = \frac{\boldsymbol{v_{INT}}}{\boldsymbol{4 \cdot f_{MAX} \cdot tan(\theta)}} \tag{3.4}$$

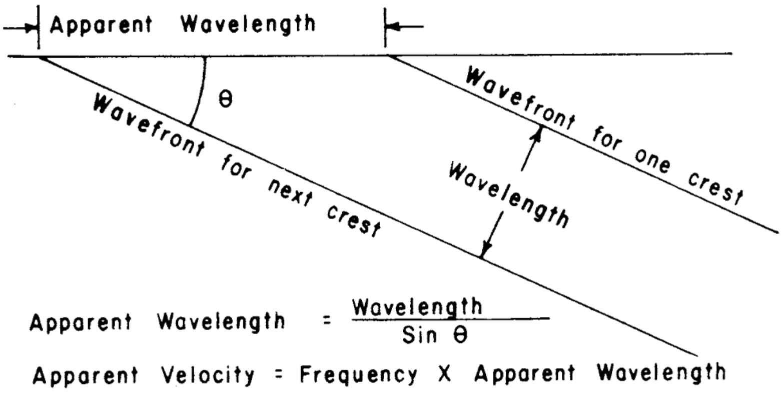

Figure 3-4 (KALLWEIT et al., 1982): Relation between the apparent wavelength and the real wavelength

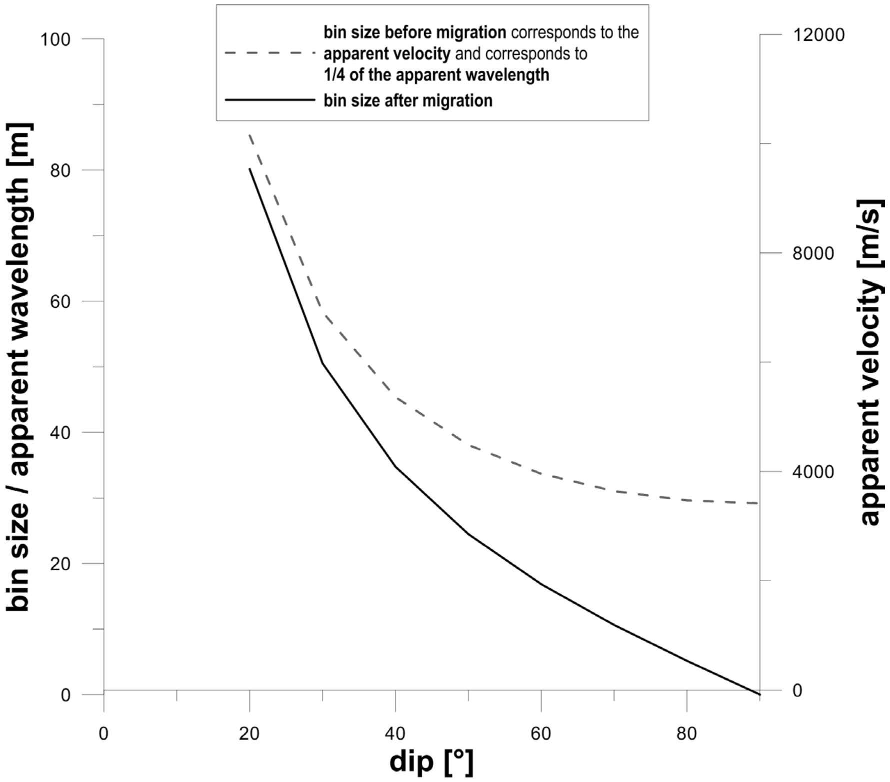

Figure 3-5: Correlation of bin size, apparent wavelength and apparent velocity as a function of the dip for a constant velocity of 3500 m/s and a frequency of 30 Hz.

Note I: In this work only the reflection events are considered to be sampled properly. The 5-D wavefield $W(t, x_S, y_S, x_R, y_R)$ [5] also includes e.g. slow, long-wave surface waves (ground roll), which have to be filtered out in f-k domain and the larger the bin size is chosen, the shorter the Nyquist-wavenumber. Thus there is the risk, that much of the surface wave energy is aliased in the area of reflections in f-k-domain. Hence, it cannot be filtered out and adulterates the reflection signal. To prevent aliasing effects of the ground roll source and receiver arrays should be considered.

Note II: The used software from GEDCO (see chapter 5.3) determines the bin size, by applying the root mean square velocity (v_{RMS}) in equation (3.3) and (3.4) instead of the interval velocity. The bin size before migration is therefore:

$$\boldsymbol{B = \frac{v_{RMS}}{4 \cdot f_{MAX} \cdot sin(\theta)}} \tag{3.5}$$

hence, the bin size after migration is given by:

$$\boldsymbol{B = \frac{v_{RMS}}{4 \cdot f_{MAX} \cdot tan(\theta)}} \tag{3.6}$$

This has been justified by GEDCO with similar arguments then previous implied:

"The wavelength of the f_{max} changes as you move around the model – so when we hit a high interval velocity (often just above the target), this will make the wavelength longer – and hence dictate a bigger bin size. However if we want to image things just below the target they may have lower velocity, hence shorter wavelength and need a smaller bin size to avoid aliasing."

And further: "Basically we decided some time ago that it is best to make sure that ALL parts of the model above the target should have adequate sampling. Thus if we concentrate solely on the target (with a high interval velocity) we will choose a larger bin size as adequate to resolve its features. However such a large bin size may not be

---

[5] x_S...x-coordinate of the source, y_S...y-coordinate of the source, x_R...x-coordinate of the receiver and y_R...y-Coordinate of the receiver

adequate for horizons above the target – with lower velocity – and thus a requirement for smaller bin sizes. By using the RMS velocity we go some way towards ensuring that the "needs" of every horizon in the model will be properly resolved." [6]

The following velocities are extracted from the velocity model with an estimated but realistic dip and maximum frequency beneath the *Neogene Basin Floor.* The example shows, that the bin size can be much smaller, if the *root mean square velocity* is used:

$$depth \;=\; 3720\,m,\; max.dip \;=\; 60°,\; f_{MAX} \;=\; 49\,Hz$$

$$v_{INT} = 6159.1\,m/s \qquad B = v_{INT}/[4 \cdot f_{MAX} \cdot \sin(dip)] = 36.3\,m$$

$$v_{RMS} = 3286.8\,m/s \qquad B = v_{RMS}/[4 \cdot f_{MAX} \cdot \sin(dip)] = 19.4\,m$$

However, the exact bin size can only be calculated for a constant velocity or a linear, with depth increasing, velocity earth. To know the background of deriving the bin size equations will be useful for the final bin size determination in practice (see chapter 6.1).

3.3 NOISE ATTENUATION AND FOLD

Fold is the sum of all CMPs, which are assigned to one bin, hence every bin has a specific fold. All traces in this bin are stacked (summed) in seismic processing to improve the S/N ratio. The dimension of the bin (bin size x bin size) controls fold, where RI and SI controls the bin size (see Figure 3-6).

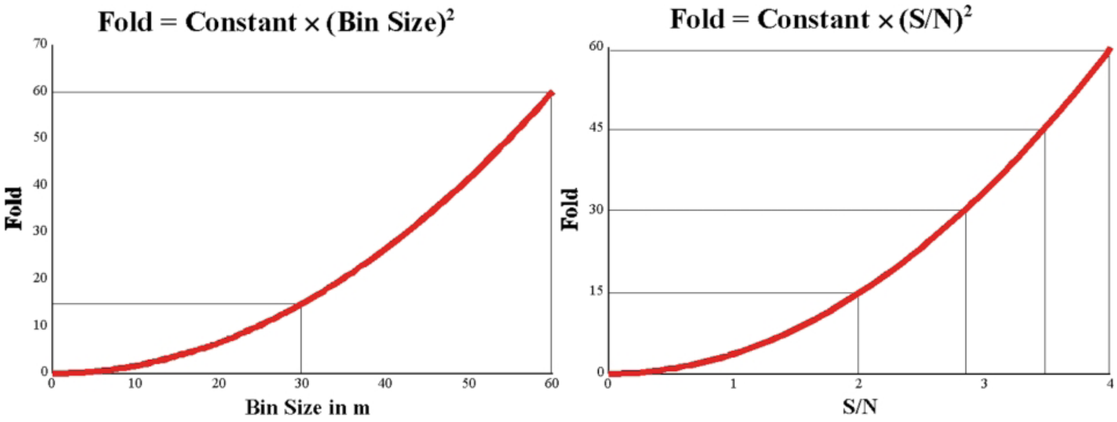

Figure 3-6 (CORDSEN et al., 2000): Bin size and S/N are connected with fold.

---

[6] GALBRAITH, M., WILLSON, N.; 2009: Email from support@gedco.com from 28th October

Generally there are many types of noise, but one can differentiate between *random noise* and *coherent noise*. The random noise is mainly ambient noise and follows theoretically a Gaussian distribution like noise from wind, rain, traffic, industry, sea waves, etc. The *coherent noise* is mainly source generated and in phase, for example ground roll, guided waves, multiple reflections, etc.

The graph in Figure 3-6 on the right shows an improvement of the S/N ratio by $\sqrt{n}$ if n traces are summed, but this is only valid for truly random noise (TELFORD et al., 1990). Random noise can be attenuated by summing traces shot at different times or different places (or both) and is the basis for several stacking techniques, like vertical stacking, common-midpoint stacking, etc. Further the random noise can be attenuated by frequency filtering (band-pass filter, notch filter), by taking multiple sources or one stronger source.

A stronger source will enhance the signal, but as well the source generated noise. Thus a stronger noise and also vertical stacking won't have an effect on coherent noise. The coherent source generated noise can be attenuated effectively by limiting the minimum wavelength (k-filter) or by limiting the recorded velocities (f-k filtering). The k-filter can be realized with linear field arrays (e.g. receiver arrays), which act as spatial anti-aliasing filter. A field array can be considered as a spatially discretely sampled box car function with its Fourier-transformed equivalent, the periodic sinc-function. In comparison: A single geophone has the response of a spatially spike and records all wavelengths. TELFORD et al., 1990 gives the statement: If n *geophones are spread evenly over one wavelength of a coherent noise wavetrain (for example, ground roll), then the coherent noise will be greatly reduced*. Hence, receiver and source arrays should be considered. One the other hand, when AVO[7] studies are planned, the use of linear receiver and source arrays to attenuate noise (random and coherent) can be a problem, because also the signal difference with offset may be attenuated (BROWN, 2004, p.512). The f-k filter can be applied in processing by cutting, for example, a pie slice in the f-k domain.

---

[7] amplitude versus offset

Generally CMP-stacking is very effective to attenuate signal generated and random noise, because traces from different shot and receiver positions, which having the same CMP-bin, are summed.

3.4 SPATIAL RESOLUTION

Resolution is the smallest possible distance between two sub-surface points where they still appear to be separated. There are two types of resolution: the vertical and the horizontal (lateral) resolution, both controlled by signal bandwidth.

In literature there are different views of resolution:

In YILMAZ, 2001 the dominant wavelength is the yardstick for the vertical resolution before migration. Deconvolution tries to increase it by broadening the spectrum and compressing the seismic wavelet. For the lateral unmigrated resolution, the Fresnel zone, is essential: *"The yardstick for lateral resolution is the Fresnel zone, a circular area on a reflector whose size depends on the depth to the reflector, the velocity above the reflector and, again, the dominant frequency. Migration improves the lateral resolution by decreasing the width of the Fresnel zone, thus separating features that are blurred in the lateral direction."*[8]

In VERMEER, 2002 a more practical approach determines resolution. Therefore the maximum frequency, that can be recorded and processed, defines mainly the achievable resolution. Based on a practical formula of the maximum wavenumber:

$$\boldsymbol{k_\alpha} = \frac{\boldsymbol{c}}{\boldsymbol{R_\alpha}} \tag{3.7}$$

where R is the minimum resolvable distance, α indicates direction (x, y, or z), c is some constant (details see page 28), and k_α the required maximum wavenumber in direction α - two formulas for resolution are achieved:

---

[8] (YILMAZ, 2001, p.1801, chapter 11.1)

$$\boldsymbol{R_z = \frac{c}{2} \cdot \frac{v}{f_{max}} \cdot \frac{1}{cos(i)}} \qquad (3.8)$$

$$\boldsymbol{R_\alpha = \frac{c}{2} \cdot \frac{v}{f_{max}} \cdot \frac{1}{sin(\theta) \cdot cos(i)}} \qquad (3.9)$$

where R_Z is the vertical resolution, v the local interval velocity, f_{MAX} the maximum achievable frequency and (i) is the *reflection angle*. The horizontal resolution is indicated by the suffix α and means now x or y direction. Thus the horizontal resolution has one more term $\sin(\theta)$, which depends on a processing factor: θ, the *migration angle*.

Vertical resolution only depends on acquisition parameters and is always better than the horizontal resolution.

Vermeer, 2002 call the resolution, achieved with formula (3.9), *potential resolution,* because it assumes perfect sampling of the wavefield. Further noise decreases the *achievable resolution,* hence also fold is not considered in the *potential resolution*.

However, one can put this considerations into perspective, since the uncertainty of the velocity and the maximum frequency is usually big.

Details for the sin Θ term (GALBRAITH et al., 2009):

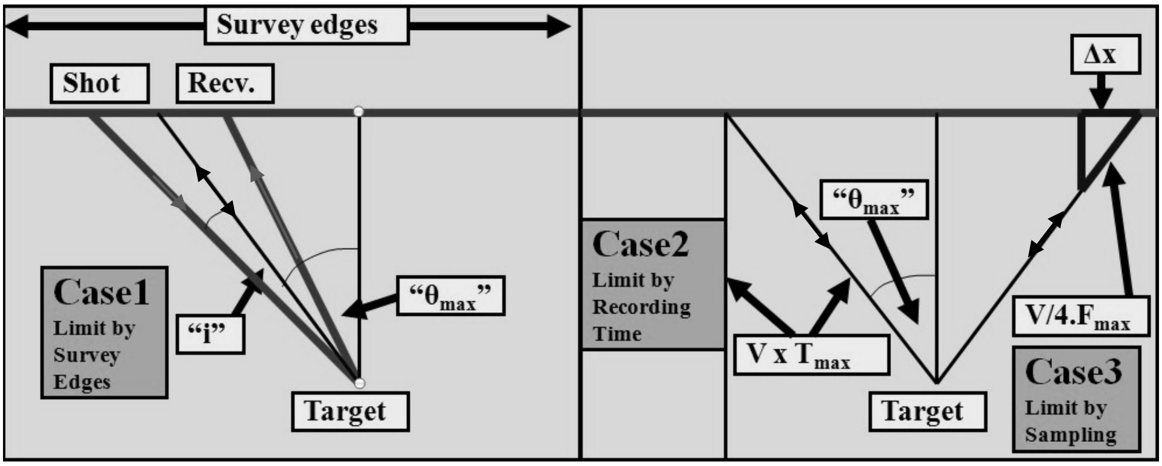

Figure 3-7 (GALBRAITH et al., 2009): Definitions of the factors (cos i) and (sin Θ). Θ is the smallest angle limited by three factors: (1) survey edges, (2) recording time and (3) sampling.

After migration a diffraction curve is collapsed, not quite to a spike, but rather to a wavelet limited by the signal bandwidth. The *migration angle* depends on three acquisition parameters, which affects the lateral resolution. The limitations are illustrated in Figure 3-7.

- Case 1, limit by survey edges: If only a portion of the diffraction curve can be used, because the diffraction point is near the survey edges, the collapse will not be quite complete, the *migration angle* is smaller and the lateral resolution worse.

- Case2, limit by recording time: A diffraction from the scatter point at depth is truncated by recording time. If a small maximum recording time is chosen, the source-receiver offset can be limited (depending on velocity and depth of the subsurface). Hence, again, the diffraction curve may not be collapsed completely.

- Case 3, limit by sampling: For a large bin size, only a reflection with a small angle to the perpendicular can be resolved and hence the maximum dip angle (and the source-receiver offset) will be limited. This angle is given by converting formula (3.5) to $\sin(\theta) = \frac{v_{RMS}}{4 \cdot B \cdot f_{MAX}}$

Details for the constant c and the Rayleigh criterion:

The Rayleigh criterion is founded in optics: "*Rayleigh proposed that, in this case, two components of equal intensity should be considered to be just resolved when the principal intensity maximum of one coincides with the first intensity minimum of the other.*" And further: "*Note: No special physical significance is to be attached to the Rayleigh criterion, and from time to time other criteria of resolution have been proposed.*" [9]

Another criterion may be formed by Ricker or Widess (see Figure 3-8 and Figure 3-9) and is also based on optical experiences.

---

[9] BORN et al., 1999, p.371, chapter 7.6

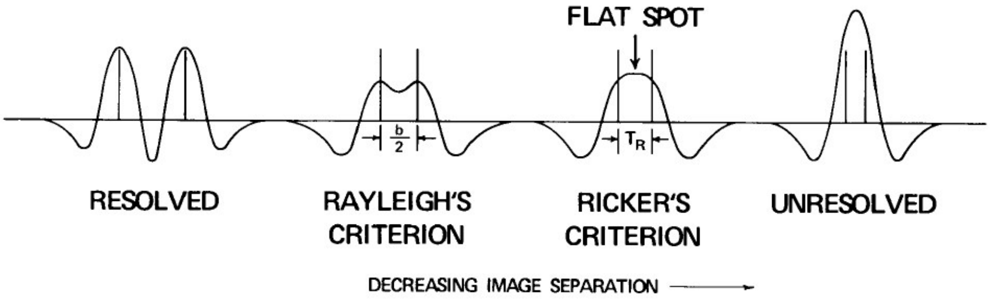

Figure 3-8 (KALLWEIT et al., 1982): Rayleigh's limit of resolution occurs when images are separated by the peak-to-trough time interval, whereas Ricker's limit occurs when they are separated by a time interval equal to the separation between inflection points.

For equation (3.8) and (3.9) the Rayleigh criterion, with the constant $c = 0.715$, is used to calculate the vertical and lateral resolution (VERMEER, 2002 and GALBRAITH, 2004). The equations are not only applicable for zero-offset rays, they also take the half shot-receiver pair angle into account with the $cos(i)$ factor. For a constant velocity medium $cos\ (i)$ represents the NMO stretch effect (see VERMEER, 2002, p.77). Migration improves the lateral resolution, which is represented with the factor $\sin(\theta)$, hence the greater the angle, the better the lateral resolution. Therefore equation (3.9) represents the resolution after migration.

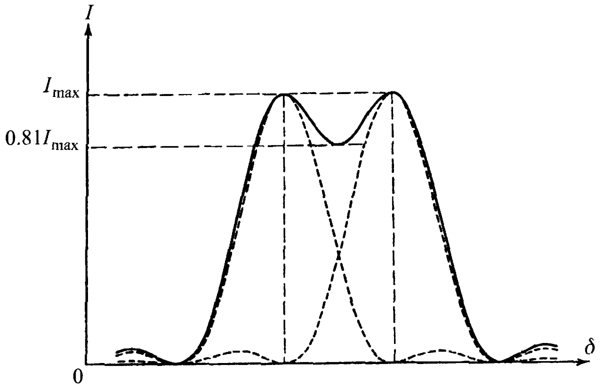

Figure 3-9 (BORN et al., 1999) Two events are just resolved, according to the Rayleigh criterion.

3.5 MINIMUM OFFSET

X_{MIN} is defined as the largest minimum offset (LMOS) of a box and is controlled by the line interval (RLI & SLI). Hence, usually it is the diagonal of the box and can be derived with the aid of the Pythagorean Theorem:

$$\boldsymbol{X_{MIN} = \sqrt{RLI^2 + SLI^2}} \tag{3.10}$$

Generally, to image the shallow subsurface, small offsets are essential. If the shallow subsurface is not of interest, a larger minimum offset can be used. In Figure 3-10 it is evident, that RLI and SLI affects the depth level, or respectively the time level, where at least single fold data can be recorded.

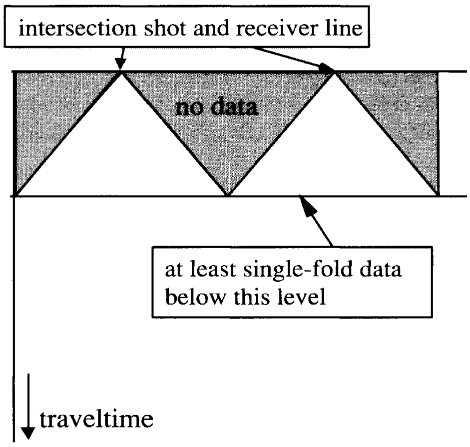

Figure 3-10 (Vermeer, 2002): Cross section along a diagonal of a box (from one RLI-SLI knot to another).

CORDSEN et al., 2000 has the perception, that four-fold data are usually sufficient for interpretation and formulates a rule of thumb: "*X_{MIN} should be less than 1.0 to 1.2 times depth of shallowest horizon to be mapped.*"[10]

In case of the *deep Vienna Basin*, the shallowest horizon of interest is the *Neogene Basin Floor*, which depth is about 3000 m beneath the surface.

---

[10] CORDSEN et al., 2000, p.13, table 2.1, chapter 2.1

3.6 MAXIMUM OFFSET

The deeper the maximal target depth, the larger the maximum offset has to be. Rule of Thumb: X_{MAX} should have the same extent as the target depth and refers to several previous survey data, where this is a good first approximation (CORDSEN et al., 2000).

In conventional time processing before stacking all traces, e.g. to a CMP gather, the traces are NMO (normal move-out) corrected in processing. This time shift lowers the frequency, especially those with large offsets. To limit the maximum time shift in the CMP gather, a maximum NMO-stretch (t_{NMO} in %) can be specified, which leads to a limited maximum offset:

$$\boldsymbol{X_{MAX} = twt \cdot v \cdot \sqrt{(1 + t_{NMO}/100\,\%)^2 - 1}} \tag{3.11}$$

X_{MAX} of equation (3.11) depends on depth (two way travel time twt and the velocity v) and the permitted NMO-stretch t_{NMO}. All recorded traces with an offset larger as X_{MAX} will be muted in processing.

The standard NMO correction is based on the classic hyperbolic approximation, which only uses one parameter (moveout velocity as a function of the zero offset time). It is a good approximation for small offset-to-depth ratios but for big offsets the inaccuracy leads to the need of limiting the maximum offset. In modern processing a non-hyperbolic moveout correction (e.g. a five-parameter non-hyperbolic moveout approximation in FOMEL et al. 2010) is applied, hence the maximum offset is not limited due to the inaccuracy of the hyperbolic computation. Nevertheless, the NMO stretch effect and thus the frequency lowering remain unaffected, but the useable offsets are much larger.

In this work the required maximum offset for imaging the deep layers is determined with the aid of ray tracing (see illumination analysis in chapter 7).

3.7 MIGRATION APERTURE AND MIGRATION APRON

Figure 3-11 demonstrates migration principles in two dimensions. The process is explained well in YILMAZ, 2002 and Figure 3-11:

Migration moves event C'D' on the time section to its true subsurface position CD. The area of interest is OA. If only the line OA is recorded, no receivers can catch the rays appearing between A and B on the surface and hence the time section will be blank. If only segment AB is recorded, then event C'D' would be absent from the migrated section. Thus the record has to be from OB. Additionally the line has to be long enough to record the tails of the diffraction curves and recording time has to be large enough.

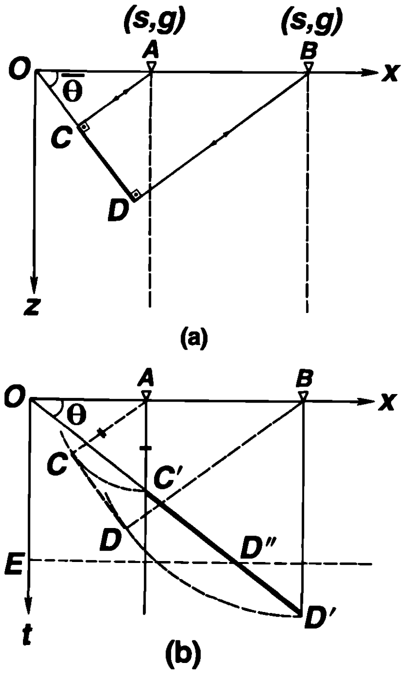

Figure 3-11 (YILMAZ, 2002): Migration principles: The reflection segment C'D' in the time section (b), when migrated, is moved updip, steepened, shortened, and mapped onto its true subsurface location CD (a).

The displacements of a dipping event by migration in x - and t - direction depends on medium velocity, depth and dip of the event.

These considerations can be applied also in three dimensions, where the area of interest has to be extended, especially in dip direction. For a constant velocity medium the migration aperture is simply calculated by:

$$MA = z \cdot tan(\theta) \qquad (3.12)$$

where MA is the migration aperture, z is the depth and θ the migration angle. The migration aperture is much larger for a constant velocity as for a linear, with depth increasing, velocity field (see Figure 3-12 A).

Based on LINER et al. 1999, who gives the formula for a linear with depth increasing earth MURTY et al. 2007 derives the *zero offset migration distance* AC (see Figure 3-12 B) for a medium with several horizontal constant-velocity layers with the following equation:

$$\boldsymbol{MA = \sum \delta Z_i \cdot tan(\theta_i)} \tag{3.13}$$

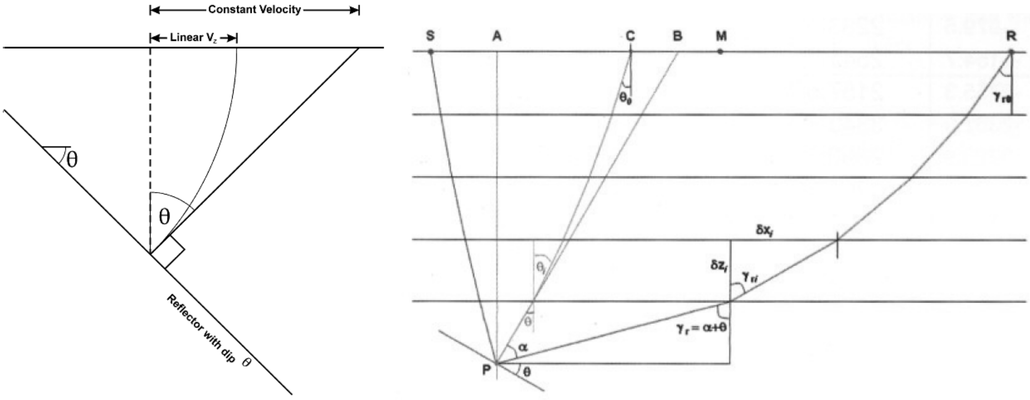

Figure 3-12: A) (CORDSEN et al., 2000) Width of migration aperture for a constant velocity medium versus a linearly varying velocity B) (MURTY et al., 2007) Zero offset migration aperture AC in a horizontal layered medium. SR can be calculated with the angle α.

With equation (3.13) the migration aperture for a zero offset ray PC can be calculated. Therefore the angle θ is the largest of the maximum *migration angle* and dip. The angles for all layer above θ_i, can be derived with Snell's law, if velocity information is available.

Every digitized depth-varying velocity model can be considered as a constant-velocity layered model and equation (3.13) can be used, where δZ_i are sampling intervals.

To determine the *migration apron* first the *migration aperture* for every subsurface point (grid bin) in the area of interest has to be calculated. Then the *migration apertures*, which are reaching outside of that area, define the *migration apron*.

4 THEORY IN RAY TRACING, ATTENUATION AND SYMMETRICAL SAMPLING

In these chapter the theory about wave propagation, ray tracing and attenuation of seismic waves are treated briefly. At the end some further basic aspects are presented to show how to sample a 3D survey correctly.

4.1 WAVE EQUATION

How a wave is propagating through the earth is depending on its frequency (source dependent) and its velocity (rock dependent). Therefore the wavelength λ is as longer, the bigger the velocity v and the lower the frequency f:

$$\lambda = \frac{v}{f} \tag{4.1}$$

Mathematically, the elastic wave equation can be derived by combining the equation of motion (4.2) and Hook's law (4.3) for isotropic materials:

$$\frac{\partial \sigma_{ij}(\vec{x},t)}{\partial x_j} = \rho \cdot \frac{\partial u_i(\vec{x},t)}{\partial t^2} \tag{4.2}$$

where:

$$\sigma_{ij} = \lambda \cdot \theta \cdot \delta_{ij} + 2 \cdot \mu \cdot \epsilon_{ij} \tag{4.3}$$

σ_{ij}	stress tensor	θ	cubic dilatation
ϵ_{ij}	strain tensor	λ, μ	Lamè parameter
δ_{ij}	Kronecker delta	$x_j, \vec{x}$	space vector
u_i	displacement vector	t	time
ρ	density of the medium		

Combining this differential equation with the Helmholtz decomposition (the displacement field can be defined as the gradient of a scalar potential field $\Phi(\vec{x},t)$ added to the rotation of a vectorial potential $\vec{\psi}(\vec{x},t)$ field), there is one solution for the scalar vector field (describing P-waves with velocity v_p) and one solution for the vectorial potential field (describing S-waves with velocity v_s):

$$\vec{\nabla}^2\Phi = \frac{1}{{v_p}^2}\cdot\frac{\partial\Phi}{\partial t^2} \quad and \quad \nabla^2\vec{\psi} = \frac{1}{{v_s}^2}\cdot\frac{\partial\vec{\psi}}{\partial t^2} \tag{4.4}$$

where:

$$v_P = \sqrt{\frac{\lambda + 2\mu}{\rho}} \quad and \quad v_s = \sqrt{\frac{\mu}{\rho}} \tag{4.5}$$

4.2 EIKONAL EQUATION AND RAY TRACING

Ray tracing is calculated faster than solving the full wave equation and is an approximation for waves with "high" frequent energy (wavelengths, which are short in comparison to changes in the velocity field). This assumption is adequate for most seismic applications.

"ray theory: Use of ray tracing to track wave energy. Appropriate where the wavelength is small compared with spatial dimensions e.g., reflector radius of curvature. Implies that changes of λ, μ or ρ are small over a wavelength." [11]

The basis for ray tracing is the Eikonal equation, which can be derived from the scalar wave equation (4.4) with the following approach (SCHURR, 2007)

$$\Phi = A(\vec{x})\cdot e^{-i\cdot\omega\cdot T(\vec{x})} \tag{4.6}$$

---

[11] SHERIFF, 2002, p.287

where $T(\vec{x})$ is a phase factor, $A(\vec{x})$ the local amplitude and $\omega = 2 \cdot \pi \cdot f$ the angular frequency of the wave. Combined with equation (4.4) the following complex equation is given:

$$\vec{\nabla}^2 A(\vec{x}) - \omega^2 \cdot A(\vec{x}) \cdot \left|\vec{\nabla} T(\vec{x})\right|^2 - i \cdot \left[2 \cdot \omega \cdot \vec{\nabla} A(\vec{x}) \cdot \vec{\nabla} T(\vec{x}) + \omega \cdot A(\vec{x}) \cdot \vec{\nabla}^2 T(\vec{x})\right] = \\ = -\frac{A(\vec{x}) \cdot \omega^2}{v(\vec{x})^2} \tag{4.7}$$

where $v(\vec{x})$ is the velocity of the wave. Solving the real part and with the high frequency assumption $(\omega \gg)$ the Eikonal equation can be achieved:

$$|\nabla T(\vec{x})|^2 = \frac{1}{v(\vec{x})^2} \tag{4.8}$$

The special case $T(x) = constant$ is defining wave fronts. The direction of the ray is defined through the gradient of the phase factor $T(x)$, which equates the spatial slowness $\vec{p}$, and is called first ray tracing equation:

$$\vec{\nabla} T = \vec{p} \tag{4.9}$$

Solving the imaginary part of (4.7), the result describes the effect of geometrical spreading of the amplitude.

The normal to a wave front forms a ray. Going along this ray an infinitesimal part of the ray path ds gives the following relation:

$$\frac{d\vec{x}}{ds} = \vec{\nabla} T \cdot v(\vec{x}) = \vec{p} \cdot v(\vec{x}) = unit\ vector \tag{4.10}$$

Hence the Eikonal equation can be transformed from a function of travel time to a function of travel path (second ray tracing equation):

$$\frac{d\vec{p}}{ds} = \frac{d}{d\vec{s}}\left(\frac{1}{v(\vec{x})} \cdot \frac{d\vec{x}}{d\vec{s}}\right) = \vec{\nabla}\left(\frac{1}{v(\vec{x})}\right) \tag{4.11}$$

Ray tracing means to solve this differential equation to get the ray path for an arbitrary velocity function. Usually it is solved numerical by finite differences. Due to the high frequency assumption of the Eikonal equation ray tracing is not valid on discontinuous velocity changes. As an example, HOLE et al., 1995 can solve velocity contrasts up to 1:4.

Two-point ray tracing: There are two kinds of two-point ray tracing, both are iterative nonlinear methods (see Figure 4-1) :

- the *shooting* method fixes one end of the ray on the source point and then the ray is calculated with varying start angles, until he arrives the receiver.
- the *bending* method fixes both ends and estimates a first initial path. Then the ray is varied as long till the ray equates the ray tracing equation.

The bending method is more efficient than the shooting method (YANG, 2003).

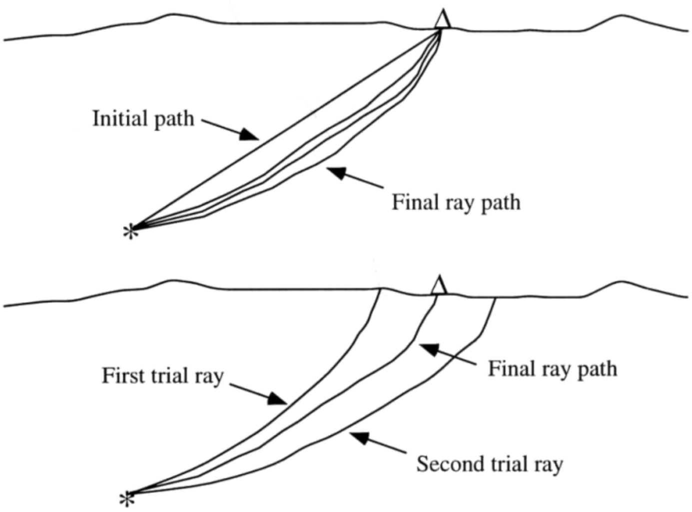

Figure 4-1 (THURBER et al., 2000): Top: The bending method, determines the ray path by iteratively perturbing an initial path estimate with two fixed end-points until it satisfies the ray equations.
Bottom: The shooting method, determines the ray path by treating it as an initial value problem, with a specified starting path point and trial propagation direction, and then iteratively adjusting the propagating direction until the target end point is reached.

4.3 ATTENUATION OF SEISMIC WAVES

The amplitude of a seismic wave travelling from source to receiver is continuously decreasing. This has several reasons (SCHURR, 2007):

A) Geometrical spreading: In a homogeneous and isotropic medium wave propagation from source occurs spherically. The energy is distributing over the spherical surface which expands with $1/r^2$, so the energy gets smaller with the same factor. The amplitude decreases with 1/r. A planar wave is the marginal case of a spherical wave and geometrical spreading has no effect.

B) Separation of reflected and transmitted waves on geological borders with impedance contrast.

C) Scattering effects: In a heterogeneous medium the wave doesn't take only the shortest way. The energy is scattered and makes small detours on the way to the receiver. This results in small temporal displacements of seismic energy (smearing of seismic energy).

D) Intrinsic attenuation (absorption): This effect is caused by inelastic effects of the rock (e.g. friction between grain boundaries) which the wave passes through. It can be described with the dimensionless term Q which is defined as the energy E stored in the material divided through the energy loss ΔE per unit circle. For a medium with a linear stress-strain relation the amplitude A is proportional to $\sqrt{E}$ $(2 \cdot \ln A = \ln E)$ and with the assumption that the quality factor Q >> 1 the following relation to the amplitude is given (after AKI et al., 2002, Box 5.7):

$$\frac{1}{Q(\omega)} := -\frac{\Delta E}{2 \cdot \pi \cdot E} = -\frac{\Delta A}{\pi \cdot A} \tag{4.12}$$

Q is called quality factor, which is in general also frequency depended. Thus, we want to know $A(x)$ measured from an initially amplitude $A(\mathrm{x{=}0}) = \mathrm{A}_0$ where $A(x)$

decreases a fraction π/Q (after 4.12) at successive distances $x = \lambda, 2\lambda, 3\lambda, \dots\dots, n\lambda$. λ can be expressed in terms of the angular frequency ω and the velocity v of the wave:

$$A(x) = A_0 \cdot \left(1 - \frac{\pi}{Q}\right)^n \qquad (for\ x = 2n\pi v/\omega) \tag{4.13}$$

By using the definition of the exponential function $\exp(\xi) = \lim_{n\to\infty} \left(1 + \frac{\xi}{n}\right)^n$ and after a substitution of π the following relation is given:

$$A(x) = A_0 \cdot \left[1 - \frac{\omega \cdot x}{2 \cdot n \cdot v \cdot Q}\right]^n$$

$$\Rightarrow\ A(x) = A_0 \cdot e^{-\frac{\omega \cdot x}{2 \cdot v \cdot Q}} = A_0 \cdot e^{-\alpha \cdot x}$$

α is called the damping factor and with $\omega = 2\pi f$

$$\alpha = \frac{\pi \cdot f}{Q \cdot v} \tag{4.14}$$

Hence, the attenuation is higher for small quality factors Q and for small wavelengths (v/f). High frequencies are more damped as low frequencies and low velocities effect in a high damping factor. After conversion of equation (4.14) the maximum achievable frequency can be calculated by using the velocity model (including v and Q) for a given amplitude ratio.

$$f_{MAX} = \frac{Q \cdot v}{\pi \cdot x} \cdot \ln \frac{A_0}{A} \tag{4.15}$$

Amplitude losses are usually given in Decibel with the following relation:

$$Amplitude\ Loss\ [dB] = 20 \cdot log \left(\frac{A_0}{A}\right) \tag{4.16}$$

4.4 THE CONTINUOUS WAVEFIELD AND 3-D SYMMETRICAL SAMPLING

In the following some extracts from the book *3-D Seismic Survey Design* (VERMEER, 2002) are cited. It should be an supplementation of chapter 3.2 and give a small insight to Vermeer`s theory about the continuous wavefield and 3-D symmetrical sampling. Symmetrical sampling is based on the *reciprocity theorem* (properties of the common-receiver gather are the same as the properties of the common-shot gather) and includes for an orthogonal geometry equal source and receiver intervals, equal source and receiver line interval and equal maximum offset in- and crossline (aspect ratio of the pattern should be near 1). For each 3D geometry a *basic subset* can be constructed, where two of the four spatial coordinates are considered to be constant. For example in an orthogonal geometry the receiver coordinate can only vary in x direction and the source coordinate can only vary in y direction. Hence, the *basic subset* for the orthogonal geometry is the cross spread. Since it has *single-fold data*, it is also called *minimal data set* (after PADHI et al., 1997).

In 2-D, the sampling problem is one of sampling the 3-D wavefield W (t, x_S, x_R) *with temporal coordinate t, shot coordinate* x_S *and receiver coordinate* x_R. *In 2-D symmetric sampling, the two spatial (shot and receiver) coordinates are sampled in the same way. Using sufficiently small sampling intervals allows the faithful reconstruction of the underlying continuous wavefield, i.e., it maintains the spatial continuity of the wavefield W* (t, x_S, x_R). (VERMEER, 2002, p. 17)

In 3-D, we are faced with the sampling of a 5-D wavefield W (t, x_S, y_S, x_R, y_R) *now with shot* y_S *and receiver* y_R *as additional spatial coordinates. It would be prohibitively expensive to completely sample this 5-D wavefield, as this would mean filling the whole survey area with a dense coverage of both shots and receivers.* (ibid, p. 17)

W (t, x_S, y_S, x_R, y_R) *can be considered as a continuous function of its variables. In the acquisition of seismic data, the 5-D wavefield* (t, x_S, y_S, x_R, y_R) *is sampled at individual source and receiver locations. The assumption of continuity means that small shifts in source or receiver position would lead to only small changes in the wavefield. Proper* *sampling of the continuous wavefield allows full reconstruction of that wavefield.* (ibid, p. 20)

One approach to 3-D survey design attempts to sample all four spatial coordinates of the 5-D prestack wavefield as well as possible. Because of the high cost of dense sampling, this objective leads to coarse sampling of the four spatial coordinates with ensuing difficulties in the application of spatial filters and prestack migration.

Alias-free sampling of the whole 5-D prestack wavefield is clearly too expensive. Often, it is also impractical, since it requires free access to the whole survey area. (ibid, p. 25)

For all intents and purposes, it is impossible to properly sample the whole 5-D prestack wavefield. Three dimensional symmetric sampling prescribes the next best alternative: proper sampling of single-fold basic subsets. Such sampling allows optimal prestack processing, and it takes care of a design criterion that is often overlooked: spatial continuity. (ibid, p. 45)

Another benefit of symmetric sampling is that the designer does not need to worry about the offset distribution: 3-D symmetric sampling automatically leads to a reasonable offset distribution. (ibid, p. 69)

For instance, in a complex geology it is more important to use small sampling intervals than in a geology which is basically flat. (ibid, p. 74)

5 AVAILABLE DATA AND SOFTWARE TOOLS

In this chapter the provided velocity model and the used software tools are presented and shortly described.

5.1 VELOCITY MODEL

As mentioned in chapter 1.4 the provided 3D velocity model includes velocities and quality factors Q of the investigation area and was constructed in the first part of the project by Stefan Pfeiler. The second floor is modeled by using roughly known geological structures and well data. Detailed structures should be delivered after a successful measurement of a future survey. The velocity model covers an area of about 15 km x 19 km x 10 km with a lateral resolution of about 200 m and a vertical resolution of 100 m. It is located northwest of Vienna (see Figure 2-4) and is prepared for the import in the acquisition software *Omni* from *Gedco*. Therefore, the file has a specific *.vin* format, which contains at every x, y - pair interval velocities and quality factors Q for different two way times (twt). The surface reference datum (SRD) of the model is 130 m above mean sea level (msl), hence $z = +130\,m$ corresponds to the two way time of zero seconds.

The model can be used for *target analysis* in chapter 6. For *illumination analysis* in chapter 7 there is the need of rebuilding the model to constant velocity layers (see chapter 7.2).

Figure 5-1 demonstrates slices through the velocity model. Therein the geological units (compare with chapter 2.2 and HAMILTON, 2000) are labeled as follows:

1. *Neogene Basin fill* from river and sea deposits, due to continuous subsidence and the pull-apart mechanism. Hence, the sediment layers are mainly horizontal and consist of sandstones, some conglomerates and marls. The velocity from the SRD to the *Neogene Basin Floor* is increasing with depth and

ranges from 1800 m/s to about 4600 m/s. Beneath the *Neogene Basin Floor* appears the *Northern Calcareous Alps* (4, 5, 6) in the south east and *Flysch* (2) in the north west.

2. *Flysch* was deposited in a deep marine facies. The lower part of the *Flysch* is compressed by the overlying load which yields to a linear velocity gradient (4500 m/s to 6500 m/s) with depth.
3. The dolomitic unit is called *Schönkirchen nappe* with a velocity of about 6200 m/s. This is a strong velocity contrast in comparison to the *Neogene Basin fill* 1.
4. This section is called *Göller nappe*. The unit consists of dolomite (Hauptdolomit) in its core and limestone. The velocities range from 5600 m/s to 6000 m/s.
5. The *Giesshübl monocline* demonstrates a low velocity zone in comparison to 4 and 6. It consists of shales, tight sandstones and partially breccias at the base. The unit acts as cap rock, which is sealing the subjacent dolomitic gas traps. The velocity is about 5500 m/s.
6. The dolomitic *Frankenfels-Lunz nappe* has very high velocities up to 6600 m/s.

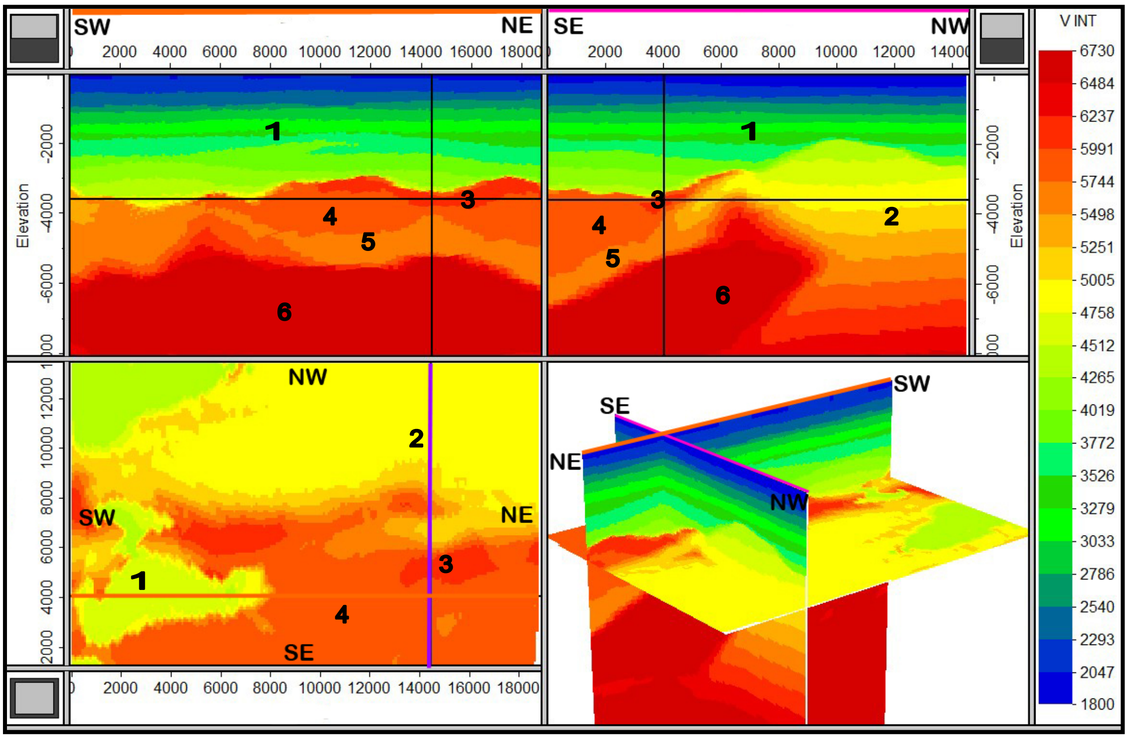

Figure 5-1: Slices through the velocity model, including the *Neogene Basin Fill* (1), the *Flysch zone* (2) and the *Calcareous Alps* (3, 4, 5 and 6). Top left: slice (orange line) from southwest to northeast. Top right: slice (pink line) from southeast to northwest. Bottom left: slice in 3600 m depth from birds view. Bottom right: 3D view from north. The numbers are representing the geological units.

The target for the seismic acquisition design is part 3 to part 6, the *Northern Calcareous Alps*, which stratigraphy ranges from Permian (300 ma) to the Paleocene (60 ma). The velocity model represents the geologic model of Figure 2-3 with some approximations.

5.2 SEISMIC 2D-LINE

A 2D seismic line was recorded in 2007, which is intersecting the investigation area. The raw data are used to extract frequency information, which will be necessary to determine the spatial resolution and bin size in chapter 6. The location of the line is shown in Figure 2-4 and is red-colored.

One line in Figure 5-2 represents the frequency content of a 500 ms time window of the stacked 2D data, which were generated by a non-linear seismic sweep between 6 and 64 Hz. To extract the frequency information the processing software *Geoclaster*, developed by *CGGVeritas,* was used. The attenuation of the amplitude is given in Decibel and had to be considered as a relative value. From the achieved spectrum in Figure 5-2 the maximum and dominant frequency is estimated. The maximum frequency is chosen where the signal is damped with -12 dB, which corresponds to an amplitude ratio (A/A_0) of 4. The dominant frequency is observed, where the spectrum has its peak.

Table 5-1 contains the determined values from Figure 5-2. The maximum depth, given in meters, is converted from the maximum travel time with the aid of a time-depth function, averaged from several well data. Each spectral curve is normalized to the maximum amplitude in the spectrum (0 dB), so the amplitudes of the spectra have to be considered relatively. The shallowest spectrum (green line) has, as expected, the best high frequency content (f_{MAX} = 62 Hz); the amplitudes at lower frequencies are smaller and may be caused by the nonlinear sweep (see Figure 5-3). Noticeable is the decrease of the high frequency content with increasing depth due to absorption (see chapter 4.3 D). Beneath the *Neogene Basin Floor* (flesh colored line and below) the high frequency content is decreasing significantly, where the maximum evaluable frequency is beneath 32 Hz and the dominant frequency is about 16 Hz.

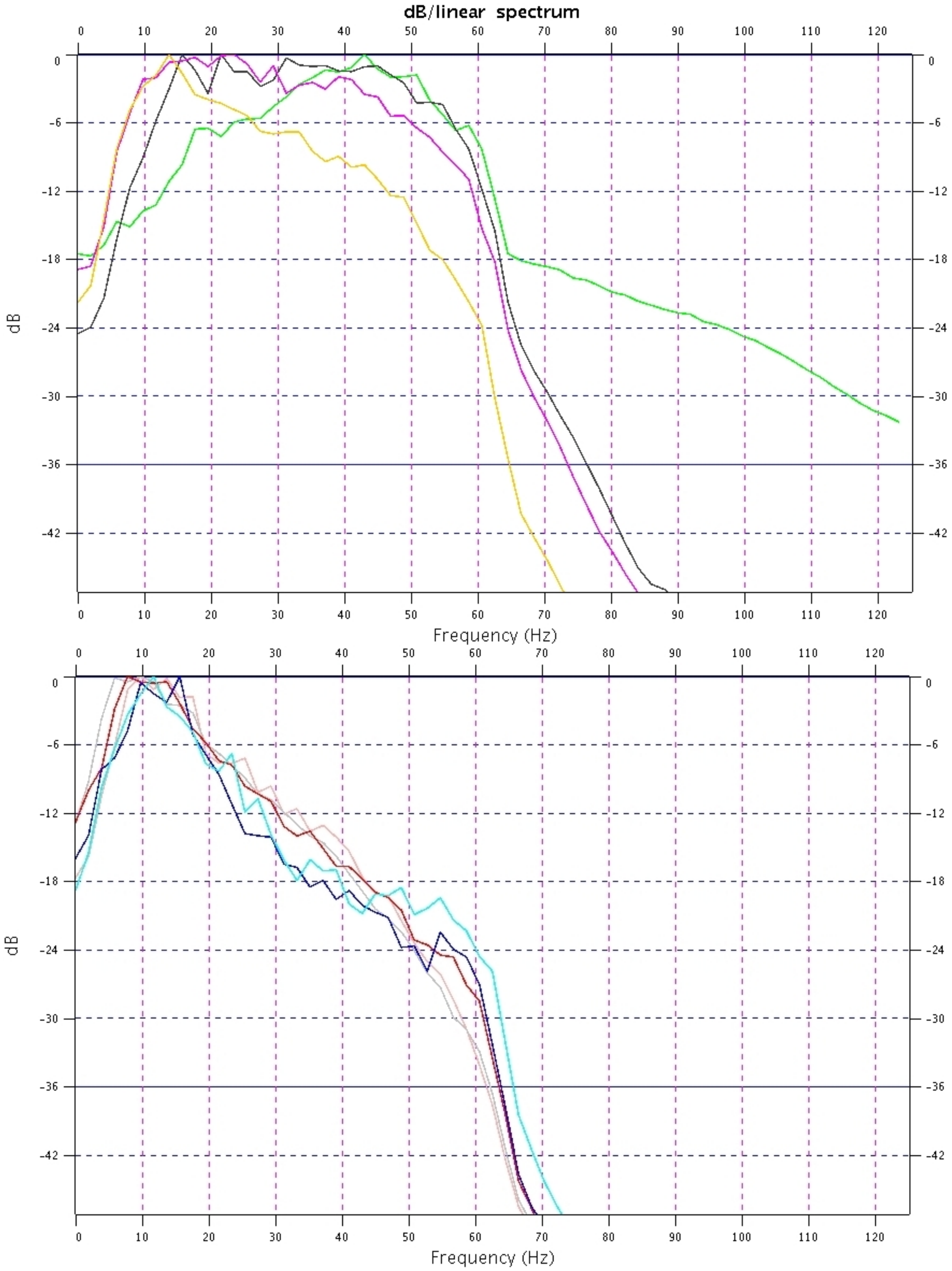

Figure 5-2: Normalized frequency spectrum extracted from an existing 2D line; time steps: 500 ms. The green, black, purple and yellow lines in the upper screenshot represents the frequency information from the *Neogene Basin fill*. The flesh-colored, gray and red lines in the lower picture represent the second floor of the investigation area. The blue and light-blue lines are frequency information from the third floor. The nonlinear source sweep ranges from 6 to 64 Hz.

	travel time range	max. depth	maximum frequency	dominant frequency
	ms	m	Hz	Hz
green line	0-500	500	62	49
black line	500-1000	1200	61	48
purple line	1000-1500	2000	58	46
yellow line	1500-2000	2900	46	32
flesh-colored line	2000-2500	4300	32	20
gray line	2500-3000	5900	31	16-17
red line	3000-3500	7300	30	16
blue line	3500-4000		28	15
light-blue line	4000-4500		25	13

Table 5-1: Dominant and maximum frequency, picked from Figure 5-2.

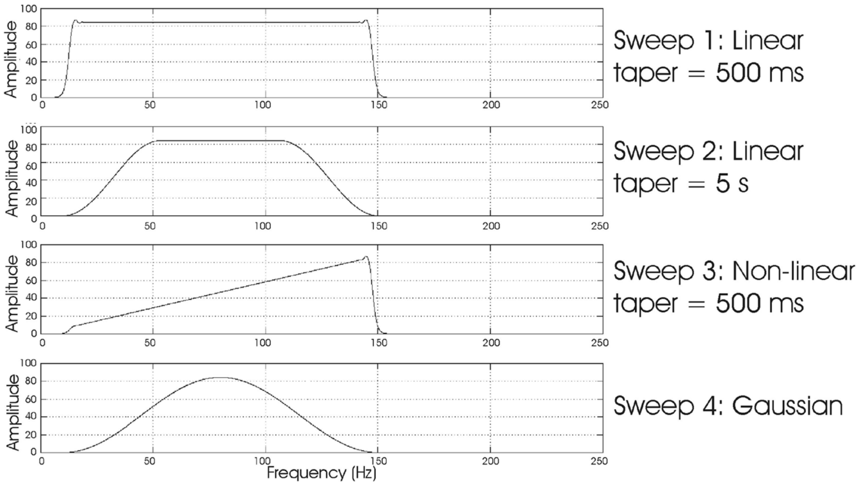

Figure 5-3 (BRITTLE et al., 2001): Examples of different sweep forms. A linear sweep has a constant spectrum, a nonlinear sweep has a linear increasing amplitude spectrum.

5.3 OMNI 3D SURVEY DESIGN & MODELING SOFTWARE

GEDCO developed this software for windows platforms and survey designers with the purpose to calculate acquisition parameters and visualize the results in three dimensions. However, a three dimensional velocity model is required. In the following a short overview of the used modules in this work is presented:

A) Velocity model: In this module a velocity model can be visualized in three dimensions. The data input has to include at every (x,y)-point the velocity, the two way time and the quality factor Q. In this module the elevation datum cannot be specified, hence the two way time of zero seconds belongs to the elevation of zero meters. In the following an extraction of the velocity model file, which has the extension *.vin*, is given:

e.g.:

```
LOC 511283.028 5356401.075
1931.047    0.172 50
1996.412    0.221 50
2045.435    0.270 50
2094.459    0.319 50
LOC 516483.028 5354801.075
2012.753    0.139 50
2061.776    0.195 50
2110.800    0.251 50
2143.482    0.306 50
```

B) Target layer: To create a *target layer* (also called *target model*) the x, y, z - data of the horizon, a velocity model and the surface reference datum (SRD) had to be specified as input. Hence, a target layer is a x,y,z-layer with RMS velocity information. Parameters like bin size, maximum frequency, maximum offset, lateral and vertical resolution, migration aperture, etc. can be calculated and visualized on the surface. This analysis is called *target analysis* (see chapter 6).

C) Survey: In this module an acquisition layout with different patterns can be created. Therefore layout depended analysis can be done, which can be applied on a *target layer* (B) or on a *3d ray model* (E).

D) 2D ray model: A model in x-z-domain can be created with poly lines or with a slice through a *3d ray model (E)*. Several analyses can be applied interactively like resolution, migration aperture, aliasing, etc. Ray tracing from a source to a receiver can be visualized. In this work it was used for test purposes only.

E) 3d ray model: In this module a new subsurface model with constant velocity layers can be created. For each layer a constant velocity and density can be specified. Details for building a model see chapter 7.2.

5.4 GOCAD

The software from *Paradigm* is used to create constant velocity layers from the velocity model to achieve horizons for creating a *3d ray model* in *Omni* (see chapter 7.2). First the velocity model was imported as "PointsSet", where every xyz-sampling point has information of the interval velocity and the quality factor Q. Then a new "Voxet" was created and the properties were transferred from the "PointSets" data. After adequate interpolation and smoothing several new "Surfaces" with constant interval velocity were exported . As an example the layer with a constant velocity of 5900 m/s is illustrated in Figure 5-4.

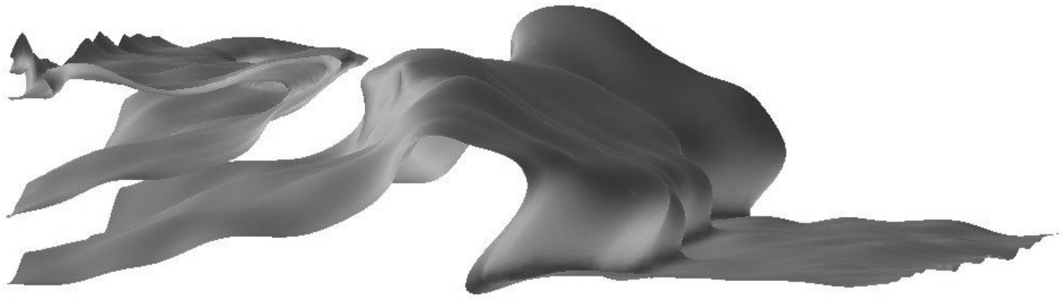

Figure 5-4: Example of an exported iso-surface in *GOCAD* with 5900m/s.

5.5 HOLE

This UNIX-based program uses the algorithm written by J. A. Hole and is used as a benchmark for Omni's ray tracing algorithm in chapter 7.5. This is necessary, because no references of the used ray tracing algorithm in Omni could be found. Inquiries at the customer support of *Gedco* affirmed, that two-point ray tracing is used.

The ray tracing algorithm used by *HOLE* is already established for inversion problems of wide-angle refraction and reflection purposes in earth's crust (e.g. BEHM et al., 2007). The experiences had shown that this is a robust ray tracing algorithm, even in complex velocity models.

The program uses a three-dimensional finite-difference algorithm and is based on Vidale's algorithm (see VIDALE, 1988 and 1990) with some small modifications to handle large and sharp velocity contrasts properly. Velocity contrasts of 1:4 can be calculated without problem (HOLE et al., 1995), where the largest velocity contrast in the *3d ray model*, used in this work, is 1:1.67. The Eikonal equation (4.8) is solved with the finite-difference method. The true first-arrival times of the reflections are calculated through a particularly complex 3-D velocity model, and works even where other ray tracing algorithm may have difficulty finding the true first-arrival path. Further the algorithm is faster and more accurate then several alternative schemes (HOLE et al., 1995). The computation time depends approximately linear on the number of grid nodes and is independent on the number of receivers and almost independent on the velocity model. Reflection travel times are calculated simultaneously for all receivers, requiring only two applications of the finite-difference algorithm (HOLE et al., 1995). The disadvantage of this algorithm is that only first-arrival times of the reflections can be computed.

To use this algorithm the velocity model has to be resampled with constant resolution in x, y and z direction, the z-coordinate has to be positive in the downward direction and it has to be renamed in "vel.mod" and "vreset.mod". The geometry of source and receivers has to be specified in several file types: *.his contains all shot locations, *.rir contains receiver coordinates, and *.hir for CMP locations. The reflector has to be given in a constant grid with the file extension *.ref. Further there are control files specified for velocity model and reflector (*.v1d and *. r1d) which includes node spacing and model extend in x-, y-, and z- dimension. Finally the *.ri file acts as executing file which includes the links to the geometry-, velocity- and reflector files.

The output file consists of the reflection point coordinates in x-, y- and z- dimension. A *Matlab* script was programmed to arrange the reflector in grid bins (binning) and counts the reflection points per grid bin to get the illumination of the layer.

6 PARAMETER DETERMINATION WITH TARGET ANALYSIS

In this chapter the most significant three *target layers* of the *deep Vienna Basin* are analyzed in *Omni* to get information about the optimum parameters for the acquisition design, like bin size, maximum unaliased frequency, maximum offset, resolution after migration, attenuation and migration apron. The last chapter 6.7 gives a summary of the determined parameters in Table 6-2.

A *target layer* in *Omni* (see chapter 5.3) is defined as a xyz-layer with RMS velocity information, which is taken from the original velocity model.

The following three horizons are selected for applying the so called *target analysis*:

Horizon 1 (see Figure 6-1) is the iso-surface with a constant interval velocity of 4500 m/s, extracted with GOCAD from the smoothed velocity model. It represents the *Neogene Basin Floor*.

Horizon 2 (see Figure 6-2) is the iso-surface with a constant interval velocity of 5700 m/s, extracted with GOCAD from the smoothed velocity model. The flank in the south-east represents the base of the *Giesshübl Monocline*, the north-western part represents *Flysch* with a constant interval velocity of 5700 m/s and the ridge between is the *Reyersdorf dolomite*.

The flank of **Horizon 3** (see Figure 6-3) typifies the base of the *Northern Calcareous Alps* (BaseNCA). The north-western part is again *Flysch* with a constant velocity of 5700 m/s (same as on Horizon 2).

As described in chapter 5.1 the *Flysch zone* has a linear, with depth increasing velocity, without an impedance contrast. Hence, the *Flysch* parts in Horizon 2 and 3 are not really reflecting areas and therefore no geological interfaces. This is necessary due to software reasons, since the target layer extension has to range across the whole investigation area (see also chapter 7.2).

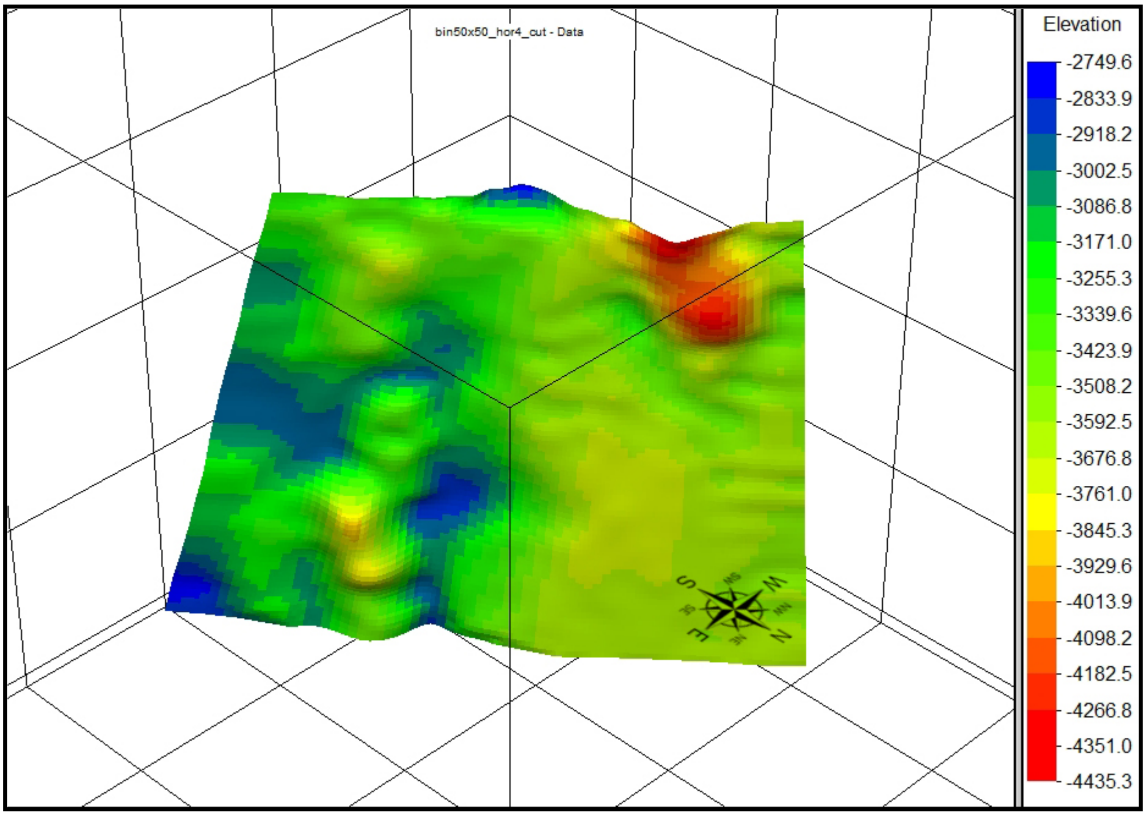

Figure 6-1: Elevation of Horizon 1, which is representing the *Neogene Basin Floor*. View from northeast.

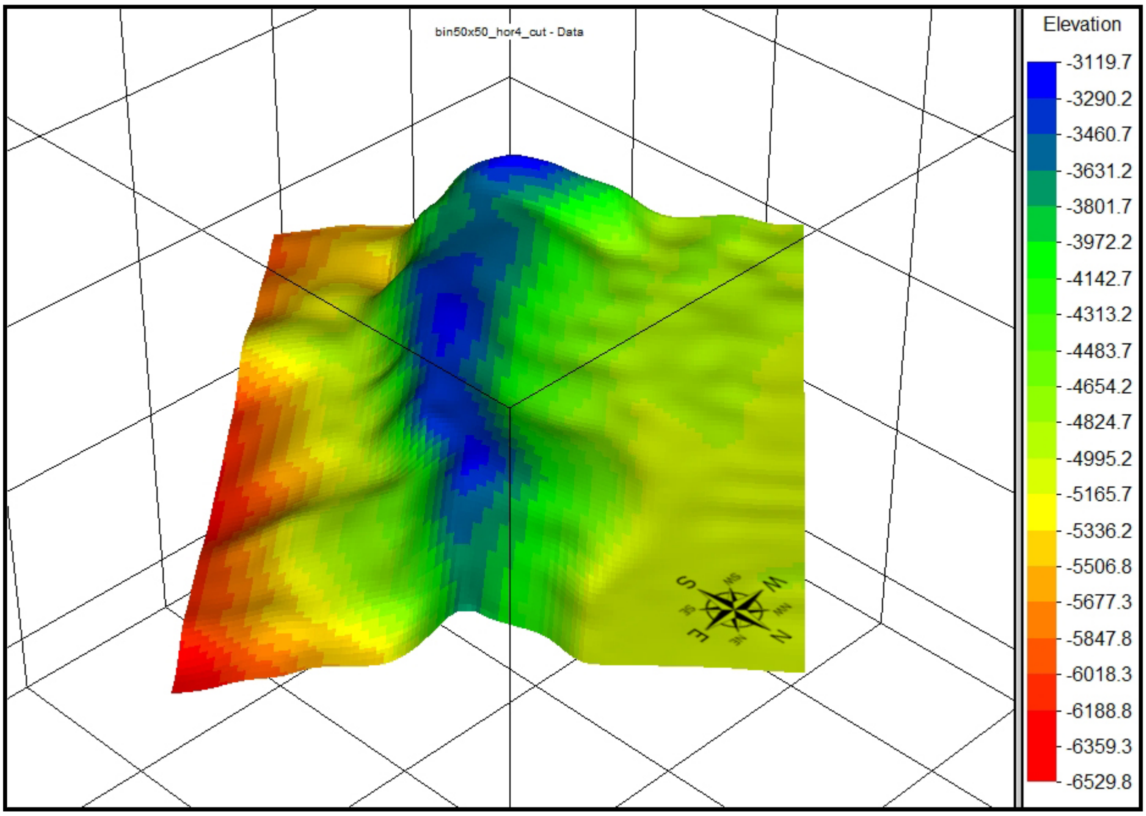

Figure 6-2: Elevation of Horizon 2, which represents the base of the *Giesshübl Monocline* (south-eastern flank), the ridge of the *Reyersdorf dolomite* (from the top of the horizon in northwest direction) and *Flysch* in the north-western flat part. View from northeast.

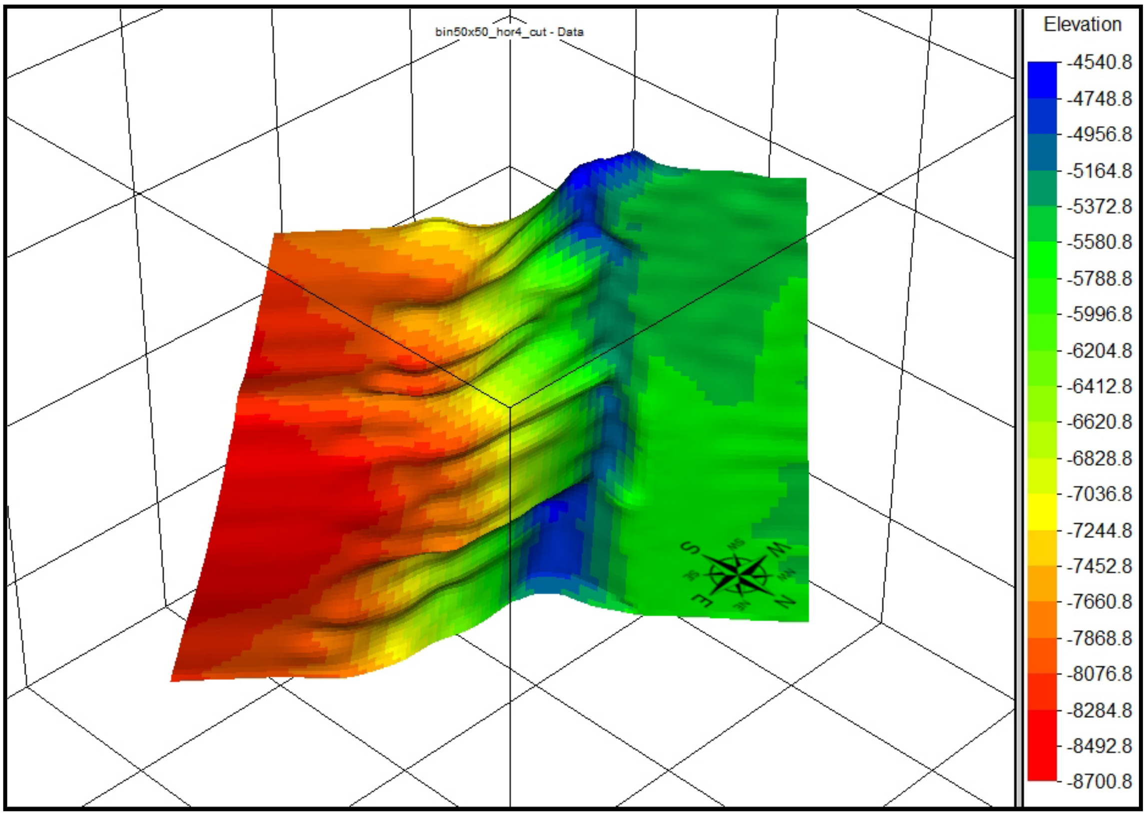

Figure 6-3: Elevation of Horizon 3. The flank represents the base of the *Northern Calcareous Alps (BaseNCA). T*he north-western flat part is *Flysch*. View from northeast.

6.1 BIN SIZE (SPATIAL SAMPLING)

In chapter 3.2 the theoretical background for determining the bin size is given in detail. Therefore equation (3.5) for the unmigrated and (3.6) for the migrated bin size is used. Generally the bin size can be chosen larger, the higher the velocity, the lower the achievable frequency and the smaller the resolvable dip of the subsurface. A large bin size can also affect the lateral resolution, represented with the $\sin(\theta)$ term in chapter 3.4. For calculating the bin size, the velocities and dips of the *target layer* are used. The maximum achievable frequency due to absorption is taken from real data (see chapter 5.2: Seismic 2D-Line).

A flat horizon ($\theta = 0° \; \rightarrow \; \sin\theta = 0$) has an infinite large bin size by using equation (3.5). For this reason *Omni* limits the bin size to a maximum of 500 m.

The screenshots in Figure 6-4 shows the migrated bin size with a limited color scale (10 to 40 m). The horizons are gridded with 50 m x 50 m grid bins. Every grid bin has information of the bin size to sample a seismic wave with the maximum achievable frequency f_{MAX} adequate to avoid aliasing. If the bin size is lower than 25 m the grid bin is blue or white colored. If it is larger than 25 m, the grid bin is colored red and thus sampled correctly.

Several bin size analysis tests on Horizon 2 had shown, that a bin size of 20 m (RI = SI = 40 m) can resolve dips up to 55° and a bin size of 15 m (RI = SI = 30 m) samples dips up to 62° adequate. These specifications are certainly only valid for the used maximum frequency ($f_{MAX} = 31\ Hz$ for Horizon 2).

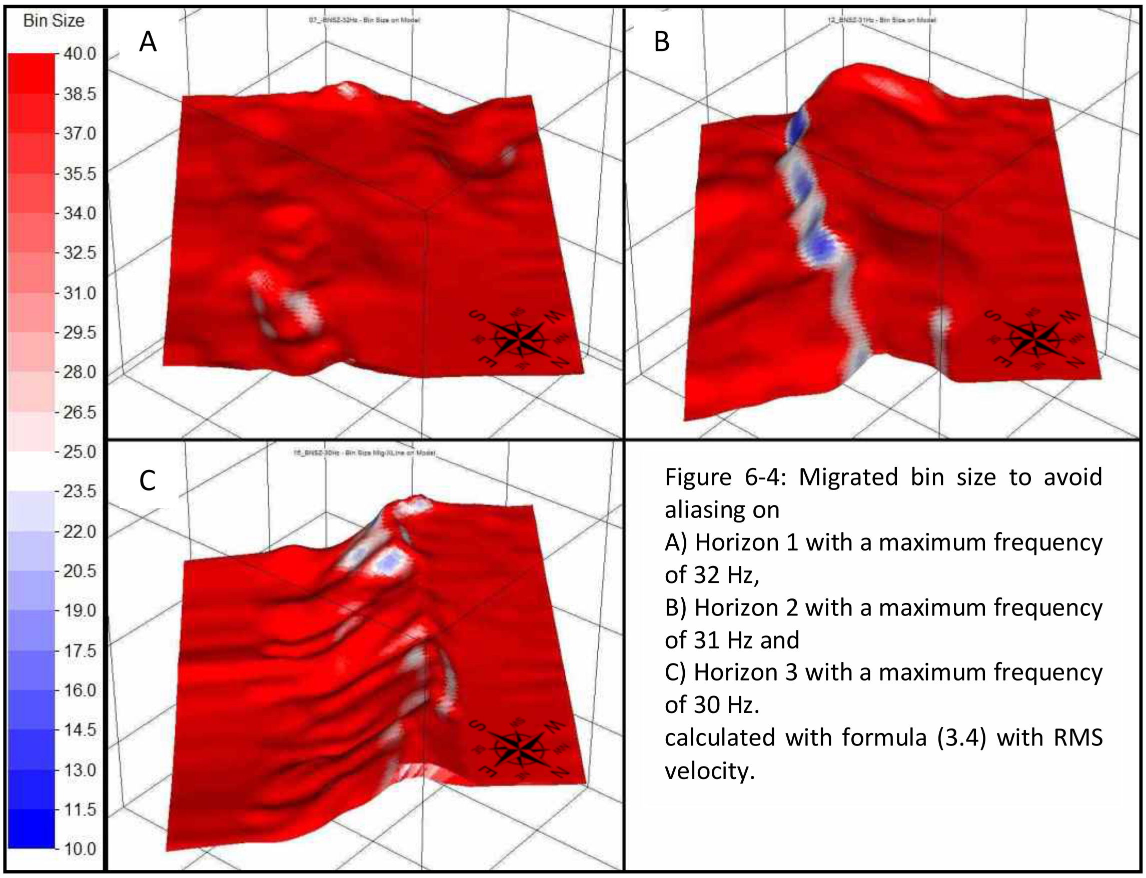

Figure 6-4: Migrated bin size to avoid aliasing on
A) Horizon 1 with a maximum frequency of 32 Hz,
B) Horizon 2 with a maximum frequency of 31 Hz and
C) Horizon 3 with a maximum frequency of 30 Hz.
calculated with formula (3.4) with RMS velocity.

The software calculates the bin size before and after migration. Figure 6-5 shows a histogram of the unmigrated and migrated bin size in comparison for all three horizons. The ordinate counts the number of grid bins for the respective bin size, which is plotted on the abscissa in one meter steps. 72 % of the grid bins of Horizon 1, 54 % of Horizon 2 and 62 % of Horizon 3 containing bin sizes greater than 100 m and are not illustrated in the diagram. The grid bins with small bin sizes corresponds to areas with steep dips. The relation between unmigrated and migrated bin size is given by replacing the sinus with the tangent in equation (3.3), see also CORDSEN et al., 2000, Fig. 2.9). Migration makes a dip steeper (to its true angle) and requires therefore a smaller bin size to avoid aliasing.

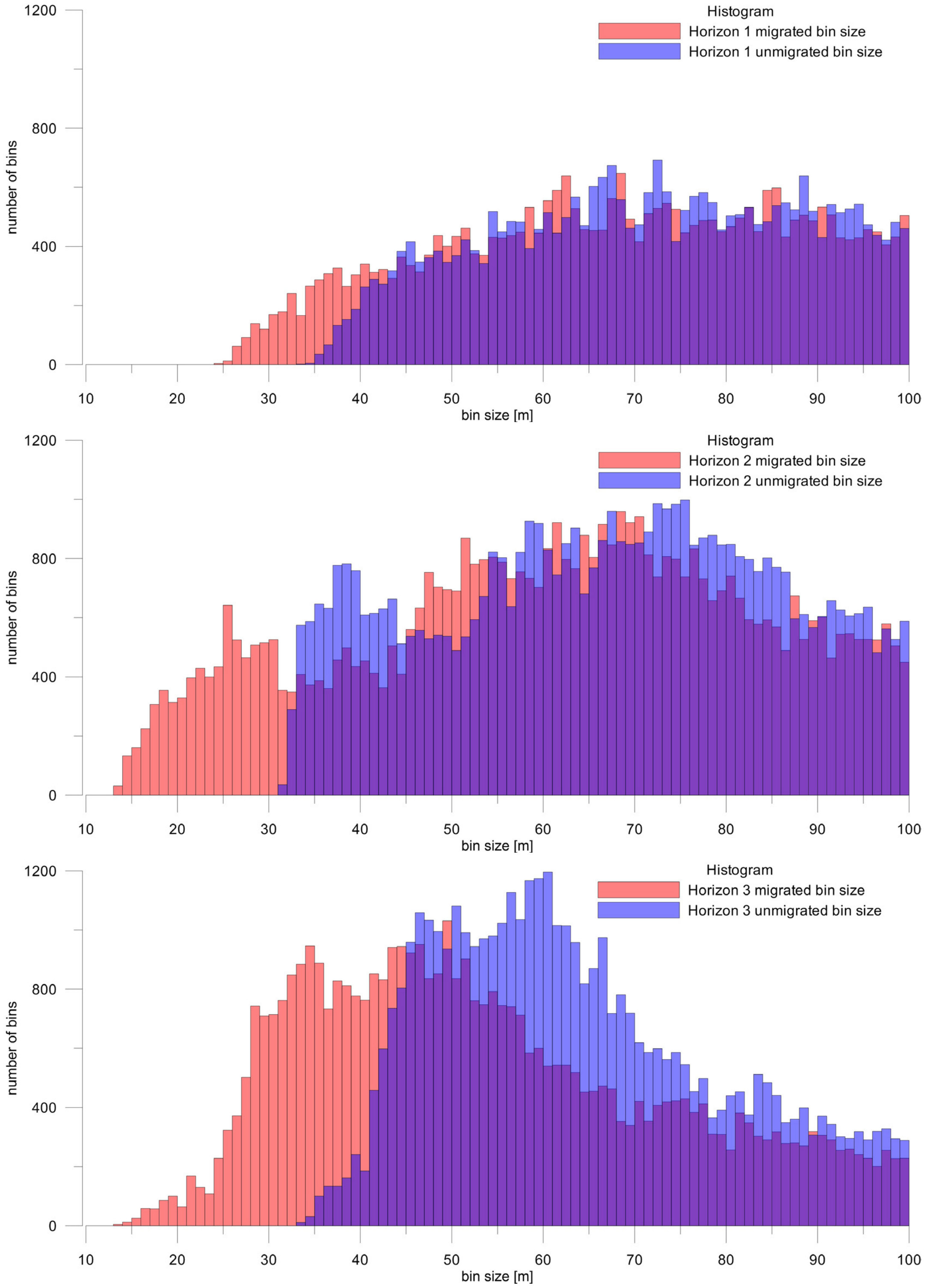

Figure 6-5: Histogram for migrated and unmigrated bin size for Horizon 1, 2 and 3.

Horizon 1 is sampled properly with a bin size of 25 m. To sample the reflected wavefield from Horizon 2 and 3 adequate, a bin size of 14 m is required.

Theoretically, the optimal spatial sampling should record the smallest possible wavelength, given by the lowest velocity and the maximum frequency of the wavefield. To record the full 5D-wavefield (see chapter 4.4) a compromise has to be found between bin size and survey costs, because small bin sizes lead to more active channels or a smaller maximum offset (X_{MAX}). Since very big offsets can be expected for exploring deep horizons, a bin size of 25 m is suggested. Thus 3081 grid bins (2.81 %) of Horizon 2 and 814 (0.74 %) of Horizon 3 will be aliased.

Note: This analysis considers only reflection events. Surface waves (ground roll) have very low apparent velocity, wherefore the receiver intervals must be small to sample the ground roll correctly. If the ground roll is not adequately sampled, there is the danger, that its energy is aliased in f,k-domain and may be folded back to higher frequencies in the area of reflections. To suppress ground roll field arrays (source and receiver arrays) should be considered, which act as spatial anti-aliasing filter. Modern acquisition geometries resigns the use of field arrays and make small sampling intervals (e.g. RI = SI = 10 to 15 m) to record the whole desired wavefield. This leads to higher survey costs and is in the Vienna Basin only possible in a limited way, due to the high cultivation of the area.

6.2 MAXIMUM UNALIASED FREQUENCY

To calculate the maximum unaliased frequency formula (3.4) is converted to:

$$\boldsymbol{f_{MAX}} = \frac{\boldsymbol{v_{RMS}}}{\boldsymbol{4 \cdot B \cdot tan(dip)}} \tag{5.1}$$

The result is the maximum unaliased frequency for a constant bin size, e.g. determined in the previous chapter.

Another input parameter is the time sampling interval (e.g. $SI = 7\,ms$) to get the maximum unaliased temporal frequency:

$$f_{Nyquist} = \frac{1}{2 \cdot SI} = 71.43Hz \tag{5.2}$$

Therefore a temporal sampling interval of 7 ms is theoretically high enough to sample adequate in time domain and get an image beneath the *Neogene Basin Floor*. In practice a standard sampling interval of 2 or 4 ms will be used, to be sure.

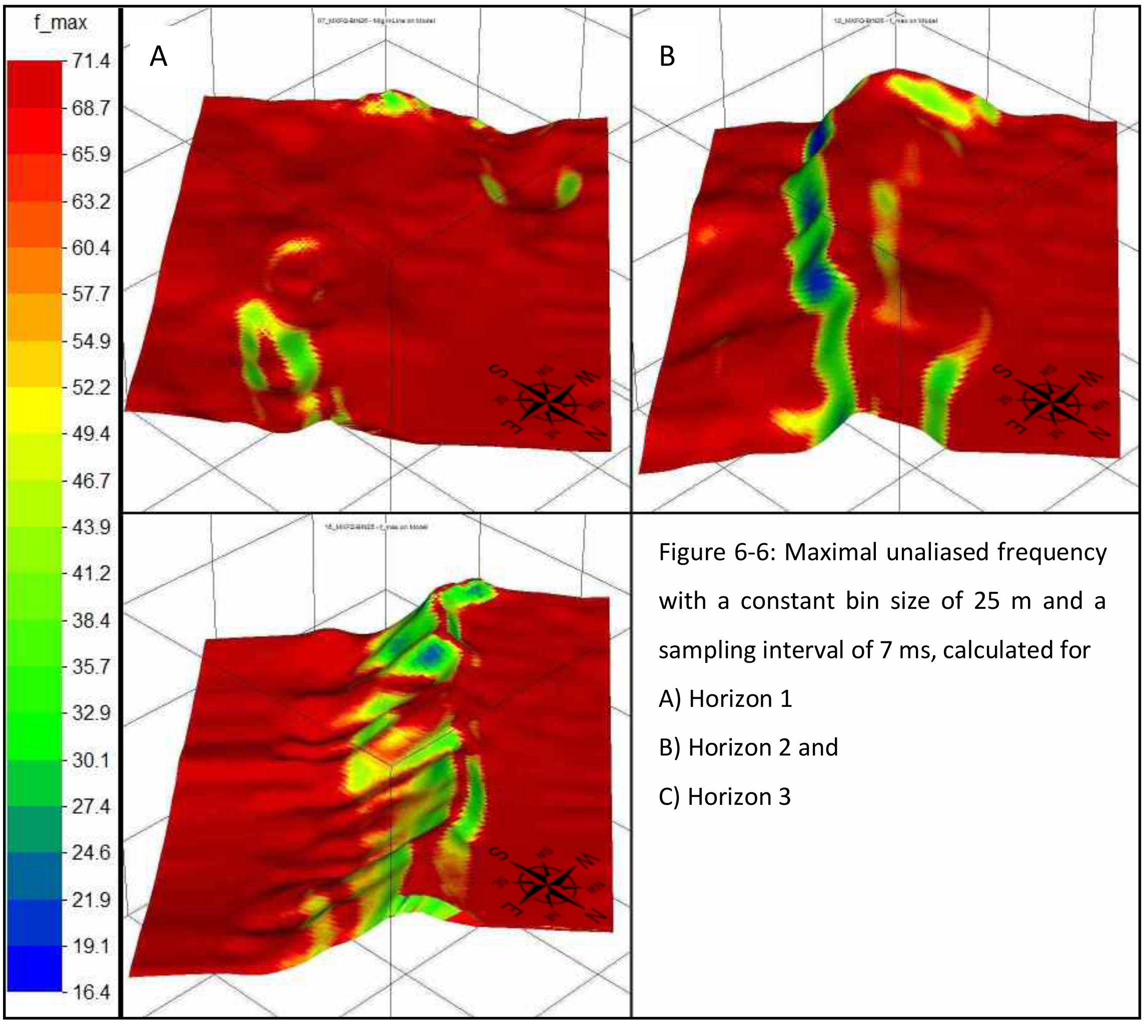

Figure 6-6: Maximal unaliased frequency with a constant bin size of 25 m and a sampling interval of 7 ms, calculated for

A) Horizon 1

B) Horizon 2 and

C) Horizon 3

Figure 6-6 shows the result of the *target analysis* for the maximum frequency, which will not be aliased, if a bin size of 25 m is used. At Horizon 1 the maximum unaliased frequency is higher as the maximum achievable frequency due to absorption (46 Hz, compare with chapter 4.3 and Table 5-1). For imaging the steepest parts of the flank at Horizon 2, a maximum frequency of only 16.4 Hz can be recorded in comparison to the maximum achievable frequency due to absorption of about 31 Hz in this depth (see Table 5-1). Hence, the steep flank will be seen only partially in the seismic section.

For Horizon 3 most parts of the flank can be recorded with its maximum achievable frequency due to absorption of about 30 Hz (see Table 5-1).

6.3 MAXIMUM USEABLE OFFSET

This analysis will determine the maximum useable offset, when a NMO stretch of 30% is allowed. As mentioned in chapter 3.6 the hyperbolic approximation is only valid for small offset-to-depth ratios. If larger offsets want to be used for stacking, a non-hyperbolic approximation must be applied. Further a moveout correction always lowers the signal bandwidth, especially for large offsets and steep dips. However, the results of this analysis are primary used to get an input parameter (the average offset) for determining the spatial resolution in the next chapter. Therefore a NMO stretch of 30 % is chosen as a compromise to get large offsets by holding the frequency decrease low.

The results are shown in Figure 6-7 for the three horizons, for which equation (3.11) is used. It is obvious, that the maximum useable offset is correlating with the depth of the horizon. For Horizon 1, an offset of about 6500 m can be used in the stacking process before the NMO stretch is reaching 30%, whereas an offset of 15000 m can be used for the deep areas of Horizon 3.

Table 6-1 gives the range of the computed maximum offsets, the arithmetic mean value over all grid bins (X_{MAX_AVE}) and the half of the maximum useable offset (X_{MAX_HALF}) per horizon. The latter is used to determine the spatial resolution in the next chapter (see equation (5.3)

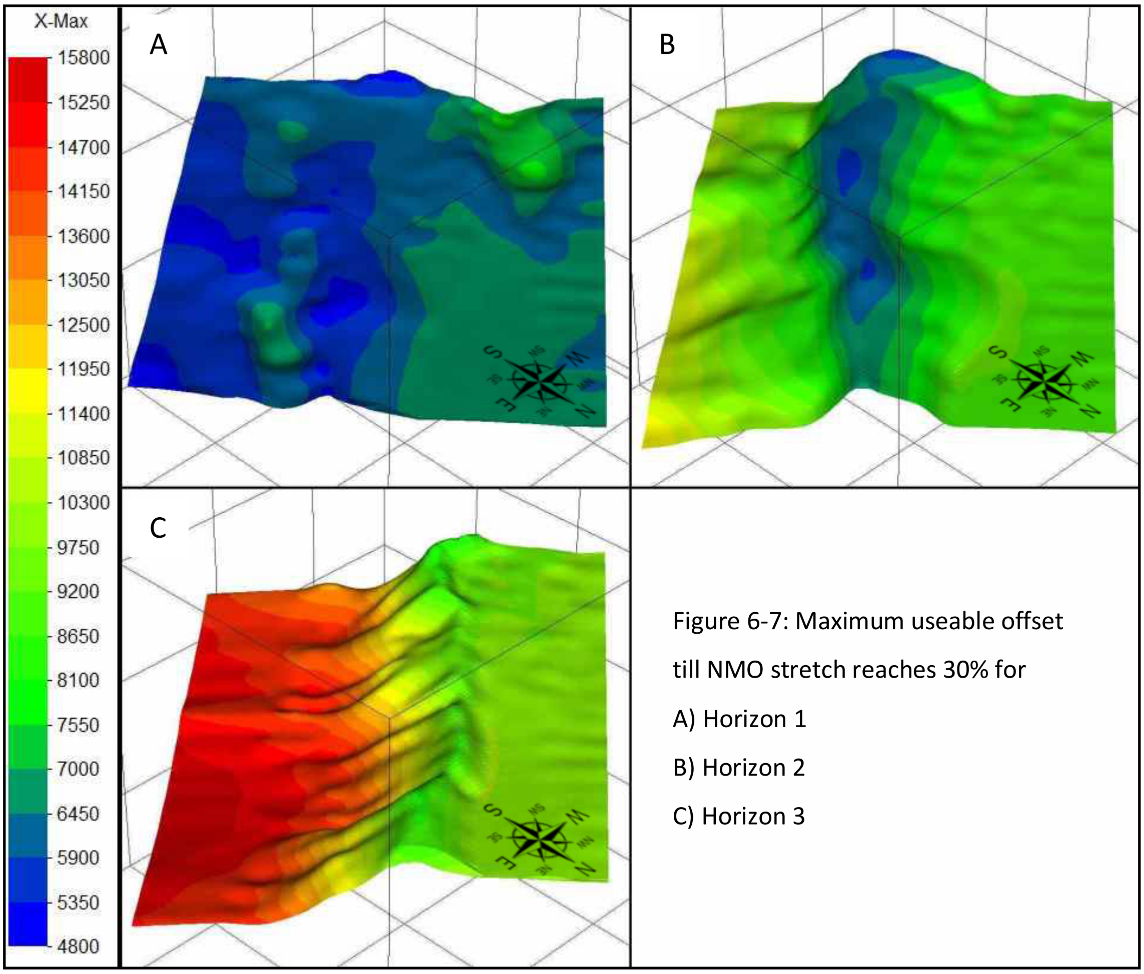

Figure 6-7: Maximum useable offset till NMO stretch reaches 30% for

A) Horizon 1

B) Horizon 2

C) Horizon 3

	Maximum useable offset range X_{MAX}	Arithmetic mean value X_{MAX_AVE}	X_{MAX_HALF}
Horizon 2	6098-6589 m	6416m	3247m
Horizon 3	8810-9141 m	9016m	4570m
Horizon 4	9817-10119 m	10007m	5060m

Table 6-1: Maximum useable offset range, the arithmetic mean value and its half.

6.4 SEISMIC RESOLUTION

The input parameters for calculating the spatial resolution are the maximum frequency, the bin size, a constant c (e.g. Rayleigh constant), the recording time and the *average offset* for each horizon. *Omni* prefers the root mean square velocity rather than the interval velocity in contrary to VERMEER, 2002 for calculating the vertical and lateral resolution. The reason is the same as in bin size determination and is explained in chapter 3.2. The detailed theory about determining the vertical and horizontal resolution is given in chapter 3.4.

<u>Vertical resolution:</u> This is computed with equation (3.8) by using the Rayleigh criterion (c = 0.715) and the RMS velocity. Since there is no $\sin(\theta)$-term in the equation, the recording time and the bin size do not affect the vertical resolution. Further in *target analysis* there is no survey geometry and hence no source and receiver positions specified. Thus the source-receiver angle i is calculated with the aid of the *average offset* (GALBRAITH, 2009). The angle i is defined as the half of the angle of the reflected ray between source and receiver (see Figure 3-7), wherefore the half of the *average offset* X_{MAX_HALF} is used as an input of the software. With the aid of trigonometric functions the angle i is given by:

$$\boldsymbol{i = arctan\left(\frac{x_{MAX\_HALF}}{depth}\right)} \; and \; \boldsymbol{x_{MAX\_HALF} = \frac{x_{MAX\_AVE}}{2}} \qquad (5.3)$$

X_{MAX_HALF} is determined in chapter 6.3, Table 6-1.

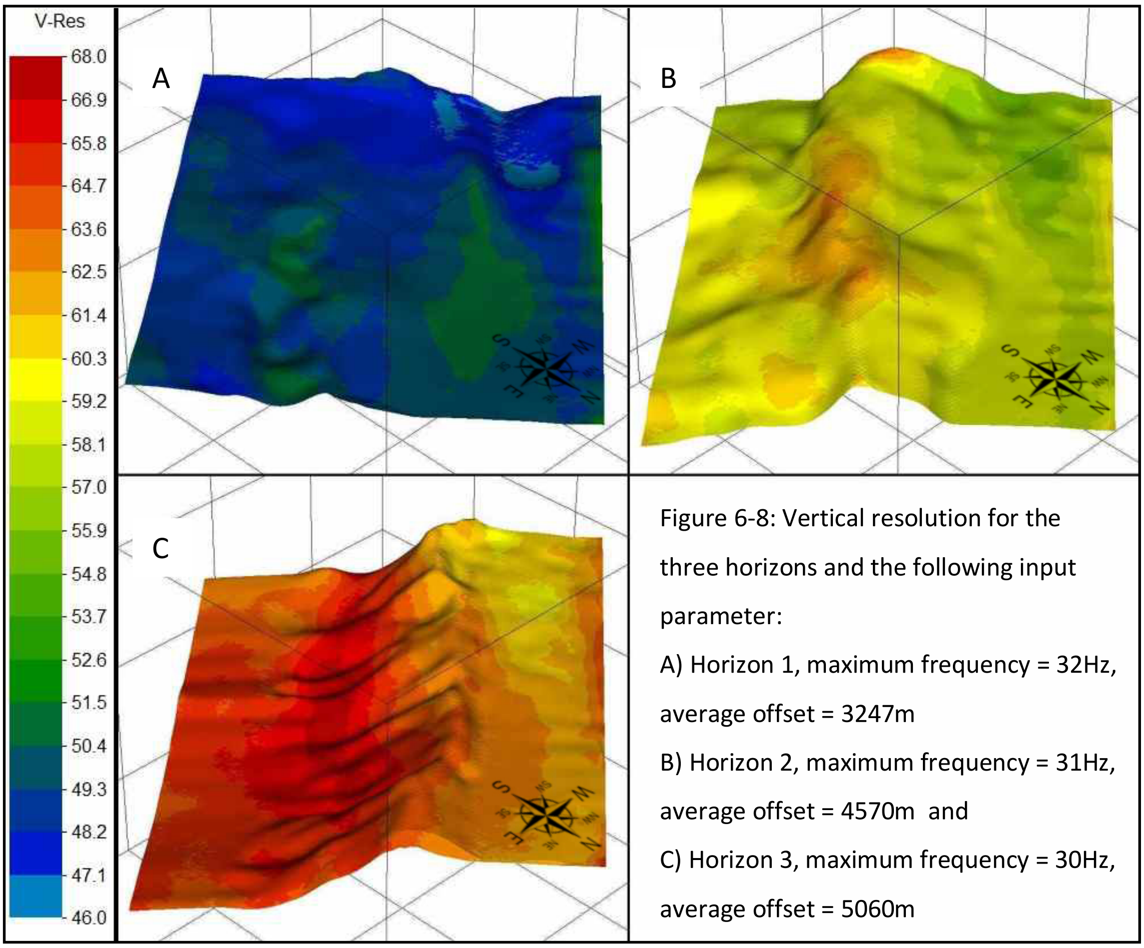

Figure 6-8: Vertical resolution for the three horizons and the following input parameter:

A) Horizon 1, maximum frequency = 32Hz, average offset = 3247m

B) Horizon 2, maximum frequency = 31Hz, average offset = 4570m and

C) Horizon 3, maximum frequency = 30Hz, average offset = 5060m

Figure 6-8 shows the vertical resolution for the three horizons. Horizon 1 can be resolved spatially with 46 to 51 m, Horizon 2 between 55 and 61 m and Horizon 3 with 60 to 68 m. For one horizon the input parameters like frequency, Rayleigh constant and offset are constant, except the RMS velocity and the angle i. Hence the vertical resolution has a correlation with v_{RMS} and the depth.

<u>Lateral resolution after migration:</u>

In equation (3.9) there is the additional term $sin(\theta)$ for the lateral resolution. θ depends on the *minimum distance to the survey edge*, *recording time* and *aliasing angle* (see Figure 3-7), where the smallest of the three values is the crucial factor (GALBRAITH, 2009).

For the reason that *recording time* does not influence the lateral resolution, it is set big enough (10 s), because it should never happen that recording time limits resolution. Now the angle Θ is affected only by two factors: the *minimum distance to the survey edge* (angle from scatter point to the nearest survey edge) and *aliasing angle* (determined with a bin size of 25 m).

Figure 6-9 is representing the lateral resolution. On the pictures it is evident, that in the middle of the *target layer* the *aliasing angle* dominates and on the survey edges the minimum distance to the survey edges is decisive for Θ. If the edge effect is unconsidered, a spatial resolution between 51 and 56 m on Horizon 1, 64 to 75 m on Horizon 2 and 72 to 95 m on Horizon 3 can be obtained.

Tests on Horizon 3 have shown, that a recording time of 7 seconds doesn't affect lateral resolution essentially. A recording time of 6 seconds leads to a worse resolution at the survey corners. Hence, the recording time should be chosen larger than 7 seconds.

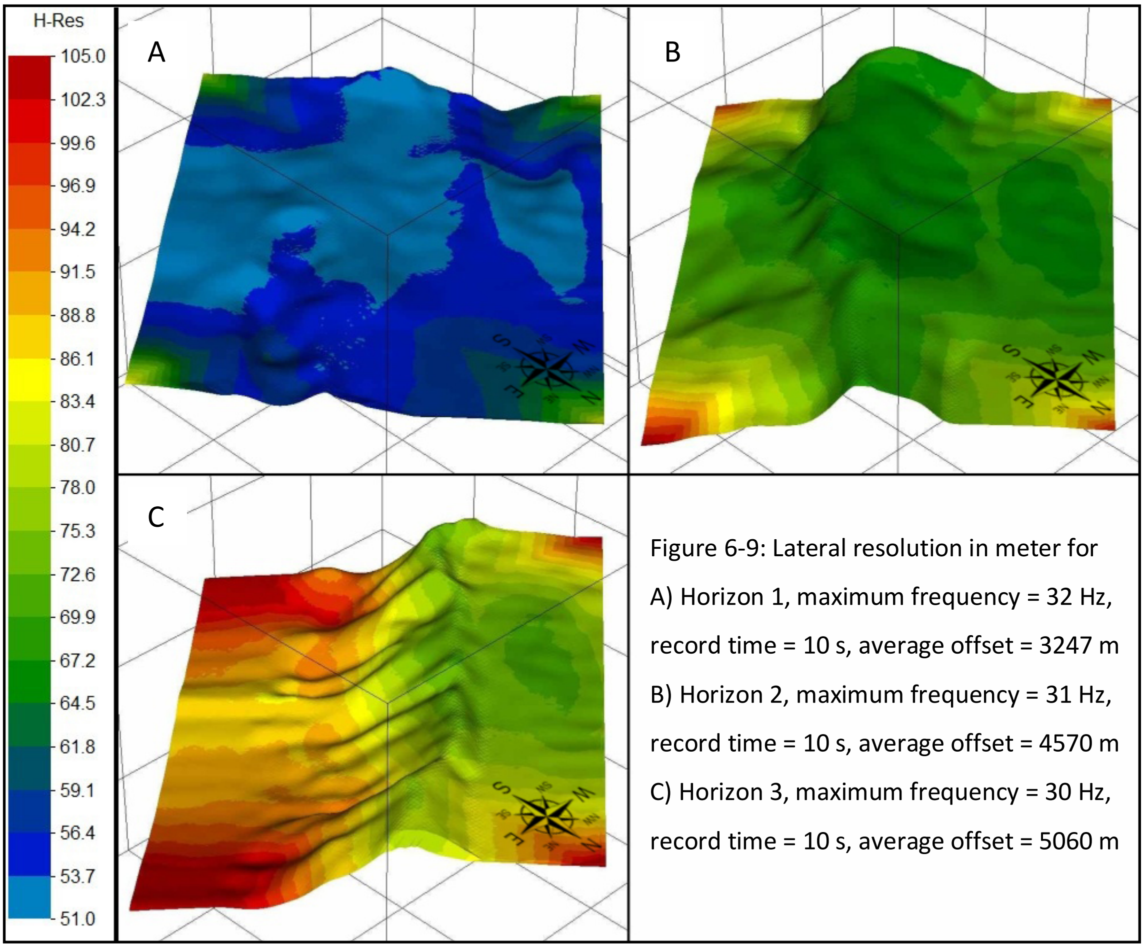

Figure 6-9: Lateral resolution in meter for
A) Horizon 1, maximum frequency = 32 Hz, record time = 10 s, average offset = 3247 m
B) Horizon 2, maximum frequency = 31 Hz, record time = 10 s, average offset = 4570 m
C) Horizon 3, maximum frequency = 30 Hz, record time = 10 s, average offset = 5060 m

6.5 AMPLITUDE LOSSES

A further possibility in *target analysis* is the determination of amplitude losses due to attenuation. Input parameters are therefore dominant frequency, target reflection coefficient and quality factor Q.

Absorption losses:

As described in chapter 4.3 this form of amplitude losses are due to absorption, which is material dependent. The main parameters are the quality factor Q and the dominant frequency. For calculate the absorption the software offers two options: Set a constant Q or a variable Q, where latter is taken from the velocity model. Some experiences had shown, that the result is exactly the same, when using a constant Q of 50 or the variable Q values from the velocity model. This is not realistic since the smallest value of Q in the velocity model is 70. This may be a bug in the program and hence the option with the constant quality factor is used in the following.

As a compromise the average quality factor Q_{AVE} was calculated (see Figure 6-10) in analogy for calculating the average velocity:

$$Q_{AVE,i} = \frac{\sum_{k=1}^{i}[Q_k \cdot (d_k - d_{k-1})]}{d_i} \tag{5.4}$$

where i is the depth sampling point of the velocity model. Hence, for each layer a constant Q_{AVE} is taken, which corresponds to the average depth of the *target layer*. This method can be justified in analogy to equations, which are designed for a constant velocity earth but are used for varying velocity models just by taking the average or root mean square velocity. The approximation method is the same.

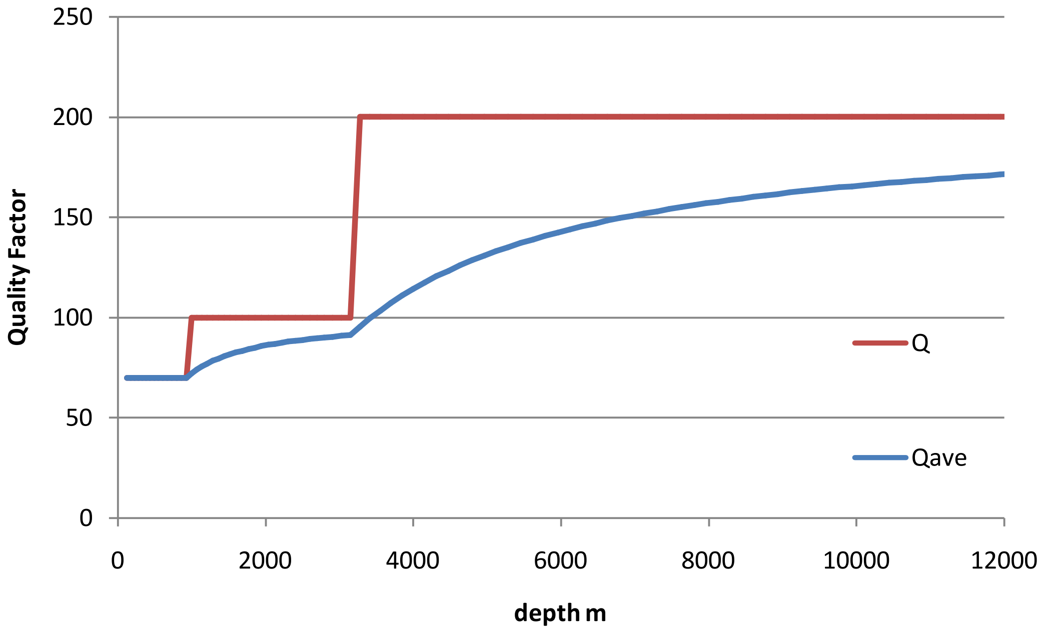

Figure 6-10: Quality factor Q and average quality factor Q_{ave}

Figure 6-11 shows the result of the absorption analysis for the three horizons. The result is adapted for a dominant frequency of 20 Hz and a constant quality factor Q_{AVE} per horizon. The amplitude losses of Horizon 1 due to absorption ranges from -12 to -16 dB, those of Horizon 2 are between -12 to -18 dB and those for Horizon 3 ranges from -14 to -20 dB.

The relation of Decibel and amplitude ratio is given in equation (4.17). -20 dB corresponds to an amplitude ratio of 10, where the amplitude of the recorded signal is

$1/10$ of the amplitude of the source signal. -12 dB corresponds to an amplitude ratio of 4.

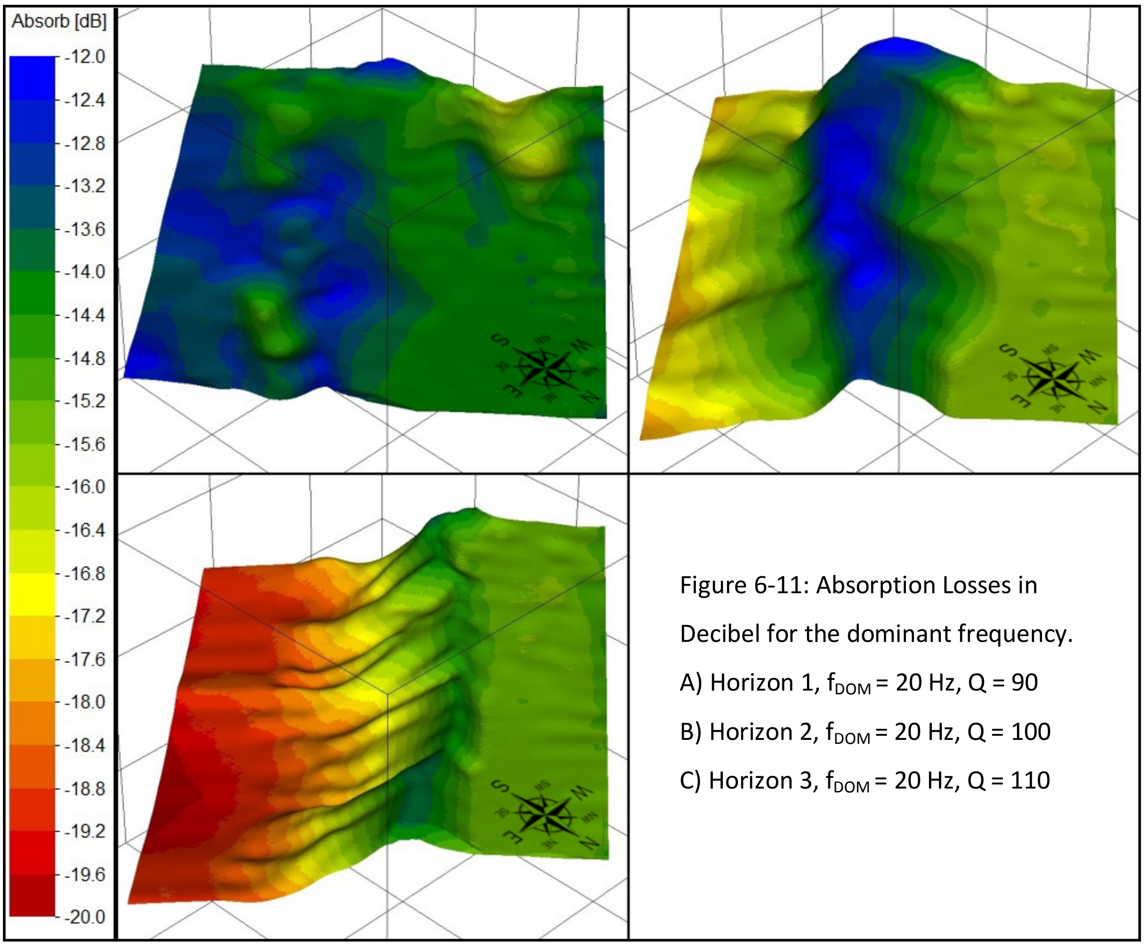

Figure 6-11: Absorption Losses in Decibel for the dominant frequency.

A) Horizon 1, f_{DOM} = 20 Hz, Q = 90

B) Horizon 2, f_{DOM} = 20 Hz, Q = 100

C) Horizon 3, f_{DOM} = 20 Hz, Q = 110

Spherical Losses:

The amplitude loss due to geometrical spreading (also see chapter 4.3) of the spherical wave is higher, as longer the travelling distance. A plane wave does not have energy losses, because the wave front area does not increase with the distance. This means, that the spherical loss will only occur on the way from the source to the reflector, where the amplitude decreases with $1/r$ (in a constant velocity medium). The three horizons of interest are deep, which means, that the amplitude losses of the signal will be high. The results of spherical losses of the amplitude are shown in Figure 6-12. It shows the effect of amplitude only due to geometrical spreading and is therefore independent of the wave's frequency. The losses range from -23 dB on Horizon 1 up to -33 dB on Horizon 3, which corresponds to the amplitude ratio from 14 to 44.

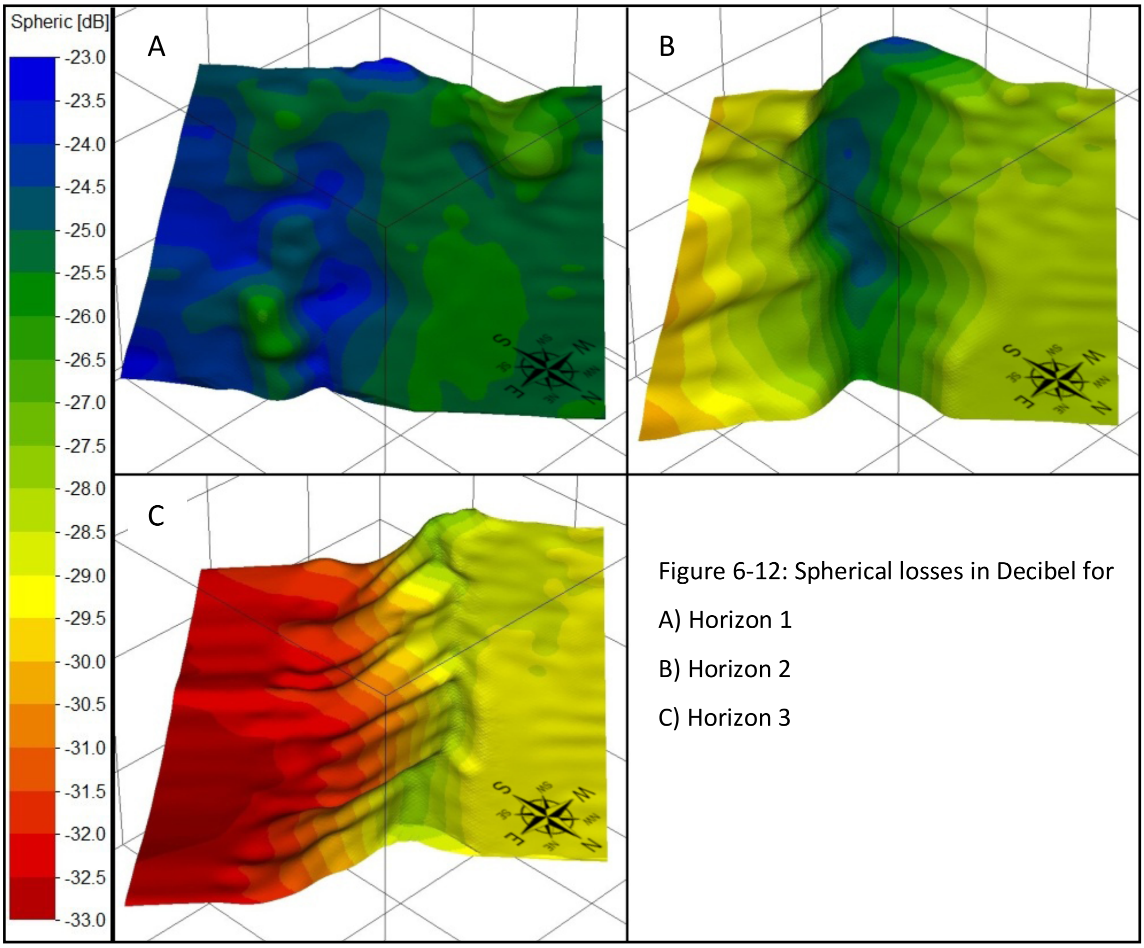

Figure 6-12: Spherical losses in Decibel for

A) Horizon 1

B) Horizon 2

C) Horizon 3

Generally the amplitude losses for the deep *target layers* are relatively high. Due to absorption the signal is bandwidth limited and causes a maximum achievable frequency of 32 Hz. A high signal bandwidth is desirable, which leads to a sharper signal and thus to a better resolution. Additionally, the spherical losses are up to -33 dB and a further great amplitude loss will occur in the transition through the *Neogene Basin Floor*, due to the high impedance contrast, where most of the energy is reflected.

As a counteraction, a high fold should be requested, to increase the signal to noise ratio and to raise low amplitudes after stacking. Also multiple sources and vertical stacking can help to raise the S/N ratio (see chapter 3.3).

6.6 MIGRATION APERTURE AND MIGRATION APRON

The input parameter to calculate the *migration aperture* of a *target layer* is the *migration angle*, which is also called diffraction angle. The standard value for the migration angle can be found in literature, e.g.: *"A migration aperture of 30° is often a good compromise and will capture most of the diffracted energy. However, steeper dips require a larger migration aperture."*[12] Although there are steep dips, the standard *migration angle* of 30° is used for this analysis.

The exact formula, which *Omni* uses to calculate the *migration aperture,* could not been determined. The support team affirms: "*OMNI picks a subsurface point, then ray traces through the model to the surface. Thus it does take ray bending into a*ccount."[13]

Experiences and tests confirmed, that for a horizontal layer with 1D velocity information, *Omni* delivers the same result as calculated with formula (3.13). It is conceivable, that if a 3D velocity model is assigned to a *target layer*, the *migration aperture* is calculated in all 4 orthogonal (or even more) directions and thus taking the largest result.

Figure 6-13 shows the result of *migration aperture analysis* on the three main targets. Every grid bin has now information of the radius (offset at the surface), which is required to record a 30° diffraction with its origin at the grid bin depth. The size of the migration apertures are correlating in a high degree with the depth lines (compare with Figure 6-1, Figure 6-2 and Figure 6-3) and are therefore calculated without considering the dip (starting angle is 30°). However, the results are plausible, because the main dips are in the middle of the investigation area. The migration aperture of the horizons are ranging from 1616 m to 3675 m. To demonstrate the size of the *migration apron* (definition see tables in chapter 1) a script in PERL (Figure 6-14) determines the minimum distance to the survey edge and plots those vectors (magnitude = migration aperture, direction = shortest way to the survey edge) which are going outside of the investigation area (see Figure 6-15). Due to clearness only every 50th vector is plotted.

---

[12] VERMEER, 2002, p.78, chapter 4.4.2.1

[13] GALBRAITH, M., WILLSON, N.; 2009: Email from support@gedco.com from 28th October

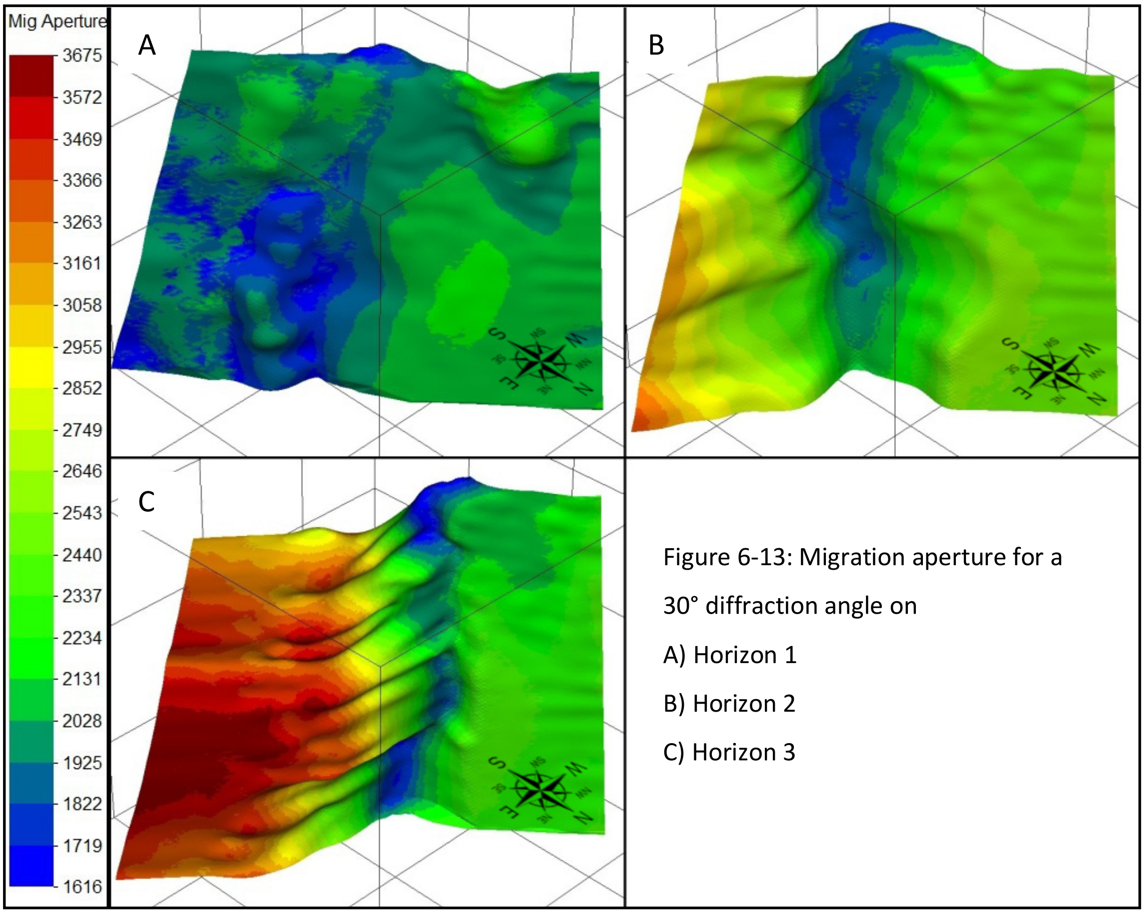

Figure 6-13: Migration aperture for a 30° diffraction angle on

A) Horizon 1

B) Horizon 2

C) Horizon 3

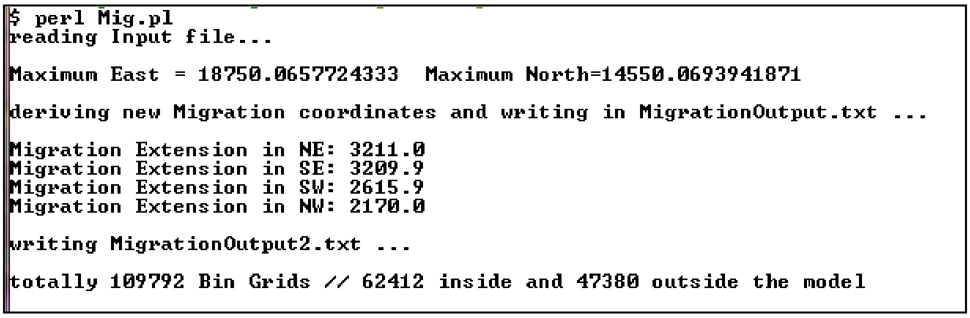

```
$ perl Mig.pl
reading Input file...

Maximum East  = 18750.0657724333   Maximum North=14550.0693941871

deriving new Migration coordinates and writing in MigrationOutput.txt ...

Migration Extension in NE: 3211.0
Migration Extension in SE: 3209.9
Migration Extension in SW: 2615.9
Migration Extension in NW: 2170.0

writing MigrationOutput2.txt ...

totally 109792 Bin Grids // 62412 inside and 47380 outside the model
```

Figure 6-14: Script in PERL deriving the migration apron and hence the maximum migration extensions in every 4 directions. This example shows the program output display for Horizon 3.

The investigation area covers 14.6 km x 18.8 km = 274.4 km². In respect to the migration apron the survey area has to be 20.7 km x 25.5 km = 527.8 km². The extension has to been made from the *nominal fold* area (see Figure 7-5), which reduce the extension to about 18.6 km x 24.8 km = 461 km². This should be enough to get an image of the *nominal fold* area. Optionally (to decrease survey costs), the area of interest could be reduced in strike-dip direction (NE and SW side), which yields to a minimum survey area of about 19 km x 22 km = 418 km².

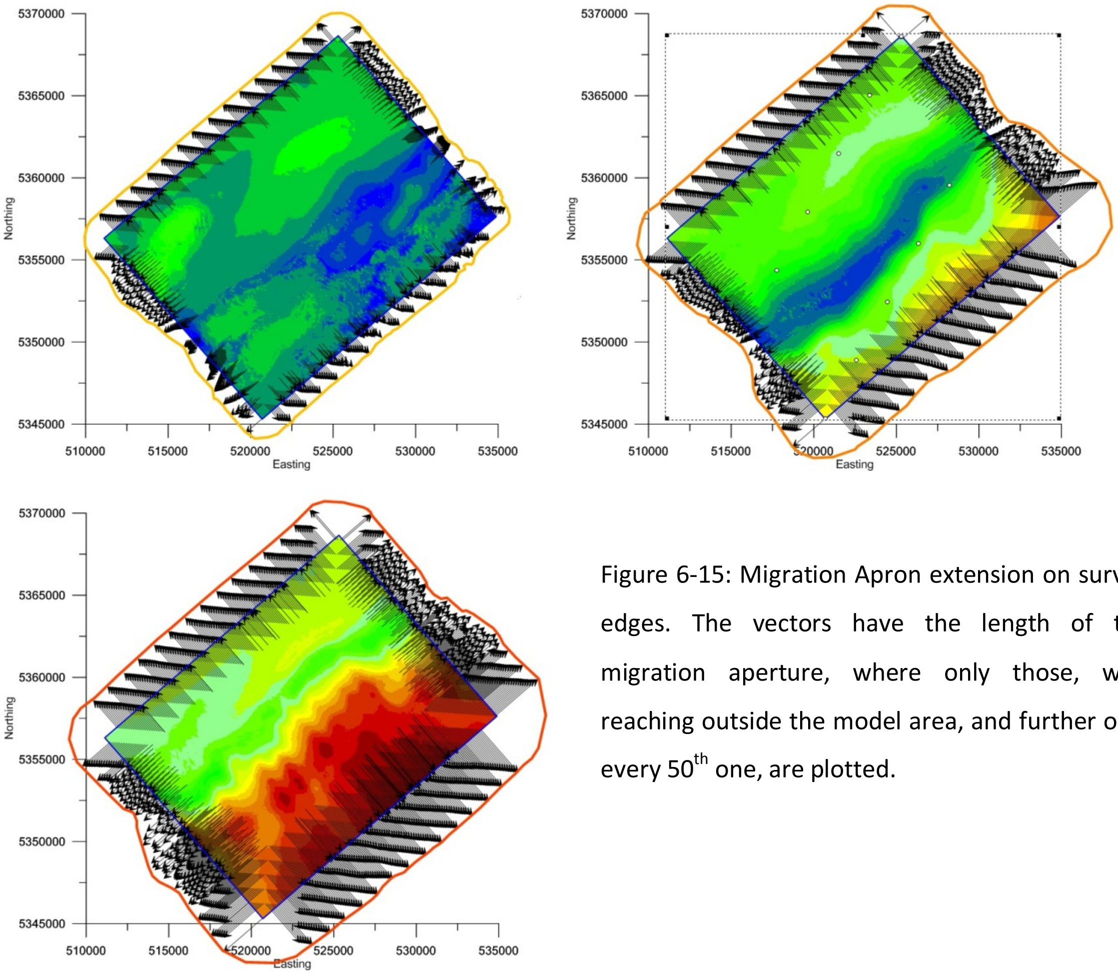

Figure 6-15: Migration Apron extension on survey edges. The vectors have the length of the migration aperture, where only those, who reaching outside the model area, and further only every 50th one, are plotted.

6.7 SUMMARY OF ARCHIEVED PARAMETERS AND DISCUSSION

Table 6-2 gives overview of the determined parameters from *target analysis* and some general parameters for the survey design. The bin size is adequate to image reflections on the respective horizon without aliasing. The maximum unaliased frequency for each horizon is given in respect to a bin size of 25 m in comparison to the maximum achievable frequency due to attenuation from chapter 5.2. Further important parameters, like the vertical and horizontal spatial resolution and the maximum allowed offset for a 30% NMO stretch, are given. The survey extension in four orthogonal directions from the investigation area is given for a 30 degree diffraction from the reflection point.

		Horizon 1	Horizon 2	Horizon 3
Bin size before migration	m	35	31	33
Bin size after migration	m	25	14	15
Maximum frequency due to aliasing[14]	Hz	50	30	32
Maximum frequency due to attenuation	Hz	32	31	30
Vertical Resolution	m	46-51	55-61	60-68
Horizontal Resolution[15]	m	51-56	64-75	72-95
Maximum offset, due to 30° NMO stretch	m	6416	9016	10007
Max. Migration Apron (NE)	km	1.5	3.2	3.4
Max. Migration Apron (SE)	km	1.4	3.2	3.7
Max. Migration Apron (SW)	km	1.8	2.6	3.3
Max. Migration Apron (NW)	km	1.5	2.2	2.4
		General Parameters		
Station interval (RI, SI)	m	50		
Line interval (RLI, SLI)	m	1000		
Maximum recording time	s	10		
Temporal sampling interval	ms	4		
Nyquist frequency	Hz	125		

Table 6-2: Received parameters from *target analysis*, the maximum frequency due to attenuation from Table 5-1 and general recommended parameters for the survey design.

Discussion:

To ensure, that the maximum frequency due to attenuation can be sampled properly, after Table 6-2, the bin size has to be set to 15 m. This will lead to a high number of receivers in respect to the required maximum offset. In chapter 3.2 the justification for taking the RMS velocity instead of the interval velocity is given, which means, that the bin size is calculated with safety reasons. Hence, the final bin size is set to 25 m, which corresponds to a receiver and shot station interval of 50 m. Therefore the most parts of the flanks should be imageable without spatial aliasing. Thus field arrays for source and receiver are suggested to suppress ground roll and other noise. Without field arrays a much smaller source- and receiver interval will be necessary.

Further, a receiver- and source line interval of 1000 m should be sufficient, thus after the rule of thumb in chapter 3.5 the shallowest imageable horizon will be 1400 m beneath the surface. Symmetric sampling is one of the most important characteristics of a survey (see chapter 4.4), hence SI = RI, SLI = RLI and a wide azimuth pattern (aspect ratio 0.8 to 1.2) has to be used.

---

[14] except dips > 50°

[15] without Edge-Effect

The rule of thumb of chapter 3.6 implies, that the maximum offset of the pattern should be the same magnitude as the deepest horizon that wants to be mapped, which is in this case in 8700 m depth. The maximum useable offset to allow a 30% NMO stretch is 10000 m. If this is high enough, or if even a smaller offset can be used will be analyzed in the next chapter with the aid of ray tracing.

The determined resolution is relatively worse and may be a criterion if the survey is carried out. But one should consider, that the calculation of the resolution have some uncertainties, e.g. the source and receiver angle i determined by the *average offset*, the interpretation of the Rayleigh constant c or taking the RMS velocity. However, the variation to reality will not be high.

The migration apron is already discussed in chapter 6.6 with the consequence, that the survey area has to be nearly doubled (minimal factor 1.5) to allow proper migration of the investigation area.

A recording time of 6-7 seconds with a temporal sampling interval of 7 ms is minimal required for reflections in the deep basin, which corresponds to the maximum resolvable frequency (Nyquist frequency) of 71.4 Hz in time domain. Nevertheless the standard sampling interval of 4 ms ($f_{Nyquist}$ = 125 Hz) is recommended and hence a recording time of 10 s.

7 ILLUMINATION ANALYSIS AND PATTERN DIMENSIONING

By using the spatial sampling interval (SI, RI) and the line interval (RLI, SLI), which are determined in the previous chapter, a survey (source-, receiver- and line layout) can be created. The next step is to determine the pattern size or respectively the maximum required offset, which defines the number of receivers and hence the survey costs. Generally, the required offset is as larger as deeper the target and is further coupled with the *fold* (for a given RI, SI, RLI and SLI). A high fold increases the signal to noise ratio, which is necessary to get the achievable resolution from chapter 6.4.

The *illumination analysis* calculates the reflection points of a subsurface layer for a defined survey layout and sums all points, which are hitting one grid bin. The idea is, to calculate the illumination for the layers of interest for an all-live pattern. The result quantifies the maximum possible illumination (fold of reflection points) for the specified survey layout. Then the pattern size (the maximum allowed offset) is reduced step by step and the final pattern size is selected by comparing the illumination results.

The illumination analysis will be applied on four layers: Horizon 1 (*Neogene Basin Floor*), Horizon 2 (between Horizon 1 and 3), Horizon 3 (*BaseNCA*), and a further layer in the middle of the *Neogene Basin fill*, which is called Horizon 0. This horizon is the layer with a constant velocity of 3500 m/s and was extracted with GOCAD from the smoothed velocity model.

To get a meaningful illumination result, at first the different ray tracing options are worked out and compared. It is essential to rebuild the velocity model to a constant-velocity layered model, called *3d ray model*. Since the company of the used software does not reveal references of their ray tracing algorithm, a benchmark with a well proven algorithm is made, which is based on Vidale and can handle even large velocity contrasts (up to 1:4).

The results and many tests show that some ray tracing algorithms may get unstable for steeper dips and also the calculation time may play a major role.

Finally the results of illumination with adequate accuracy and affordable calculation time are presented and further compared with the illumination of the already field-tested survey design, which was designed and carried out 25 years ago to measure the *Neogene Basin fill* (*Neogene Basin Survey).* Thus the required maximum offset for the *Deep Basin Survey* can be determined.

7.1 PRINCIPLES AND DIFFERENT RAY TRACING ALGORITHM

As mentioned, the result of illumination analysis is dependent on the survey layout. First the survey has to be defined, where source and receiver positions and shooting strategy have to be specified. Then the ray tracing algorithm is looking for the ray paths of the wave for every shot- and receiver pair and stores the reflection points (CDPs). Finally the number of reflection points for every grid bin is counted and called *migrated fold* or illumination.

Creating a new survey in OMNI is fast and simple by using wizards. The survey can be defined by the input values X_{MIN}, X_{MAX} and the bin size, or by inline and crossline fold, X_{MAX}, and the bin size or by receiver- and source line interval and receiver- and source interval. X_{MIN} and X_{MAX} are the minimum and maximum offset (see chapter 3.1).

The horizons to analyze may exhibit significant topography, but have to be a single-valued function of easting and northing ($z = f(x, y)$). This means, the horizon may not fold back upon itself and has to extend the whole survey area.

To remember the Omni specific nomenclature, see also chapter 5.3.

Omni provides three main ray-tracing options (see Figure 7-1):

1. Stacking fold or fold before migration. The analysis is applied on a *target model*, where the CMP`s (common midpoints) are mapped on the layer. This method doesn`t use velocity information and is not useful for this work.

2. Simple migrated fold on a *target layer*: Within this option two ray tracing methods are possible:

b.) Straight Ray: In this case shot and receiver elevations attributes are used, but the ray paths are straight, i.e. the velocity model defined in the *target layer* is ignored and a specific constant velocity is assumed. This method is not useful for this work.

a.) Curved Ray: The ray-tracing algorithm uses the velocity model, defined in the *target layer*, hence the rays will be curved. The shot- and receiver position will be assumed to be at the elevation of the velocity model datum (SRD). The input parameters for this analysis are "maximum iterations" and "iteration accuracy". This method can be useful for this work.

3. Complex migrated fold on a *3d ray model*: This is full three dimensional curved ray tracing. Both shot and receiver elevations are used and the rays are traced curved through the *3d ray model,* which includes the velocity information. The reflecting horizon can be defined as a layer within the *3d ray model*. This method is useful for this work and is called *standard algorithm* in the following. Within this option there are further two advanced settings, which enhance the *standard algorithm*:

a.) Intensive search: This option can be activated by clicking "3d ray model style" on "ray trace parameters" tab. If this option is chosen, a different algorithm is used to find the ray paths (according to *Omni* help). The support gives a bit more information: *"The intensive search algorithm attempts to find rays even if the original approximation fails. We have refined the method in recent versions, so this setting should not increase the number of reflections significantly."*[16]

b.) Multiple rays: When this option is activated, the ray search is started in multiple areas of the horizon looking for local minima. It tries to find up to 10 reflection points per source-receiver pair.

Four different ray tracing options seem to be useful for this work: *curved ray*, *standard algorithm*, *intensive search* and *multiple rays*. The next chapters will focus on testing

---

[16] HUNT, J.; 2010: Email from support@gedco.com from 27th January

and comparing the algorithms to find out the best way to illuminate the *deep Vienna Basin*. But at first, a *3d ray model* for option three is required.

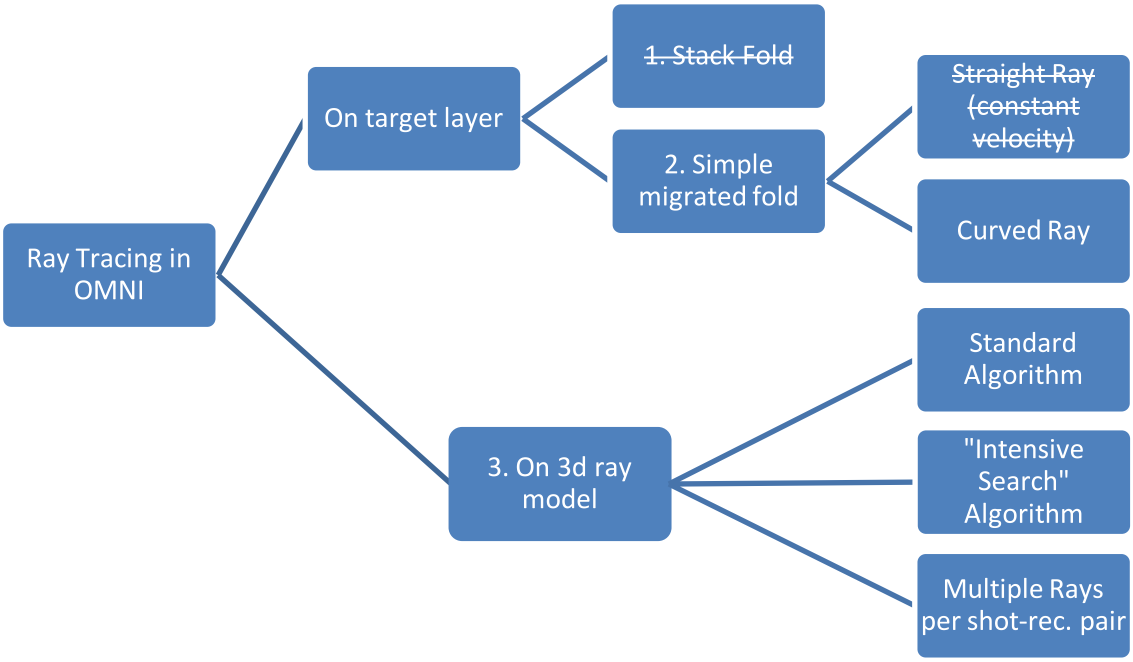

Figure 7-1: Different illumination options in Omni. The not useful options for this work are crossed out.

7.2 DATA PREPARATION - BUILDING A 3D RAY MODEL IN OMNI

For applying the illumination analysis on a *3d ray model* (constant velocity layered), the velocity model has to be rebuilt, and therefore some approximations and limitations has to be made. The *3d ray model* is constructed by extracting constant velocity layers with GOCAD.

Creating a *3d ray model* has several specification and limitations:

- Generally layers can be created by defining a mathematical function, a dipping plane, a ridge or dome, or by interpolating from xyz points.
- Before defining layers the model extension and resolution has to be defined. The maximum number of layers is limited to 19.

- For each layer the velocity (for P and S waves) and the density have to be defined. These properties are constant from one layer to the next layer.
- Each layer has to extend the whole model dimension (investigation area) and z has to be a function of x and $y \rightarrow z = f(x, y)$. This means the lateral velocity discontinuities of the velocity model can only be approximated with the function *clipping*.

Clipping: If two layers are crossing in z domain the upper layer huddles to the lower layer or vice versa. The space between upper and lower layer (*clipping area*) is 10 m, which represents a thin layer with incorrect velocity.

Figure 7-2 gives an example of two clipped layers. Figure 7-3 shows the velocity model and the *3d ray model* with *clipping* in comparison. It seems to be a good approximation for the velocity model, but in closer inspection one can see, that the clipping areas have the wrong velocity. Some ray tracing tests had shown, that the ray tracing algorithm is sometimes "irritated" within the *clipping area* and hence many rays are missing. Therefore the *3d ray model* has to be constructed without clipping, which leads to a higher approximation level. In the following the model without clipping is called *simplified 3d ray model* and is illustrated in Figure 7-4. Additionally the four analyzed horizons are marked.

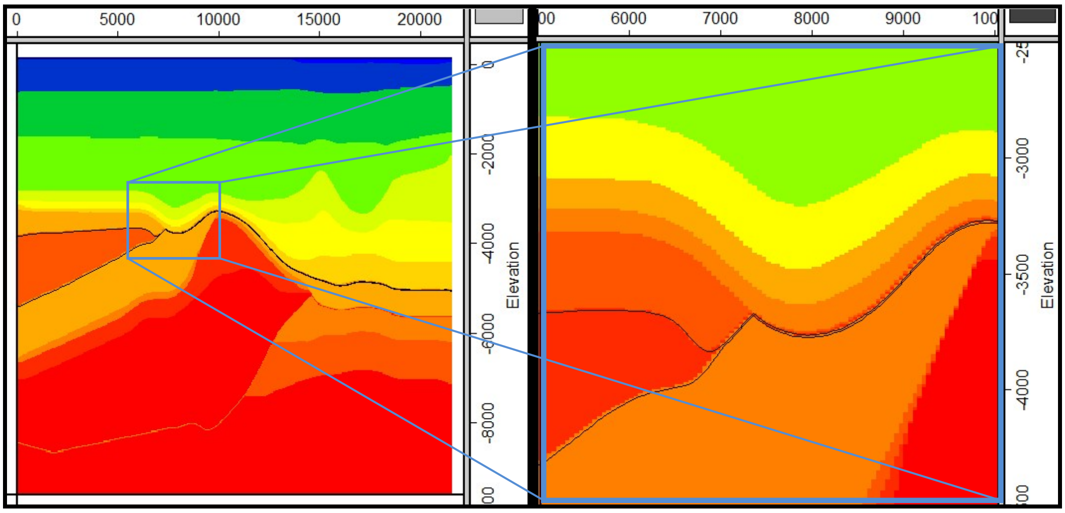

Figure 7-2: Example of clipping layers: The lower black marked layer is clipped to the upper layer. Zoomed view on the right.

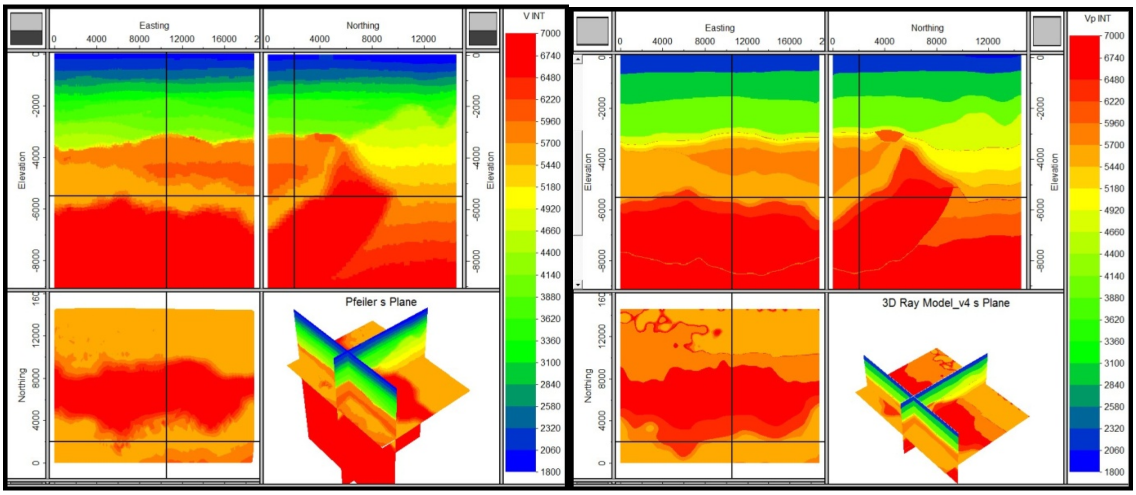

Figure 7-3: Original velocity model on the left versus the constant-velocity layered 3d ray model with clipping on the right.

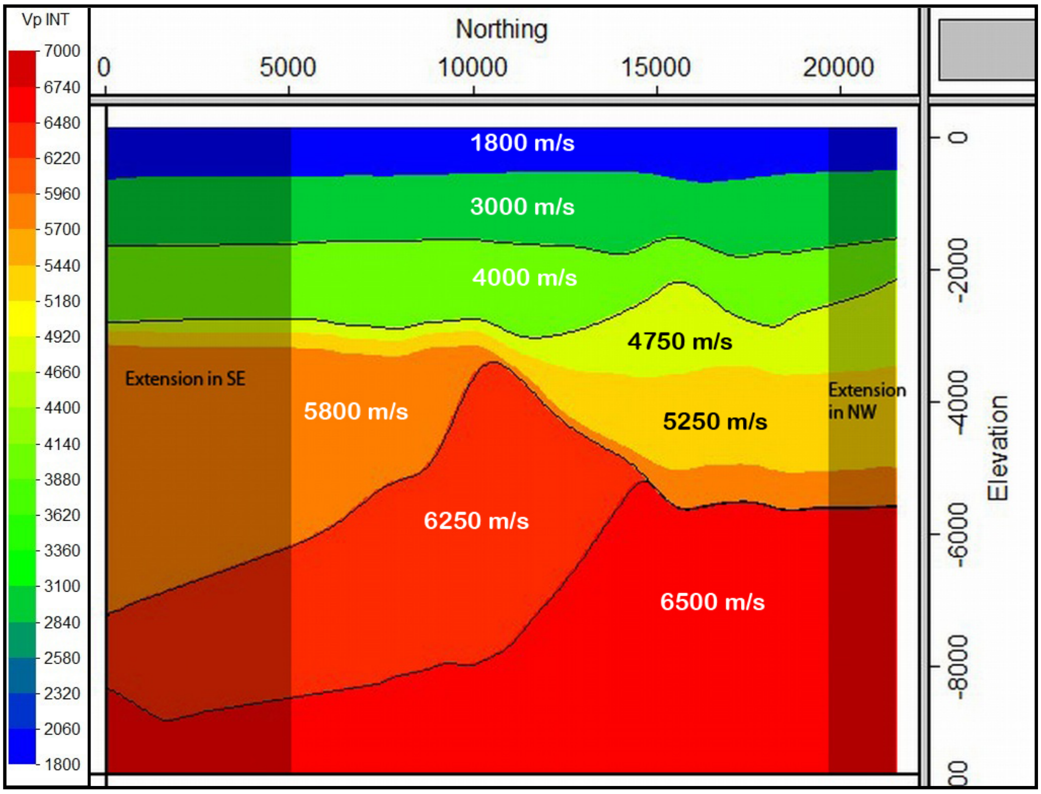

Figure 7-4: *Simplified 3d ray model* without clipping (slice from SE to NW). The black lined horizons (Horizon 0 to 3) are used in *target analysis* and in *illumination analysis*. For illumination test purposes the investigation area is extended: 5 km on the left side (SE) and 2 km on the right (NW).

7.3 SURVEY LAYOUT AND FIRST RESULTS

In this chapter the survey layout after the parameters from chapter 6 is presented and the first illumination results with the *standard option* (see chapter 7.1, method 3) on Horizon 0 to 3 are discussed.

For the survey layout a source and receiver interval of 50 m (bin size = 25 m) and a line interval SLI = RLI = 1000 m is chosen (see chapter 6.7). Overall, this survey has 6096 shots and 6020 receiver stations on 285 km² (see Figure 7-5). As mentioned above, at first the survey will be simulated with an all-live pattern, where all 6020 receivers are active at every shot. This yields in 36,7 million shot-receiver pairs and as much rays to calculate in the illumination analysis.

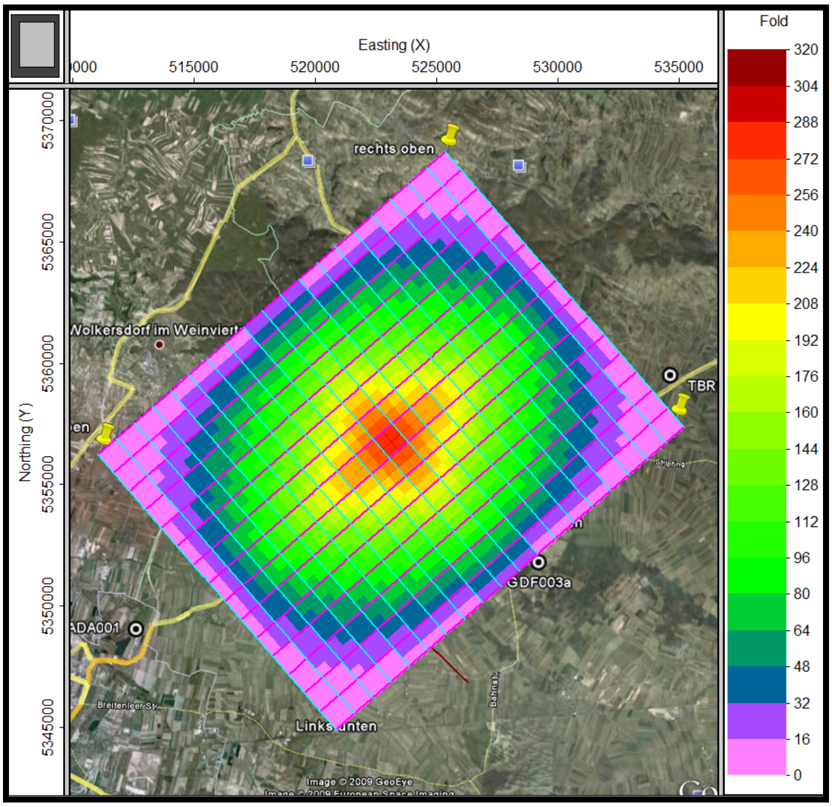

Figure 7-5: Survey layout for illumination analysis. Receiver lines in blue in dip direction and source line in red. RI = SI = 50 m and RLI = SLI = 1000 m. With the all-live pattern the highest fold is 320 in the middle. The pink area can be interpreted as *fold taper*, when the *nominal fold* is set to 16.

The shallow horizons in the *Neogene Basin fill* (Horizon 0 and 1) are not illustrated yet, but the whole area of the shallow horizons is covered well with reflection points, so the ray tracing algorithm seems to work correctly. But the results for the deeper horizons in the *Northern Calcareous Alps* are not satisfying. Figure 7-6 shows the illumination on the deep lying horizons, Horizon 2 and 3.

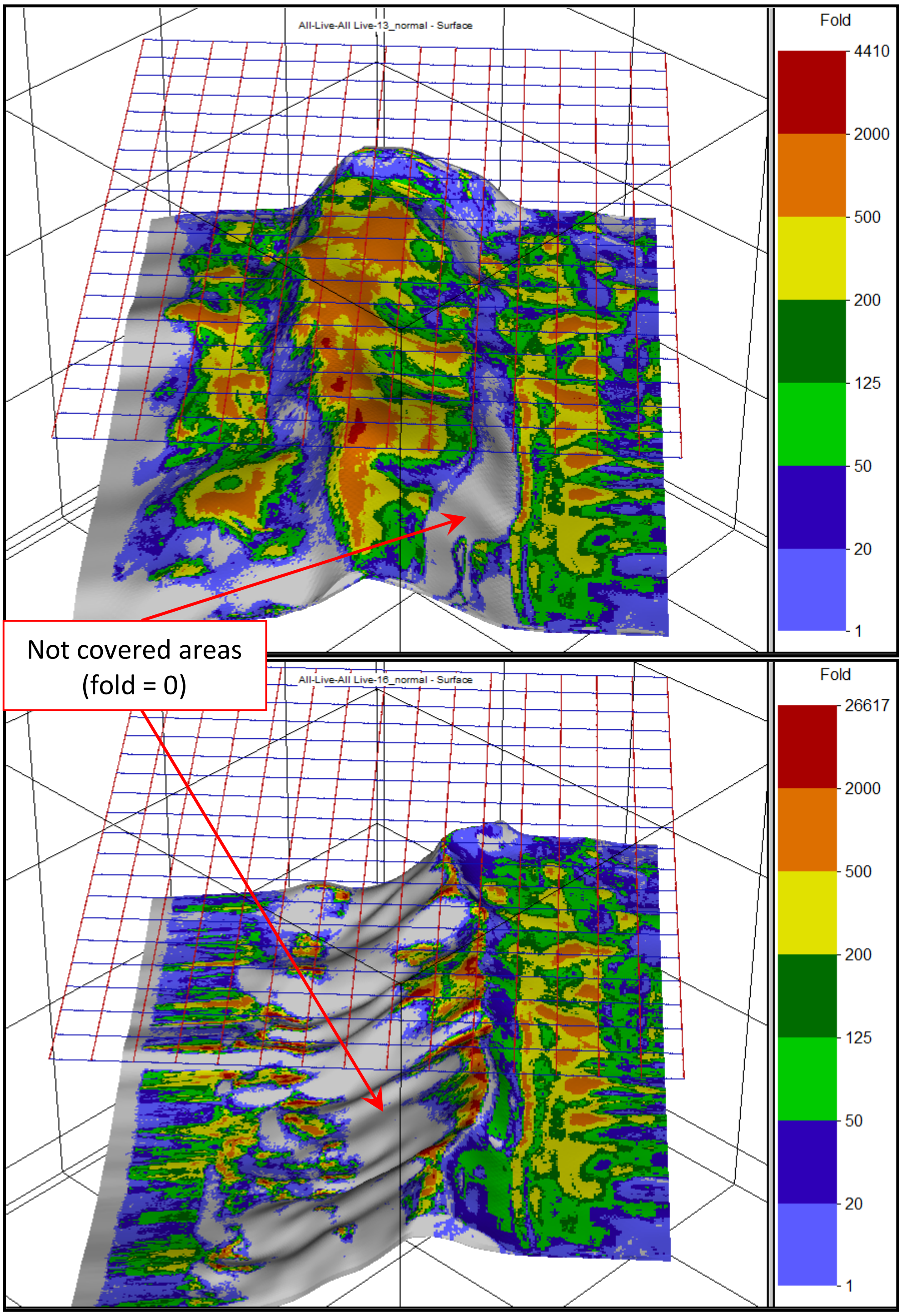

Figure 7-6: Illumination applied on the simplified *3d ray model* on Horizon 2 in the upper screenshot and Horizon 3 in the lower screenshot. The flank of Horizon 3 is not illuminated at all.

At Horizon 2 the flanks are illuminated poor but probably good enough to be imaged. It appears curious, that the area in the front right part in Figure 7-6 is not covered, although the dips are not really steep.

The flank at Horizon 3 is not covered at all in the lower part. It seems, that the rays solely concentrate on the top of the layer. Maybe the rays with the shortest travel time are all hitting the top or maybe there are some traces missing.

Figure 7-7 shows a 2D analysis. The flank of Horizon 3 is illuminated well on different shot positions. The highlighted ray indicates that there are near-zero offset rays, which hit the flank. Also the 2D line, measured in 2007 by OMV, confirms that this flank should be illuminated.

Figure 7-8 gives an example of two zero offset rays for the same source-receiver pair. Many ray tracing algorithms are only calculating the one ray with the fastest travel time, hence the ray, which is hitting the flank of Horizon 3, will not count for illumination, because its travel time is longer.

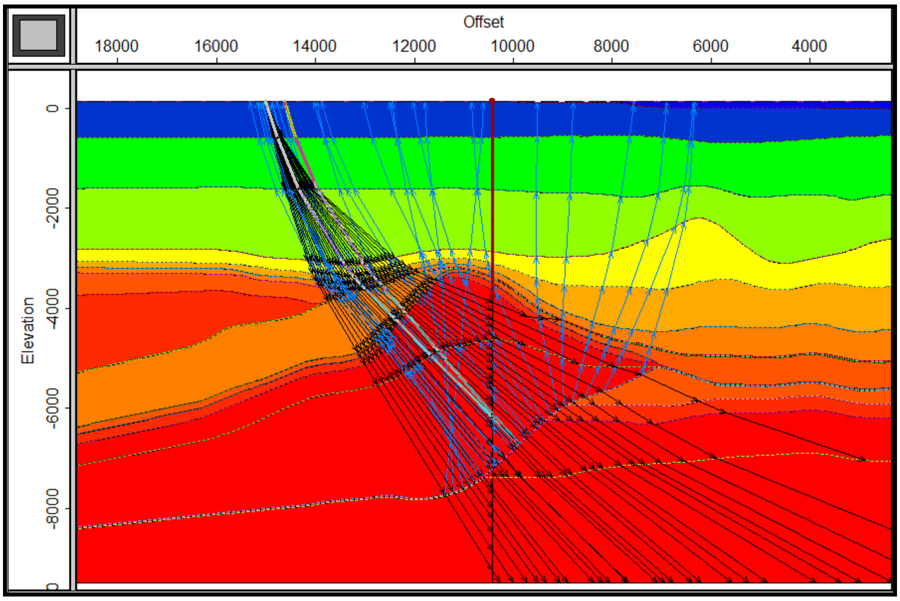

Figure 7-7: 2D slice from northeast: Shot position at offset 15 km. The reflecting horizon is Horizon 3 (BaseNCA). Source Rays are displayed in black, reflected rays in blue. 30 Ray are plotted between the emergence angle of -10° and -25°. The flank of this horizon is illuminated well.

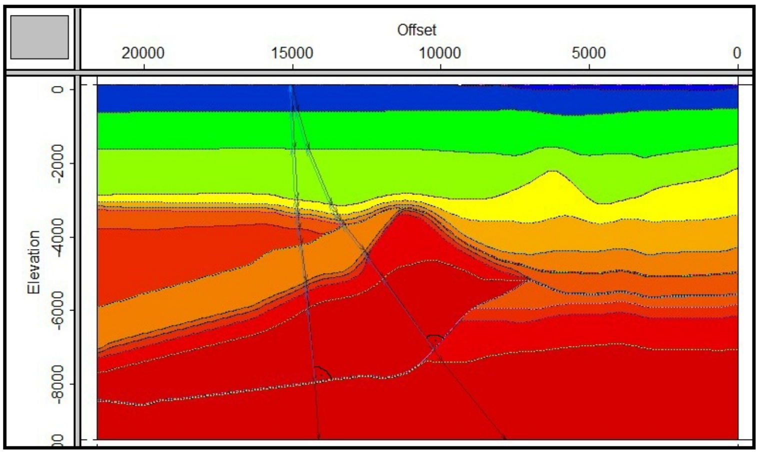

Figure 7-8: Two rays of the same shot-receiver pair. The reflecting layer is Horizon 3. The travel time of the left ray is about 3.7 seconds, the right one about 4 seconds from the source to the receiver. If the ray tracing algorithm only uses the ray with the fastest travel time, some rays (e.g. the right one which hits the flank) will not count for illumination analysis.

These first illumination results, especially those of Horizon 3, are not satisfying and therefore this study will focus on the working methods of the different ray tracing algorithms, before deciding which approach is applied for the illumination analysis to optimize the survey layout.

7.4 COMPARISON OF OMNI'S RAY TRACING ALGORITHM

To find out whether the flank of Horizon 3 really cannot be imaged or if the ray tracing algorithm is defective the different illumination methods are compared on a simple survey layout (see Figure 7-9). The test survey consist of two receiver lines with 15 receiver stations per line, where RI = 1000 m, and RLI = 2000 m. The shots are located on one source line with five shot stations (SI = 3000 m), which are lying between the two receiver lines. This layout yields to only 150 rays (shot-receiver pairs) to calculate, so that the calculation is very fast.

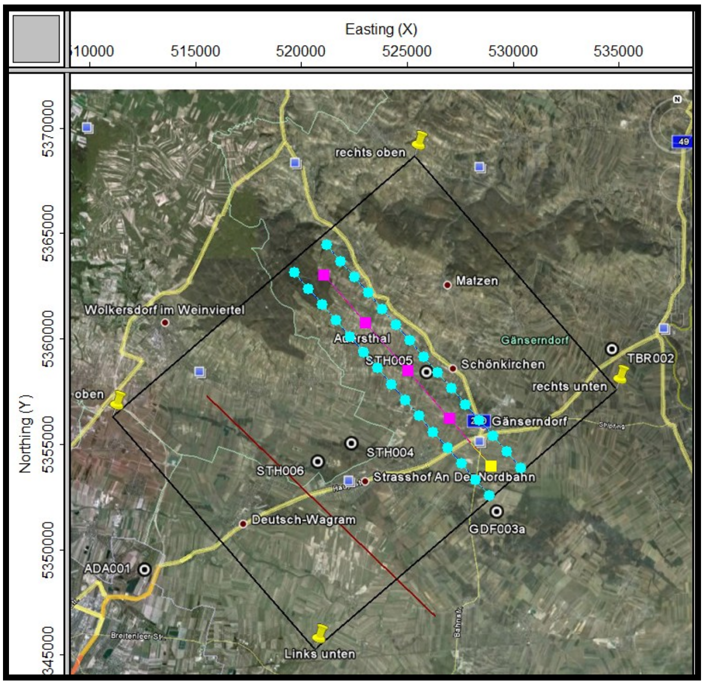

Figure 7-9: Simple test survey for ray tracing algorithm tests. receivers in blue; sources in pink

The following tests are applied on the *simplified 3d ray model* (see Figure 7-4).

Figure 7-10 to Figure 7-15 shows the illumination on Horizon 3 with different ray tracing settings. The rays of one shot (shot 2) are plotted. Please note, that the rays are calculated curved but drawn straight, due the algorithm saves only the reflection point and not the exact travel path. Thus the drawn ray marks only the affiliation of the reflection point to its source and receiver.

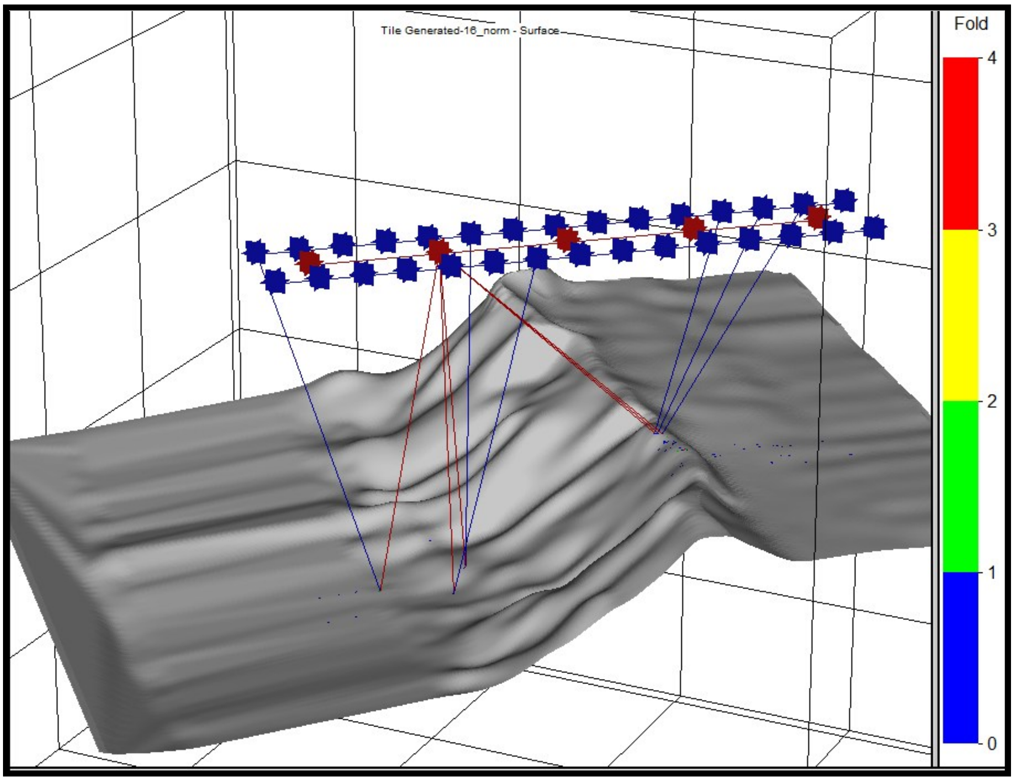

Figure 7-10: Illumination on a 3d ray model with the *standard* ray tracing algorithm. The rays of shot 2 are drawn. Calculation time: < 1 s

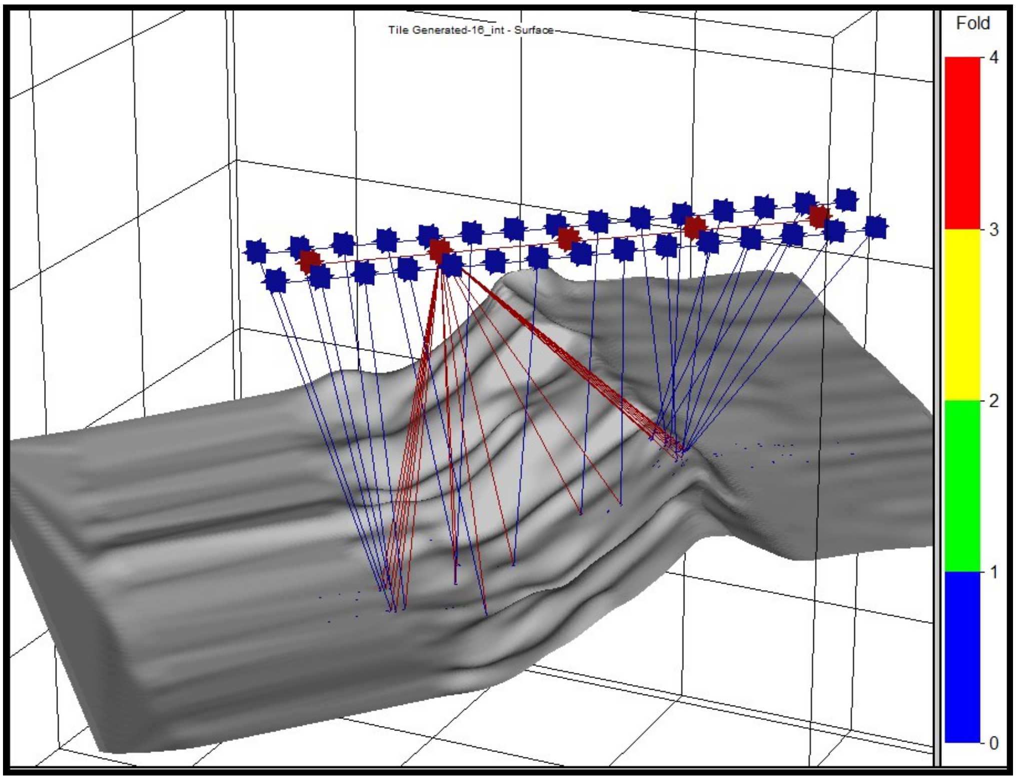

Figure 7-11: Illumination on a *3d ray model* with the option *intensive search*. The rays of shot 2 are drawn. Calculation time: ~15 s

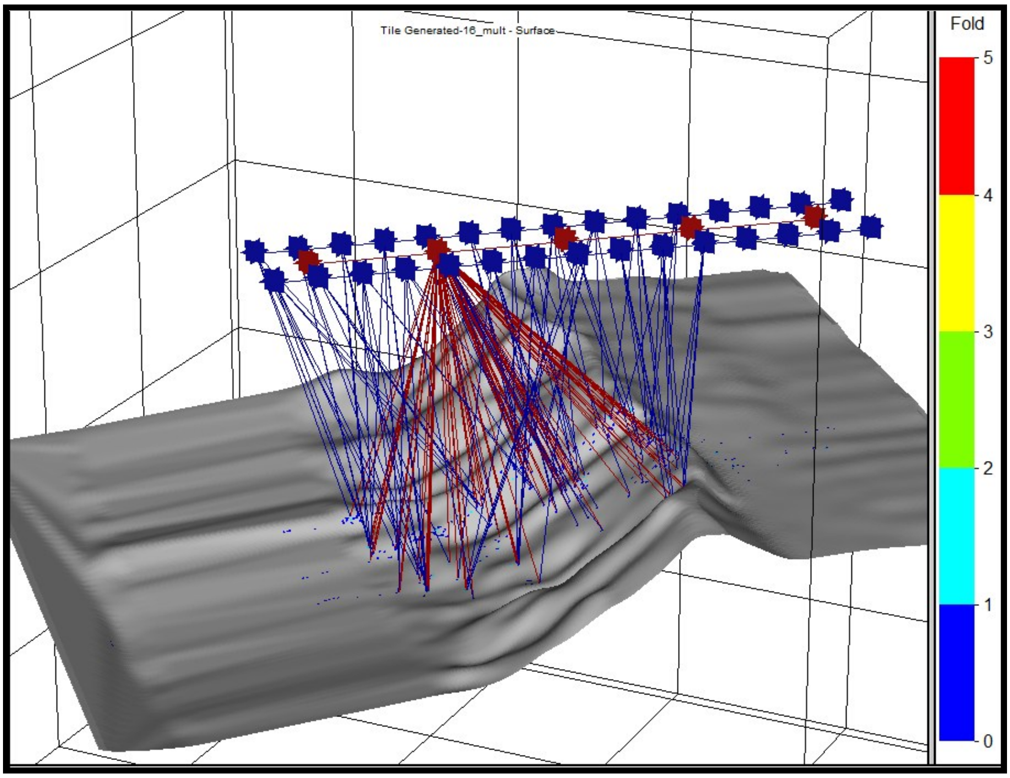

Figure 7-12: Illumination on a *3d ray model* with the option *multiple rays per trace*. The rays of shot 2 are drawn. Calculation time: 3h 33 min

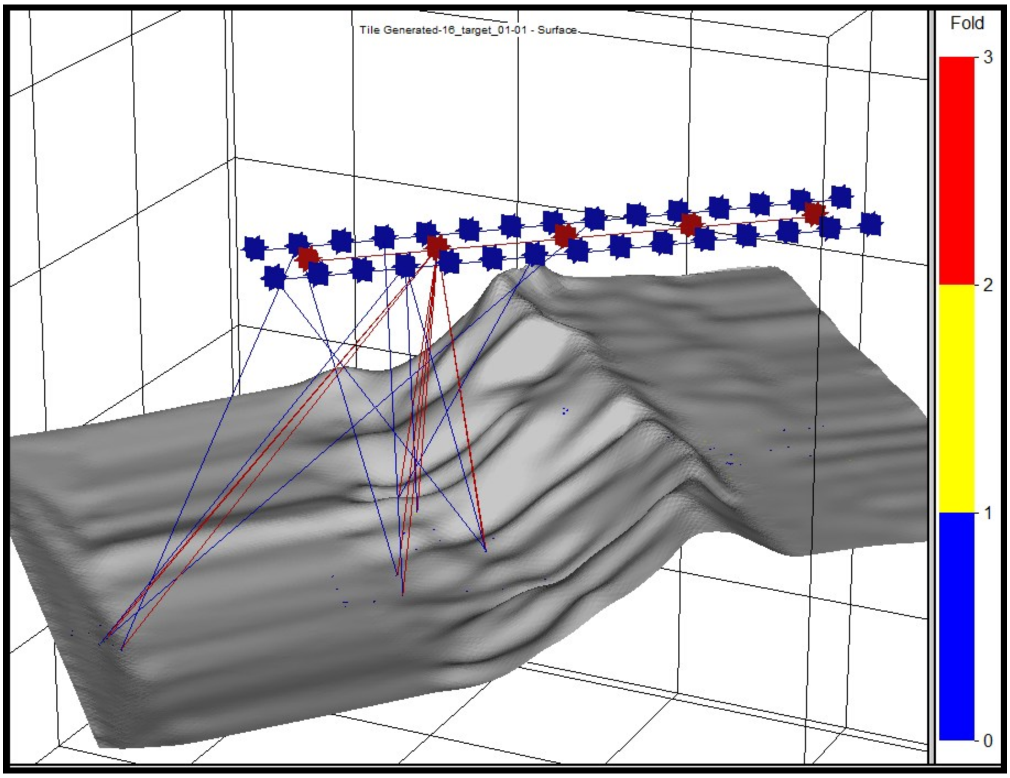

Figure 7-13: Illumination on a *target model* (curved ray). The rays of shot 2 are drawn.; max. Iterations: 1, Iteration Accuracy: 1. Calculation time: 20min

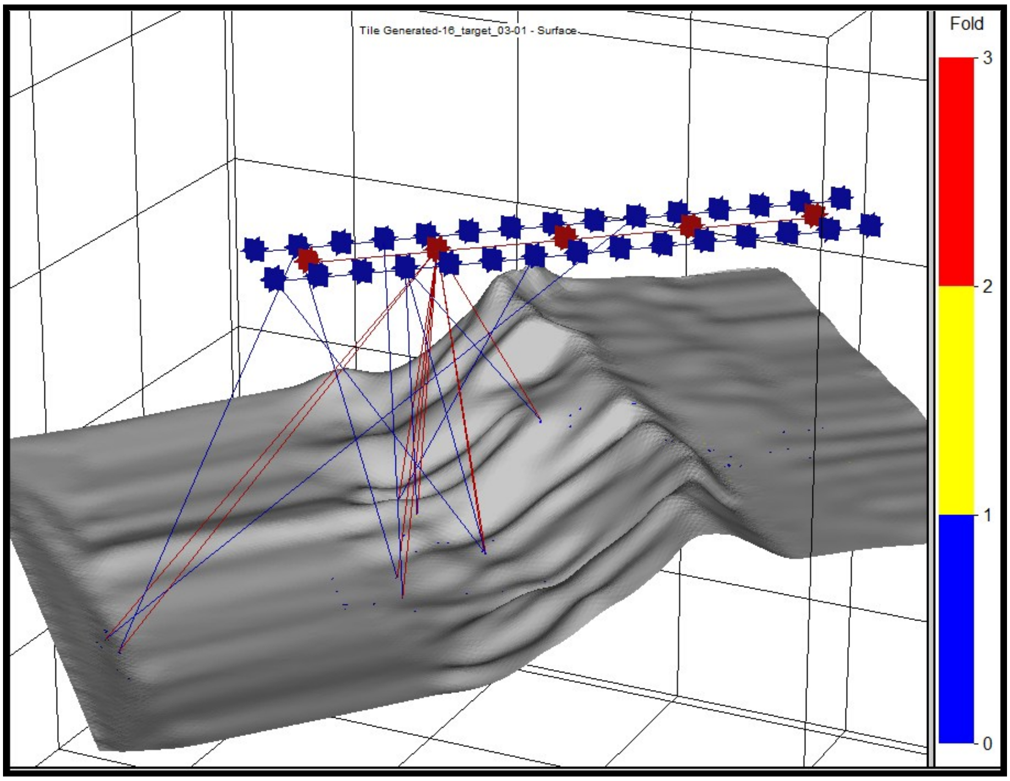

Figure 7-14: Illumination on *target model* with the option *curved ray*. The rays of shot 2 are drawn; max. Iterations: 3, iteration accuracy: 1, calculation time: 50 min

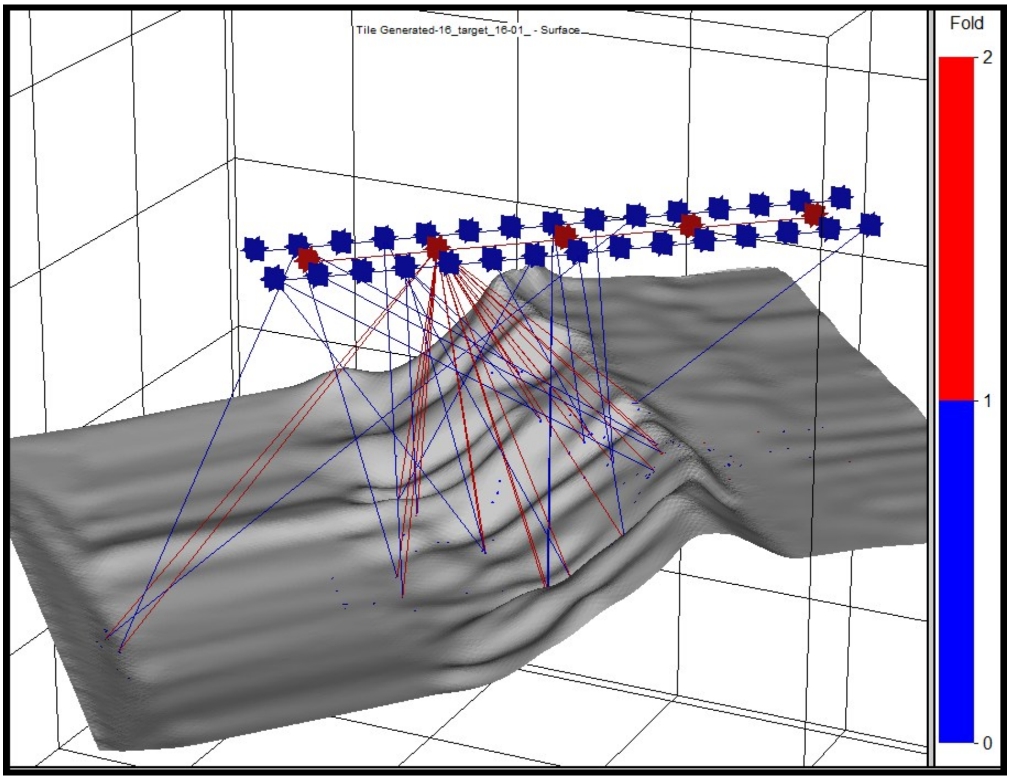

Figure 7-15: Illumination on a *target model* with the option *curved ray*. The rays of shot 2 are drawn; max. Iterations: 16, Iteration accuracy: 1 (0.5 or 3), calculation time: ~ 3h

The screenshots demonstrate, that the *standard algorithm* has troubles with the illumination of the flank and many source-receiver rays are missing. With the option *intensive search* one ray is found for nearly every shot-receiver pair. It seems, that it is the fastest ray path, like in many other ray tracing algorithms, e.g. in Vidale's algorithm (VIDALE, 1990). With the option *multiple rays per trace* up to 10 ray paths per shot-receiver pair are detected. It delivers definitely the best result, but the calculation time is much too long. It is also noticeable, that the rays with a higher offset are not calculated in Figure 7-12. It seems, that the *multiple ray* option limits the maximum offset to save calculation time.

Applying the illumination analysis on a *target model* with the option *curved ray* (option 2a in chapter 7.1) has the benefit, that the original velocity model is used. It is not clear, which criteria for the ray calculation are used, but it is definitely not the fastest ray path. Also many source-receiver rays are missing, when the *maximal iteration* is set low. More iterations yields to a more realistic result, but then the calculation time is inefficient for big surveys.

7.5 BENCHMARK OF RAY TRACING

The tests in the previous chapter mark the *intensive search* algorithm as the most efficient algorithm with a good compromise between accuracy and calculation time. In this chapter a benchmark test will show, if the algorithm is comparable with a successfully applied (e.g. BEHM et al., 2007) and well documented ray tracing algorithm. As a benchmark the algorithm from the software *HOLE* (see chapter 5.5) is used, which is stable even in high velocity contrasts and delivers the fastest ray path (HOLE et al., 1995). Again the simplified velocity model (see Figure 7-4) is used to illuminate Horizon 0, 1, 2 and 3.

The three compared algorithms are:

A) HOLE algorithm

B) OMNI *standard* algorithm

C) OMNI *intensive search* algorithm

Figure 7-16 to Figure 7-19 show the results of the benchmark test. Horizon 0 and Horizon 1 are well illuminated with all three algorithms, where **B** and **C** are very similar. The wider distribution of the reflection points on **A** is noticeable, thus the lower fold is due to the wide spaced receiver lines and will be compensated in a real survey. On Horizon 1 local synclinal structures are not illuminated, due first arrival times always hits the top of the reflector in a local surrounding.

For Horizon 2 all three illumination results deliver the same trend, where again **A** has a broader reflection point distribution in crossline direction and all rays follow the law of the minimum travel time. Therefore many reflection points are on local anti-synclinal structures of the reflector and thus no reflection point will be found in synclinals. **B** seems to show poorer performance in illuminating dips and **C** delivers definitely the best result by illuminating also the flank, although with poor fold.

The results on Horizon 3 are similar to Horizon 2. The best algorithm seems to be **C** followed by **A** and **B**.

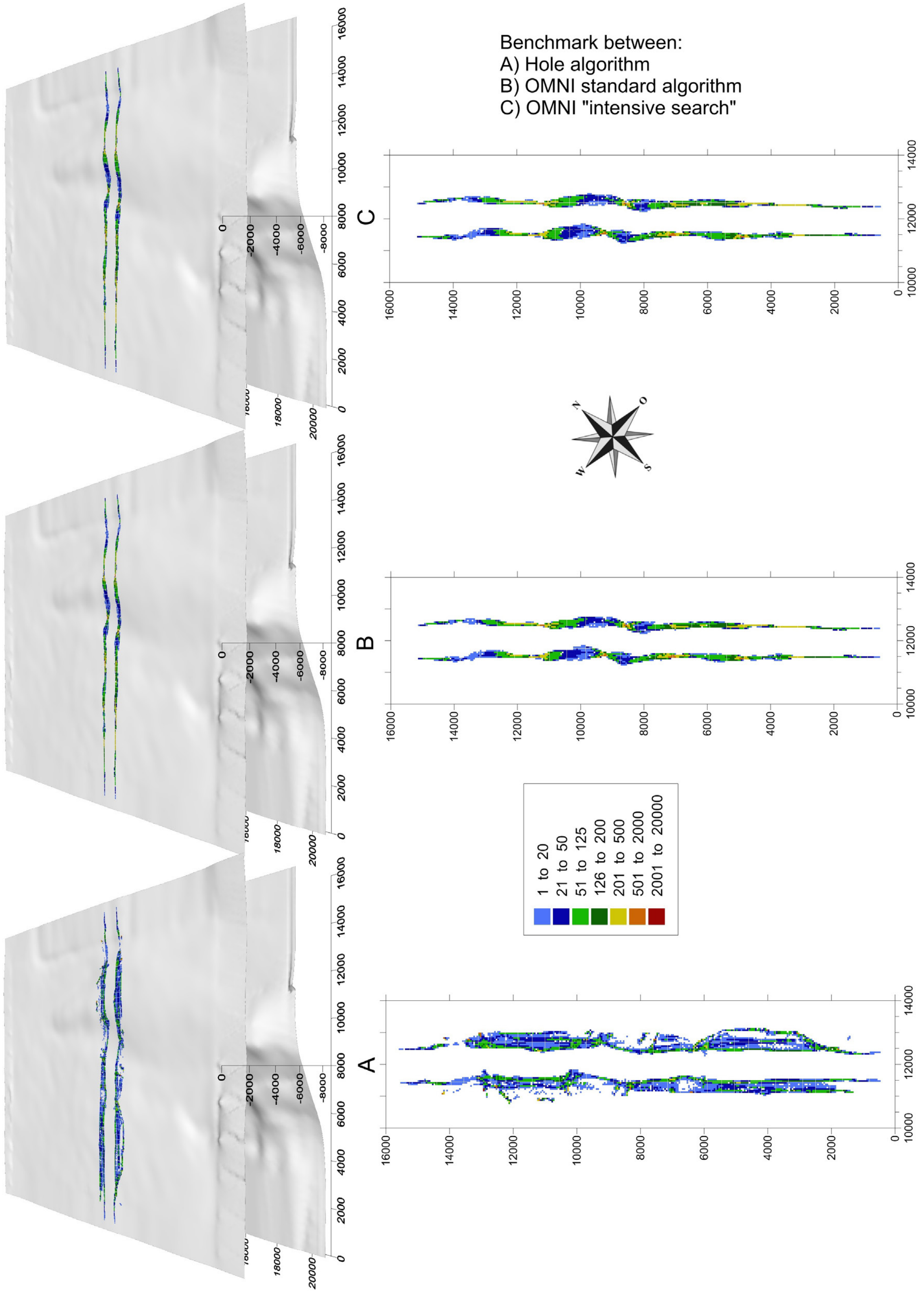

Figure 7-16: Benchmark test between the Hole- and OMNI- algorithm on Horizon 0.

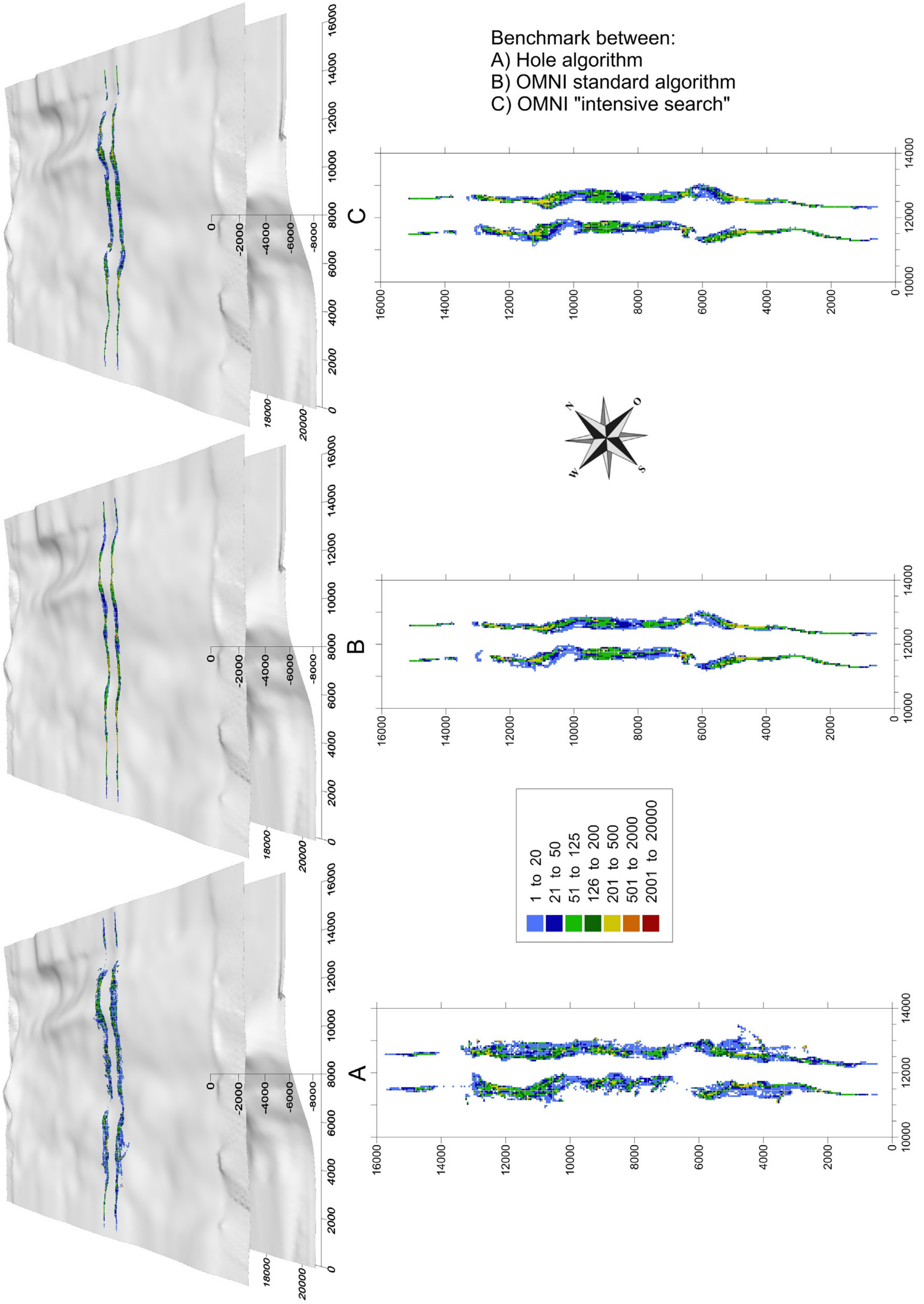

Figure 7-17: Benchmark test between the Hole- and OMNI- algorithm on Horizon 1.

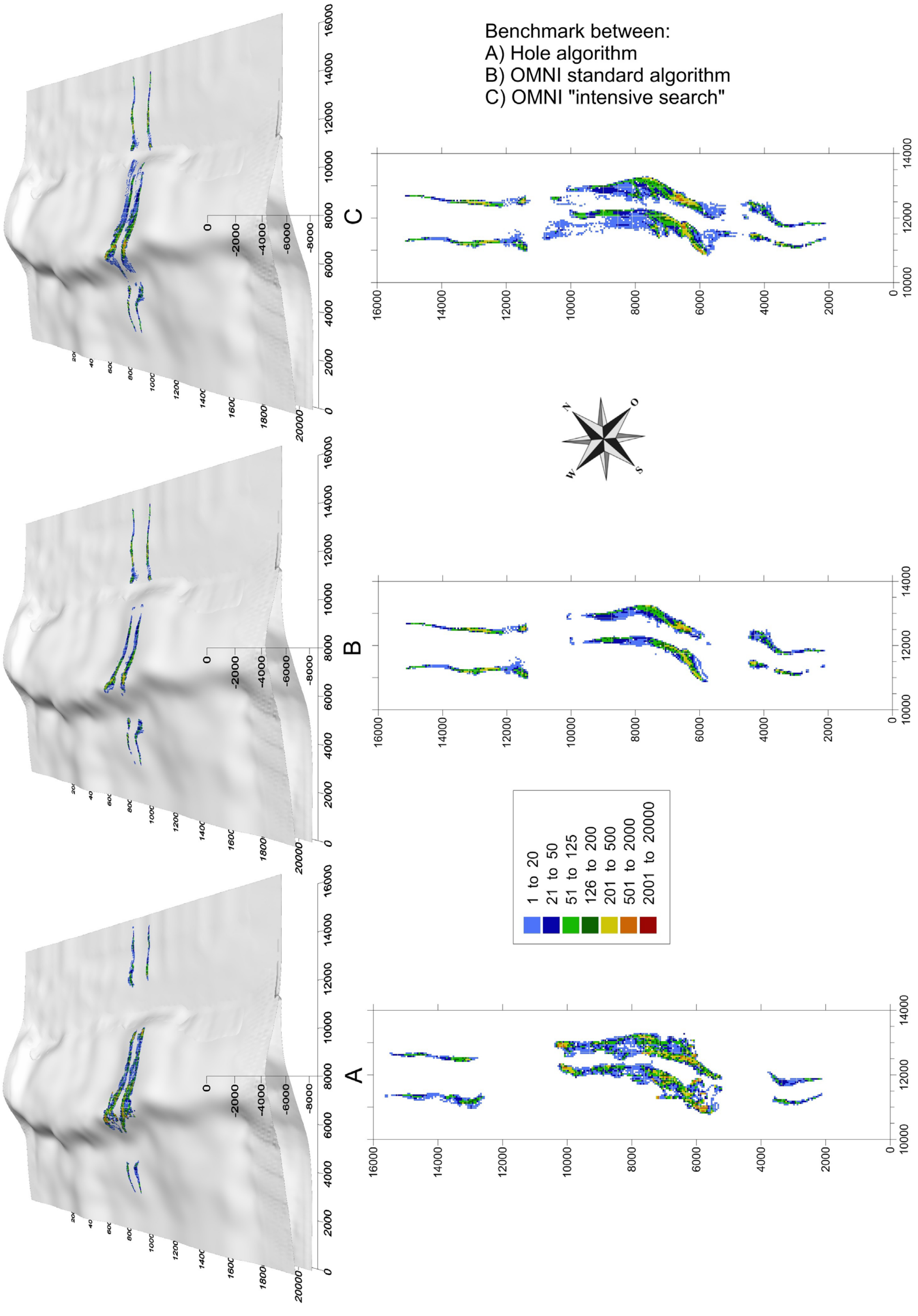

Figure 7-18: Benchmark test between the Hole- and OMNI- algorithm on Horizon 2.

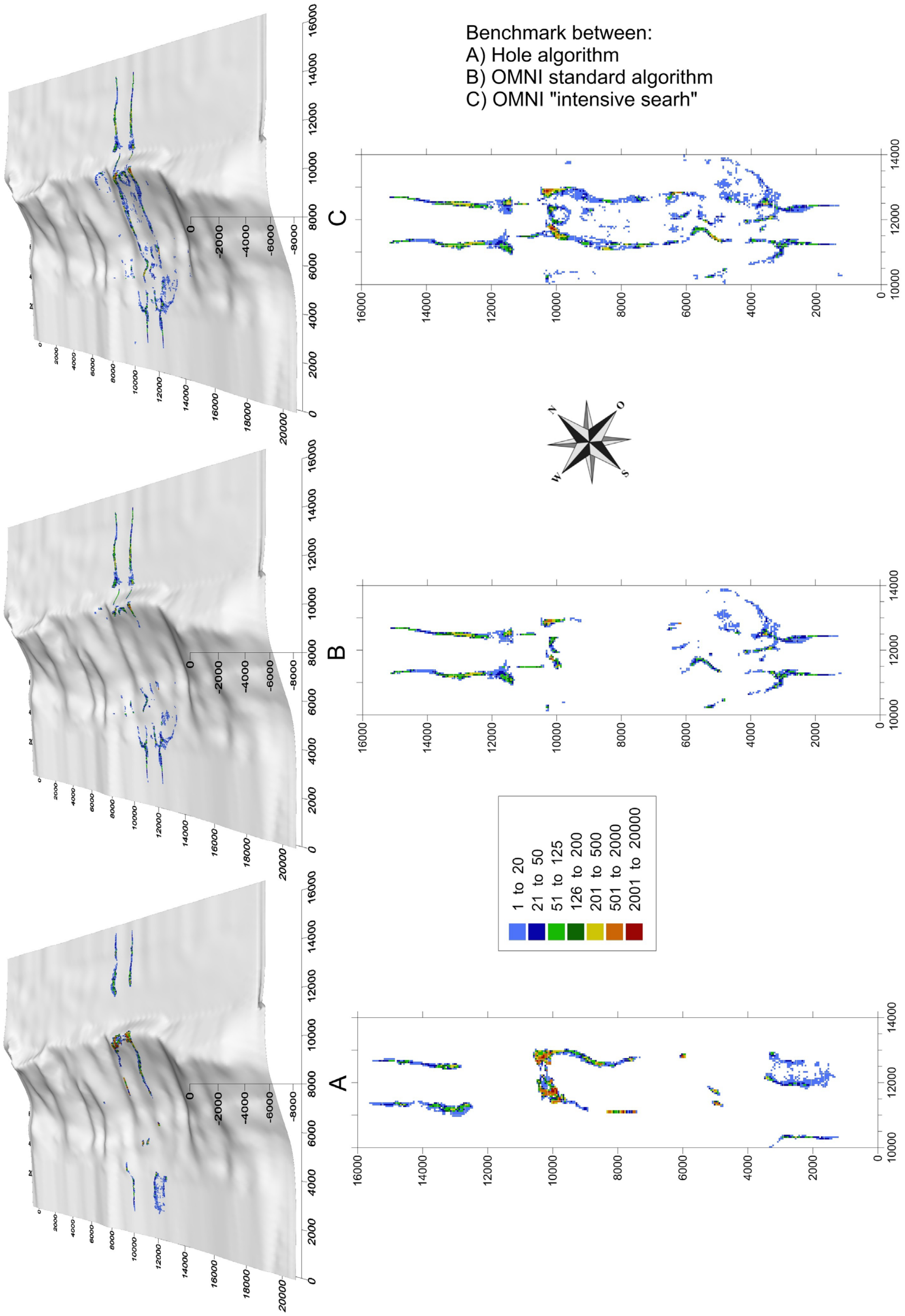

Benchmark between:
A) Hole algorithm
B) OMNI standard algorithm
C) OMNI "intensive searh"

Figure 7-19: Benchmark test between the Hole- and OMNI- algorithm on Horizon 3.

Summary of the benchmark:

All three tested algorithms have the limitation, that only one ray per source-receiver pair is calculated, which is contrary to reality. Every algorithm seems to use the fastest travel path. If one considers *multiple rays per source-receiver pair*, the calculation time increase significantly.

A) HOLE delivers realistic illumination results, where the rays concentrates strongly on the locally elevations of the reflector, which verifies the shortest travel time. Synclinal structures of the horizon are therefore not illuminated.

B) "*The standard algorithm should not lead to significant differences in reflection point density compared to the intensive search algorithm*."[17] This can be confirmed on almost flat and shallow layers. On deep layers the *standard* algorithm seems to have difficulties in illuminating horizons with moderate or steeper dips. Here many source-receiver ray-calculations fail and rays are missing. The calculation time is comparatively fast.

C) It seems, that the *standard* and *intensive search* option uses the same algorithm, but if the standard algorithm fails, the intensive search option takes the time to find the ray path. This conclusion can be made, because on Horizon 0 and 1 the results of **B** and **C** are similar and also the calculation time of the both algorithms are similar. On Horizon 2 and 3, the *intensive search* option can even take 100 times longer.

The results of **C** has the same trend as in **A**, hence the illumination results with this algorithm can be used, if one keeps in the head, that only the one ray with the fastest travel time is calculated.

---

[17] HUNT, J.; 2010: Email from support@gedco.com from 27th January

7.6 FINAL OPTIONS FOR THE ILLUMINATION ANALYSIS

The calculation time of the illumination analysis is dependent on the survey size (number of source-receiver pairs), the used ray tracing method and the subsurface resolution of the velocity model. Also computer power should be high.

In the previous chapter *the intensive search* algorithm delivers affordable results. By applying the algorithm to a velocity model (*3d ray model*) with a resolution of 200 m x 200 m x 200 m, even big surveys can be calculated in an adequate time.

Conclusions of the ray tracing tests:

- Generally method 3 of chapter 7.1 (illumination on a *3d ray model*) delivers the best results in ray tracing. If the illumination analysis is applied on a *target model,* the results are not adequate and the algorithm cannot be quantified.
- The *intensive search* option should be activated, especially on layers with dips. If the *standard* option works effectively, the calculation time of *intensive search* is not significantly longer, but if the standard algorithm fails, the *intensive search* algorithm can increase the required time appreciable - in this case by a factor of 160 on Horizon 3.
- The option *multiple rays per trace* is very interesting, but also very time consuming and only affordable for very small surveys. Also the maximum offset is limited automatically. The calculation takes about 1 to 2 minutes per source-receiver pair.[18]
- The larger the survey area, the larger the grid resolution of the velocity model has to be, so that the calculation time will be affordable. In this example for a subsurface model with a dimension of 15 km x 20 km x 10 km a resolution of 50 m x 50 m x 50 m will result in 24,000,000 knots, whereby the ray tracing algorithm has to deal with. Using a 200 m x 200 m x 200 m grid would result in

---

[18] with Intel Core 2 Quad CPU Q9400 @ 2.67GHz, 4GB DDR2 RAM, 64 bit operating system

only 370,000 knots, i.e. 64 times less grid cells and hence fastening the computations significantly.

7.7 ILLUMINATION RESULTS

Now the most efficient ray tracing method can be applied in an affordable calculation time, using the option *intensive search* and a velocity model with a grid spacing of 200 m. Every horizon is illuminated with an all-live survey and with the layout, which is illustrated in Figure 7-5. The result of the illumination can be offset limited afterwards and furthermore every arbitrary pattern configuration can be simulated without recalculate the illumination. The illumination of the field-tested configuration (*Neogene Basin Survey*) is compared with the all-live survey of the *Deep Basin Survey* and its different offset limitations to find the required maximum offset.

Two different surveys are used:

<u>- *Neogene Basin Survey:*</u> This configuration was used 25 years ago to image the *Neogene Basin fill* (first floor of the Vienna Basin). A sampling interval of $RI = SI = 50\,m$ and a line interval of $RLI = SLI = 300\,m$ was used. The pattern was dimensioned with 8 x 60 (8 receiver lines with 60 receivers) and thus a dimension of 2950 m x 2100 m. Hence, the maximum offset is 1525 m in inline direction and 1625 m in crossline direction.

<u>- *Deep Basin Survey:*</u> This design is based on the parameters determined in chapter 6 for imaging the deep Vienna Basin beneath the *Neogene Basin Floor*. The sampling interval was chosen to $RI = SI = 50\,m$ with a line interval of $RLI = SLI = 1000\,m$. The survey layout is illustrated in Figure 7-5.

Horizon 2 is the most interesting layer of the deep Vienna Basin, because its location is in the middle of the investigation area. The illumination results with different pattern configurations are demonstrated in Figure 7-20. The color code of the fold is nonlinear and with a factor 7 higher in A as in B, C and D The last level is the true maximum fold of the horizon.

A) Illumination with the *Neogene Basin Survey*. The coverage of the area with reflection points is poor. The *migrated fold* is higher than in B, because of the smaller line interval. The maximum offset is too small to allow proper migration in such depths.

B) The *Deep Basin Survey* is used and the offset is limited to 1625 m in inline and 1525 m in crossline direction. Hence it has the same maximum offsets as the 8 x 60 pattern in **A**. The reflection point coverage is the same with a 7 times higher *migrated fold* in **A** compared to **B**. This is clear, because the *Deep Basin Survey* has a larger line spacing and therefore about 7 times less source-receiver pairs in the offset area of 1625 m x 1525 m. But it verifies the usefulness of the "limited-offset-method".

C) After adjusting the offset limit successively, a limitation of 6000 m was chosen as a good compromise between reflection point density, fold and area coverage of reflection points.

D) Compared to **C** all receivers are active for every shot (all-live survey). There is no offset limitation.

The same schemes can be found in Figure 7-21 for Horizon 3, Figure 7-22 for Horizon 0 and Figure 7-23 for Horizon 1. Horizon 0 and Horizon 1 are limited with a maximum NMO stretch of 30 % in **C**. For Horizon 2 and 3 the NMO stretch is maximal 40 % without limitation.

Horizon 2:

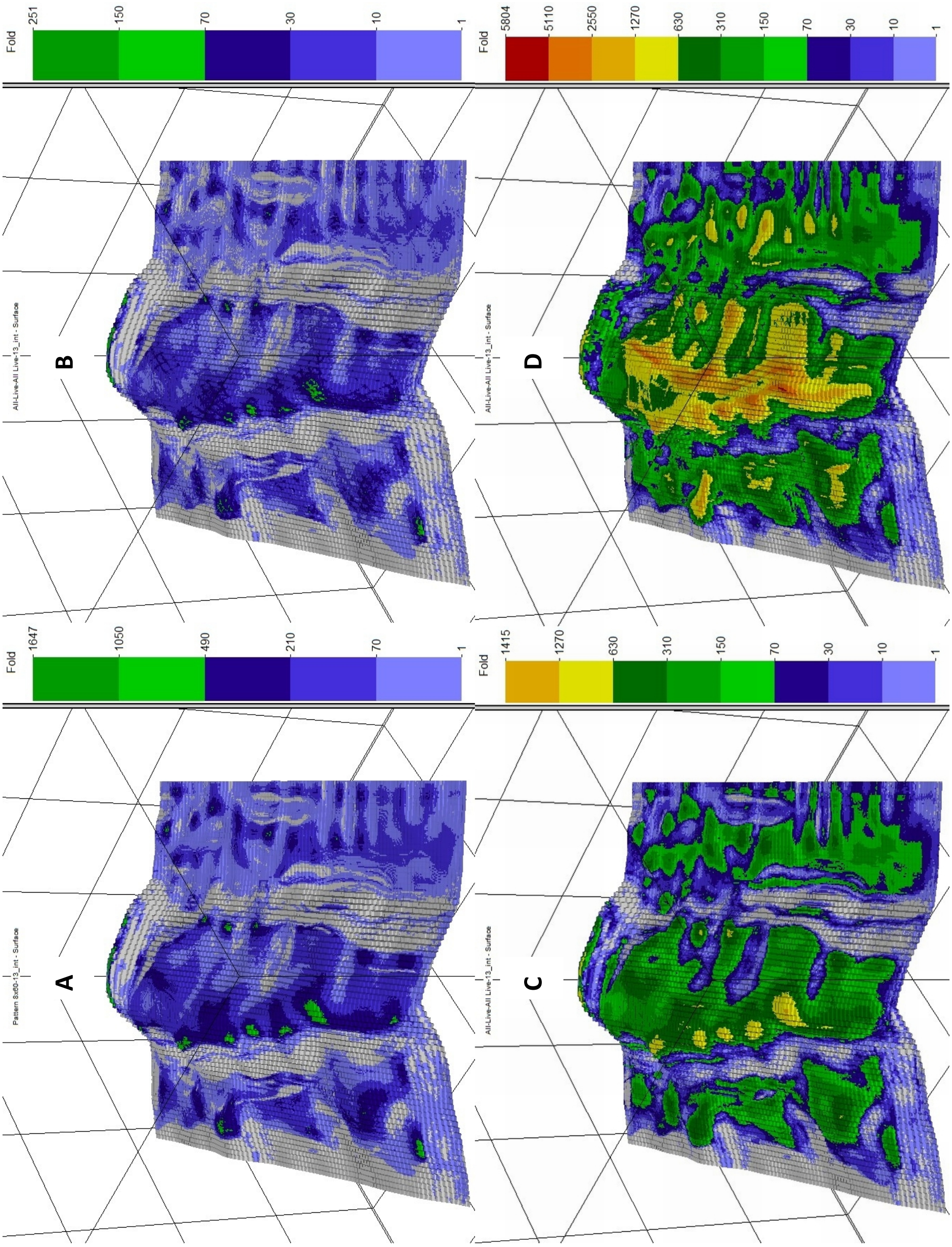

Figure 7-20: Illumination results for Horizon 2 with the *Neogene Basin Survey* in **A** (offset 1525 m inline and 1625 m crossline) and the *Deep Basin Survey* in **B**, **C** and **D**. The offset limitation is 1625 m in inline and 1525 m in crossline direction in **B**, 6000 m inline and crossline in **C** and without limitation in **D** (all-live).

Horizon 3:

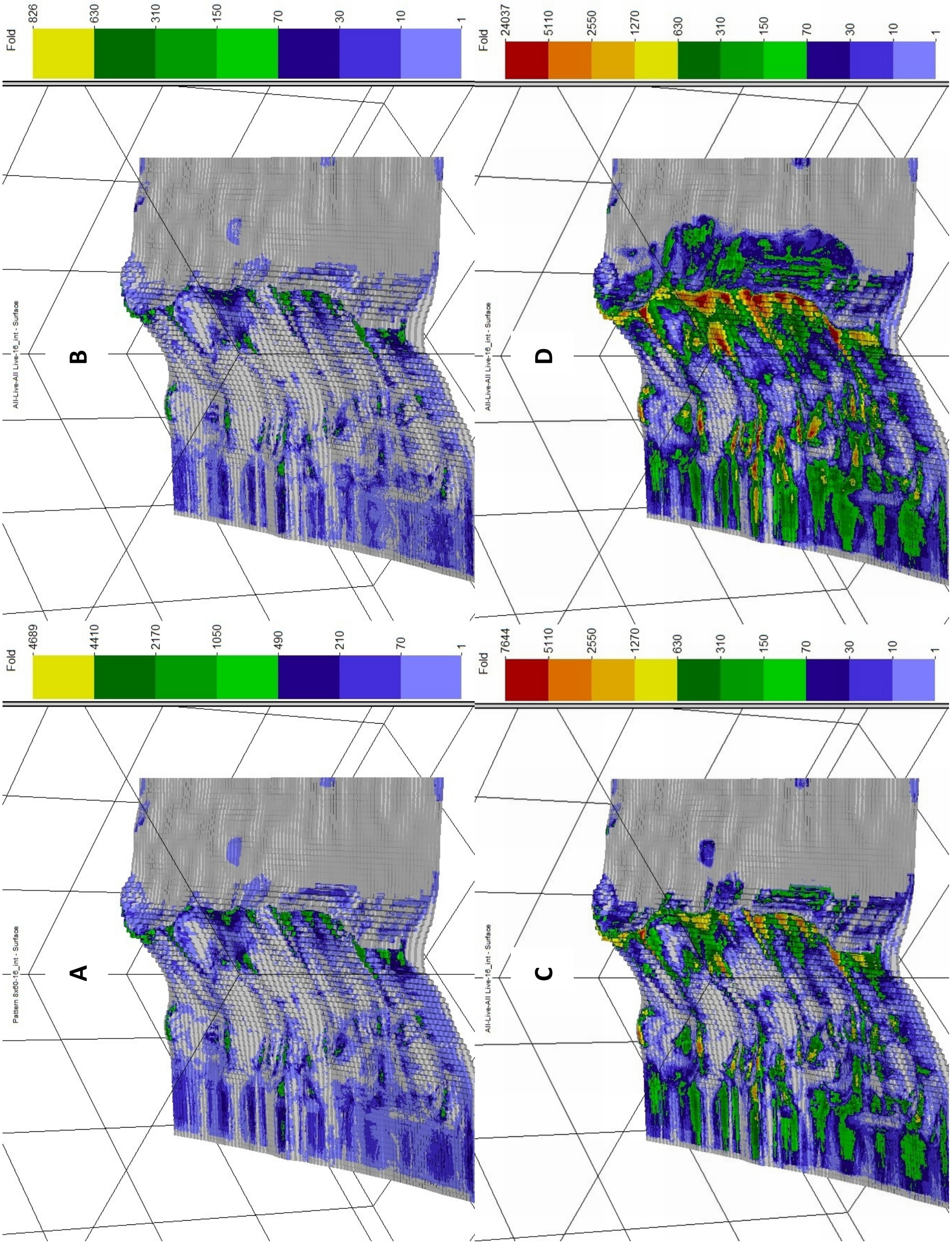

Figure 7-21: Illumination results for Horizon 3 with the *Neogene Basin Survey* in **A** (offset 1525 m inline and 1625 m crossline) and the *Deep Basin Survey* in **B**, **C** and **D**. The offset limitation is 1625 m in inline and 1525 m in crossline direction in **B**, 6000 m inline and crossline in **C** and without limitation in **D** (all-live).

Horizon 0:

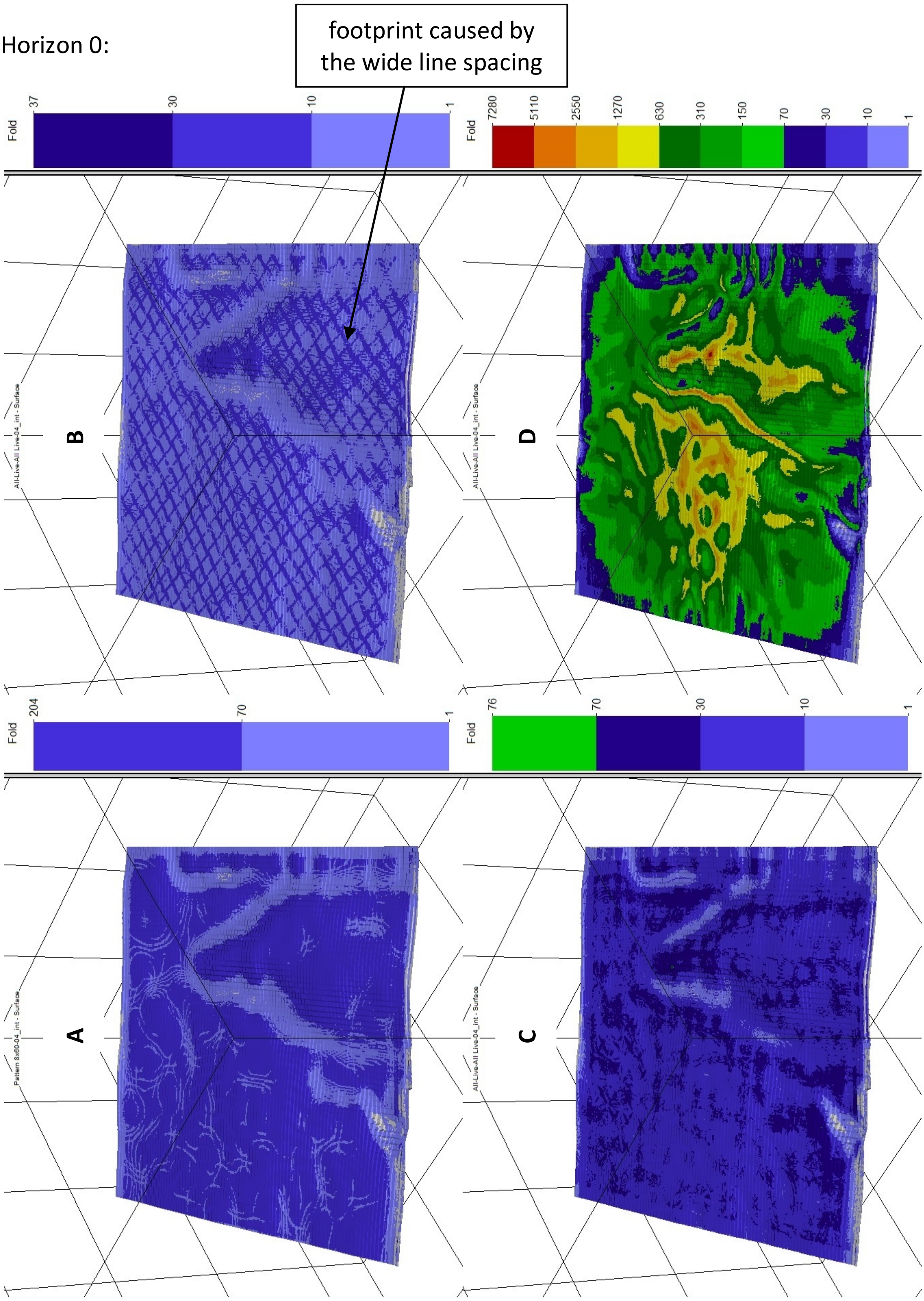

Figure 7-22: Illumination results for Horizon 0 with the *Neogene Basin Survey* in **A** (offset 1525 m inline and 1625 m crossline) and the *Deep Basin Survey* in **B**, **C** and **D**. The offset limitation is 1625 m in inline and 1525 m in crossline direction in **B**, a maximum allowed NMO stretch of 30% (equates about 2600 m inline and crossline offset) in and without a limitation in **D** (all-live).

Horizon 1:

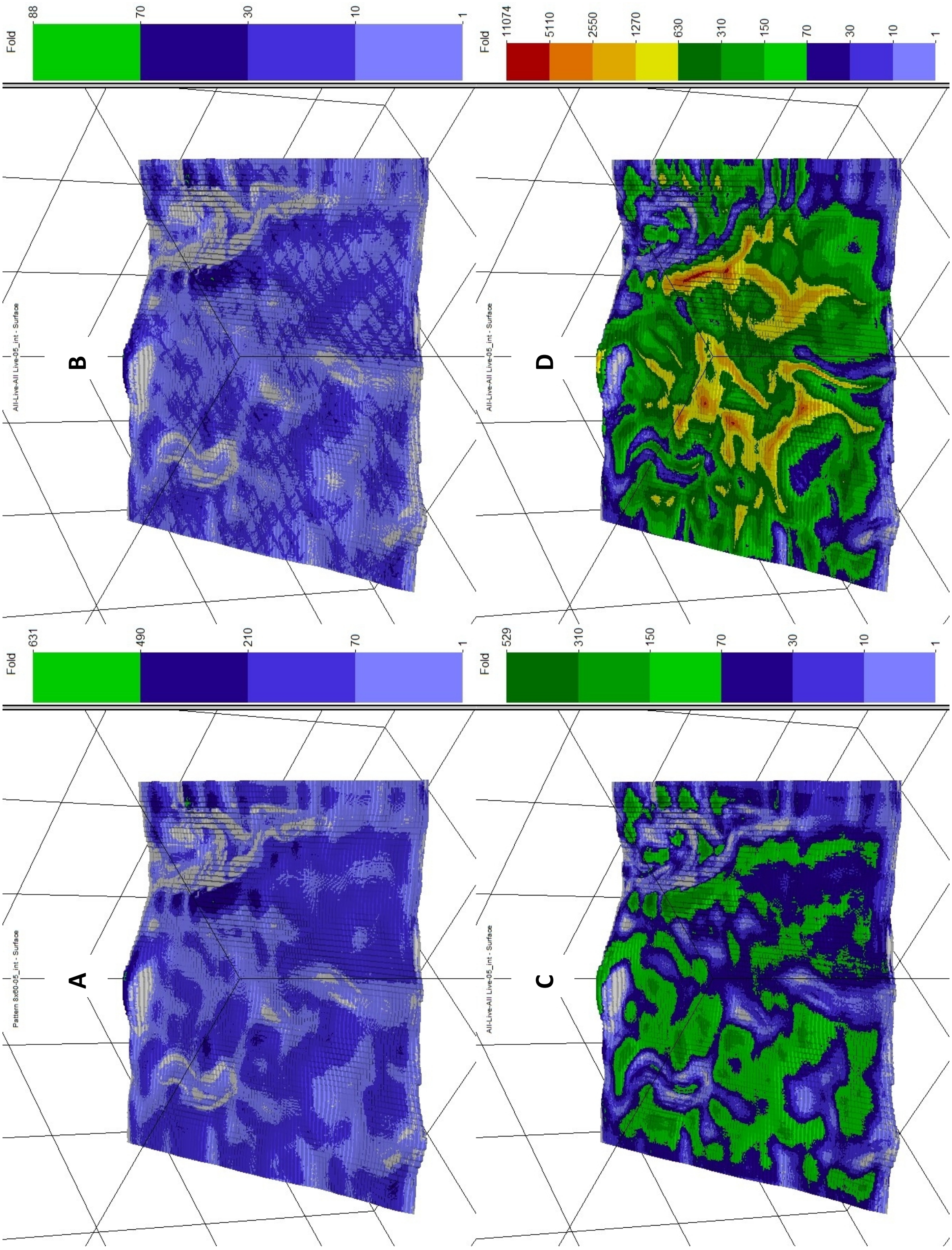

Figure 7-23: Illumination results for Horizon 1 with the *Neogene Basin Survey* in **A** (offset 1525 m inline and 1625 m crossline) and the *Deep Basin Survey* in **B**, **C** and **D**. The offset limitation is 1625 m in inline and 1525 m in crossline direction in **B**, a maximum allowed NMO stretch of 30% (equates about 4500 m inline and crossline offset) in and without a limitation in **D** (all-live).

7.8 DISCUSSION OF THE RESULTS

In comparison to the *Neogene Basin Survey*, where the *deep Vienna Basin* is not imaged at all, an improvement of the fold can be reached with an optimum acquisition design. This includes a high number of receivers, because the required offset is large. The line interval can be expanded up to 1000 m, since the *Neogene Basin fill* is not the main target. The horizon of main interest (Horizon 2) should be image-able well with a fold in the range from 70 to 300.

Most parts of the flank of Horizon 3 (*BaseNCA*) are covered with reflection points, although with low fold. Hence, parts of the flank should be interpretable in the seismic section. Furtheron it has to be considered, that only the one ray with the fastest travel time is accounted per source-receiver pair, so the coverage of reflection points on the flank of Horizon 3 will be better in reality than in the simulation (especially on synclinal structures).

Horizon 0 is located in the middle of the *Neogene Basin fill* and is already imaged with the *Neogene Basin Survey* from the 1980's. This layer is not a target in the *Deep Basin Survey* and is analyzed for comparison, because a new picture of the *Neogene Basin Fill* also interesting. The "footprint" caused by the wide line interval of 1000 m (see Figure 7-22 B) can be seen and the fold is very low (about 10). However, there will be gaps in the image but it may be interpretable by combining the image with the *Neogene Basin Survey*.

The footprint of the line spacing is also distinctive on Horizon 1 (see Figure 7-23 B) and has a weak conspicuity even on Horizon 2 (Figure 7-20 B) with a small offsets limitation. By allowing larger offsets the footprint vanishes (Figure 7-20 C and D).

Figure 7-20 C and Figure 7-21 C gives the illumination results for a pattern with a realizable offset and a realistic number of receivers. The maximum offset of 6000 m in inline and crossline direction leads to a pattern dimension of 12 km x 12 km or 12 lines with 240 receivers (pattern size = 12 x 240). Therefore 2880 active receivers will be necessary. If more receivers are available (or rather affordable) a smaller line spacing is recommended to get information in the *Neogene Basin fill* as well. The maximum offset may also be reduced in crossline direction. The *Deep Basin Survey* has the great improvement of a wider maximum offset. This leads to a much higher migration angle compared to the *Neogene Basin Survey*, which allows proper migration also in the deep sections. Furthermore steeper dips can be imaged.

For Horizon 0 and 1 (Figure 7-22 C and Figure 7-23 C) the maximum offset is limited by an NMO stretch of 30 % (see also chapter 6.3) and shows, that higher offsets are not needed for interpretation. Horizon 2 and 3 are not NMO stretch limited. The NMO-stretch on Horizon 3 with an offset limitation of 6000 m is staying under 40 % and on Horizon 2 the NMO stretch does not exceed 28 %.

The northwestern flat part of Horizon 3 is not illuminated, which is a good example of the problem caused by clipping layers (see chapter 7.2). The northwestern flat part of Horizon 2 in the same depth is illuminated, but the clipped part of Horizon 3, which is 10 m beneath Horizon 2 is poor illuminated. This case coincidentally equates reality, because it is the iso-surface through the *Flysch* with has a linear depth increasing velocity without impedance contrast (no velocity discontinuity). This non-illuminated area can be ignored.

8 CONCLUSION

Three dimensional model-based survey design may play a major role in future and is interesting, especially in areas with complex geology. Moreover, it is certainly also dependent on the resolution and the accuracy of the subsurface model. Generally, the used software (Omni) can determine the most important acquisition parameters fast and the results can be visualized on the selected horizon. A disadvantage is the poor documentation of the calculation methods and the incomplete description of the input parameters for determining the parameters. Hence, it took a lot of time to find out what the exact formulas and correct options are. The determined parameters are also affected by the constitution (e.g. maximum dip, smoothness,..) of the selected horizons. So three horizons were selected in order to range from the highest to the lowest depth of interest, and also the maximum dips, which need to be resolved, are included. As already mentioned, the software uses the root mean square velocity instead of the interval velocity to be sure, that the determined parameters are also valid for smaller interval velocities, which may be above the analyzed layer. This is not necessary, if the upper horizon is on the highest level of interest, like in this case. But since the errors of velocity model building and the fact, that most formulas are adapted from the constant velocity design, it is good to have a safety buffer. One advantage of OMNI`s *target analysis* is that the velocity model can be used directly without modification.

As a precondition for determining the bin size the maximum achievable frequency has to be known, which generally decreases with depth. In this case, the frequencies could be evaluated from real data by extraction from an existing seismic 2D line in the investigation area. Therefore the bin size can be calculated for the selected horizon before and after migration and it is a good guidance to decide the right bin size. The bin size is one of the most important parameters for the seismic survey and defines the maximum recordable frequency, the dimension of aliasing and the maximum incidence angle of the wave that can be recorded by the receivers. It has also an impact to the fold, the number of receivers, the maximum offset and the survey costs.

Another *target analysis*, to determine the maximum unaliased frequency, uses the converted bin size equation. It is interesting to see, which frequencies can be maximally recorded with the selected bin size in respect to the dips of the layer. The intrinsic attenuation is not included, and can be calculated separately.

The determination of the vertical and horizontal spatial resolution has an approved computation base. In the formula the angle between source and receiver is included. It is determined with the input parameter *average offset*, which is approximated by the half of the maximum offset due to a 30% NMO stretch. Hence, the input parameter has an uncertainty, which affects the result slightly. An exact error calculation is ineffective, since there are only rare hard facts.

The amplitude losses give a valuation for the amplitude decrease due to geometrical spreading and absorption. By calculating the absorption a probable bug in the software was detected, thus the average quality factor Q_{AVE} is taken as input parameter as a compromise. However, the result indicates the dimension of the amplitude attenuation.

The determination of the migration aperture is calculated for a 30° diffraction angle and takes ray bending into account. The migration apron is illustrated with a self written script to demonstrate the survey extension, if the whole velocity model area wants to be imaged. Therefore the survey has to be extended by a factor 1.7 to migrate the investigation area properly.

The illumination analysis can be applied for different survey layouts. It can be very time consuming and is strongly dependent on the used ray tracing algorithm and the subsurface grid spacing. One weakness of the used software is, that the subsurface model has to be rebuilt, where lateral variations of velocities are hard to realize and the velocity model gets more simplified. This can be justified, if one considers, that the velocity model has already been simplified several times during this study and only rough structures of the underground are known, which are mostly estimated. A detailed subsurface model can be built after measuring and interpreting the *Deep Basin Survey*.

At the beginning there were difficulties to get comparable results of the ray tracing based illumination analysis. Due to the missing references of the software a detailed testing of the algorithms, options and a benchmark test were indispensable. Finally, the optimal options are worked out to get a comparable and comprehensible illumination result.

The applied method to calculate the all-live survey once for each horizon and then limit the maximum offset successively worked fine and every arbitrary pattern size can be simulated very fast without recalculation. The coverage of reflection points can be compared and thus the required pattern size can be evaluated.

As mentioned in the introducing chapter the *deep Vienna Basin* is certainly a challenge for a seismic investigation, especially due to the deep lying steep dipped layers. The *Deep Basin Survey*, which is the final goal of this work, gives a concrete idea of a survey layout that considers the important acquisition parameters to carry out the survey successfully. Also the feasibility, the number of receivers and the budget was considered in a more or less realistic way. Finally, a spatial sampling interval of 50 m (bin size = 25 m) was chosen for the *Deep Basin Survey*, which is equal to the *Neogene Basin Survey*. The great difference is the line spacing of 1000 m compared to the *Neogene Basin Survey* with a line spacing of 300 m. Also much more receivers are available, thus a bigger pattern size (factor 21) can be realized. The higher maximum offset (factor 7.2) is required to resolve and migrate the deep lying dipped layers. Although the line spacing is wide, an improved fold (factor 1.3 on the main target) can be obtained. The pattern size is therefore 12 x 240 (131 km^2) in comparison to the *Neogene Basin Survey* with a pattern size of 8 x 60 (6.2 km^2). The number of receivers is 2880 in comparison to 480 (factor 6). A disadvantage of the wide line spacing is, that the upper 1000 m in the *Neogene Basin fill* will probably not be visible in the seismic image. The layers underneath should be interpretable, although there will be a footprint from the line spacing.

The implementation of the Deep Basin Survey will be interesting and will certainly bring new scientific findings. Especially the comparison of the theoretically considered results and the real data will be exciting.

A further wave-equation-based illumination method may be interesting in future, where a target-orientated and volumetric illumination analysis in 2D and 3D are possible (XIE et al., 2006). This method suits properly in complex media, where velocity smoothing and Fresnel-zone smoothing is not required as in the high-frequency, asymptotic, ray-based approach. The advantage of this method in comparison to ray tracing methods is the direct relation to the amplitude of the signal and full wave fronts are used instead of only one ray per shot-receiver pair. A disadvantage may be again the computation time.

9 REFERENCES

AKI, K. and RICHARDS, P.G. [2002] Quantitative Seismology - second edition. *University Science Books,* United States, CA - Sausalito, 704 pages

ALVAREZ, G., PEREYRA, V. and CARCIONE, L. [2004] Model-based 3-D seismic survey design as an optimization problem. *SEG Extended Abstracts,* **23**, 63-66

ASHTON, P.C., BACON, B., DEPLANTE, C., DICKILRESON and REDEKOP, G. [1994] 3D Seismic Survey Design. *Oilfield Review*, **6** (2), 19-32

BEHM, M., BRÜCKL, E., CHWATAL, W. and THYBO, H. [2007] Application of stacking and inversion techniques to 3D wide-angle reflection and refraction seismic data of the Eastern Alps. *Geophysical Journal International*, **170** (1), 275-298

BORN, M. and WOLF, E. [1999] Principle of Optics - Seventh expanded edition. *Cambridge University Press*, UK, 986 pages

BRITTLE, K.F., LINES, L.R. and DEY, A.K. [2001] Vibroseis deconvolution: a comparison of cross-correlation and frequency-domain sweep deconvolution. *Geophysical Prospecting,* **49** (6), 675-686

BROWN, A.R. [2004] Interpretation of Three-Dimensional Seismic Data, sixth edition. *Society of Exploration Geophysicists*, Tulsa - Oklahoma, 560 pages

COOPER, N. [2004] A world of reality—Designing land 3D programs for signal, noise, and prestack migration. *The Leading Edge*, **23** (10), part 1: 1007-1014, part 2: 1230-1235

CORDSEN, A., GALBRAITH, M. and PEIRCE, J. [2000] Planning Land 3-D Seismic Surveys. *Society of Exploration Geophysicists*, Tulsa - Oklahoma, 204 pages

EBROM, D., LI, X. and MC-DONALD, J. [1995] Bin spacing in land 3-D seismic surveys and horizontal resolution in time slices*. The Leading Edge*, **14** (1), 37-40

FOMEL, S. and STOVAS, A. [2010] Generalized nonhyperbolic moveout approximation. *Geophysics,* **75** (1), U9–U18

GALBRAITH, M. [2004] A new methodology for 3D survey design*. The Leading Edge*, **23** (10), 1017-1023

GALBRAITH, M. and WILLSON, N. [2009] Email from support@gedco.com from 28th October, including a presentation of Mike Galbraith from 2007: Bin Size: Lateral and Vertical Resolution

HAMILTON, W., WAGNER L. and WESSELY, G. [2000] Oil and Gas in Austria. In: NEUBAUER, F. and HÖCK, V.: Aspects of Geology in Austria. *Mitteilungen der Österreichischen Geologischen Gesellschaft* ÖGG, Vienna, **92**, 235-262

HOLE, J.A. and ZELT, B.C. [1995] 3-D finite-difference reflection traveltimes. *Geophysical Journal International*, **121** (2), 427–434

KALLWEIT, R.S. and WOOD, L.C. [1982] The limits of resolution of zero-phase wavelets. *Geophysics*, **47** (7), 1035-1046

KRÖLL, A. [1980] Die österreichischen Erdöl- und Erdgasprovinzen: Das Wiener Becken. In: BACHMAYER, F.: Erdöl und Erdgas in Österreich. *Naturhistorisches Museum*, Vienna

LASTER, S.J. [1985] The present state of seismic data acquisition - One view. *Geophysics*, **50 (**12), 2443-2451.

LINER, C.L. and UNDERWOOD, W.D. [1999] 3-D seismic survey design for linear v(z) media. *Geophysics*, **64** (2), 486-493

MURTY, N. and SHANKAR, T. [2007] Pre Stack Migration Aperture - An Overview, Part II. *Geohorizons India*, **July**, 23-26

NACHTMANN, W. [2007] Exploration Country Focus: Austria. *AAPG European Region Newsletter*, **September**, 4-6

PADHI, P.T. and HOLLEY, T.K. [1997] Wide azimuths - why not? *The Leading Edge*, **16** (2), 175-177

PILLER, W.E. [1999] The Neogene of the Vienna Basin. *Berichte der Geologischen Bundesanstalt,* Band **49**, 113 p., Wien, 11-19

QUIGLEY, J. [2000] Evolution of a seismic acquisition methodology through integrated testing - onshore Abu Dhabi, United Arab Emirates, 1996-2000. *First Break*, **18** (11), 452–485

RÖGL, F. [1996] Stratigraphic correlation of the Paratethys Oligocene and Miocene; *Mitteilungen der Gesellschaft der Geologie- und Bergbaustudenten in Österreich*, Band **41**, 65-73

RÖGL, F. and STEININGER, F.F. [1983] Vom Zerfall der Tethys zu Mediterran und Paratethys. Die neogene Paläogeographie und Palinspastik des zirkum-mediterranen Raumes. *Annalen des Naturhistorischen Museums in Wien*, Band **85**, Serie A, 135 -163

ROYDEN, L.H. [1985] The Vienna Basin: A thin-skinned pull-apart basin. In: BIDDLE, K.T. and CHRISTIEBLICK, N.: Strike slip deformation, basin formation and sedimentation. *Society of Economic Paleontologists and Mineralogists*, Special Publication **37**, 319-338

SAVIT, C. [1989] Seismic data acquisition*. The Leading Edge,* **8** (9), 14-18

SCHURR, B. [2007] Theorie seismischer Wellen. *lecture notes*

SHERIFF, R.E. [2002] Encyclopedic Dictionary of Applied Geophysics. *Society of Exploration Geophysicists*, Tulsa - Oklahoma, 384 pages

STEININGER, F.F., BERNOR, R.L. and FAHLBUSCH, V. [1990] European Neogene marine/continental Chronologie correlations. 15-46. In: LINDSAY, E.H., FAHLBUSCH, V.

& MEIN, P. (eds.): *European Neogene Mammal Chronology*. Plenum Press, New York, 658 pages

TELFORD, W.M., GELDARD, L.P. and SHERIFF, R.E. [1990] Applied Geophysics - Second Edition*. Cambridge University Press*, UK, 792 pages

THURBER, C.H. and KISSLING, E. [2000] Advances in Travel-Time Calculations for 3-D structures. 71-99. In: THURBER, C.H. and RABINOWITZ, N.: Advances in Seismic Event Location, *Kluwer Academic Publishers*, Dordrecht, NL, 276 pages

TSAVANKIN, I. and THOMSEN, L. [1994] Nonhyperbolic reflection moveout in anisotropic media. *Geophysics*, **59** (8), 1290-1304

VERMEER, G.J.O. [1998] 3-D symmetric sampling. *Geophysics*, **63** (5), 1629-1647

VERMEER, G.J.O. [2002] 3-D Seismic Survey Design. *Society of Exploration Geophysicists*, Tulsa - Oklahoma, 205 pages

VERMEER, G.J.O. [2003] 3D seismic survey design optimization. *The Leading Edge*, **22** (10), 934-941

VIDALE, J. [1988] Finite-difference calculation of travel times. *Bulletin of the Seismological Society of America*, **78** (6), 2062-2076

VIDALE, J. [1990] Finite-difference calculation of traveltimes in three dimensions. *Geophysics*, **55** (5), 521-526

WESSELY, G. [1988] Structure and Development of the Vienna Basin in Austria. In: ROYDEN, L.H. and HORVATH, F.: The Pannonian System - A study in basin evolution. *American Association of Petroleum Geologists Memoir*, **45**, Tulsa - Oklahoma.

WESSELY, G. [1999] Oil and Gas Occurrences of the Vienna Basin. *Berichte der Geologischen Bundesanstalt*, **49**, 20-21

WESSELY, G. [2006] Geologie der österreichischen Bundesländer - Niederösterreich. *Eigenverlag der Geologischen Bundesanstalt*, Wien, 416 pages

XIE, X.B. and YANG, H. [2008] A Full-wave Equation Based Seismic Illumination Analysis Method. *70th EAGE Conference & Exhibition - Rome*, Italy, 9 - 12 June

XIE, X.B., SHENGWEN, J. and RU-SHAN, W. [2006] Wave-equation-based seismic illumination analysis*. Geophysics*, **71** (5), 169-177

YANG, W. [2003] A Basical Study on Two-point Seismic Ray Tracing. http://www.ees.nmt.edu/Geop/Classes/GEOP523/Docs/yang.pdf, accessed on 16.01.2011

YILMAZ, Ö. [2001] Seismic Data Analysis Vol. I & II; *Society of Exploration Geophysicists*, Tulsa - Oklahoma, 2027 pages

MARTIN FUCHSLUGER

Knieberg 16
3341 Ybbsitz

+43 680 1419939
ma.fu@gmx.at

Personal Data

Date of Birth
31. January 1983

Nationality
Austria

Marital status
unmarried

Education

October 2005 - Spring 2011
Master's degree in Geophysics at the University of Vienna

1997 - 2002
Institution of higher education for electrical engineering, graduating with Matura (A-levels, graduation diploma) in Waidhofen/Ybbs

1989 - 1997
Elementary and secondary school in Ybbsitz

Military service / Alternative civilian service

February 2003 - January 2004
Civilian service at the Red Cross in Waidhofen/Ybbs with certification as a paramedic

Work experience before university

June 2004 - September 2005
Project handling engineer of electrical industry cabinets (switchboards), Siemens Elin Ebg Linz

February 2004 - March 2004
Call Center Agent, Telekom Austria Linz

August 2002 - January 2003
CAD engineer for special technical tools, Welser AG Ybbsitz

Work experience during the study

Service contract at the Geological Survey of Austria

Numerical simulation for the geothermal storage of solar thermal energy in the shallow soil

Research assistance at the Helmholtz Centre for Environmental Research in Leipzig

Electromagnetic induction and gamma spectroscopic measurements, script writing in PERL to correct GPS data

Service contract at OMV Exploration and Production

3D seismic acquisition design for the deep Vienna basin, practical part for the diploma thesis

Service contract at the Geological Survey of Austria

Implementation of geoelectrical measurements

Service contract for Steinhauser Erschütterungsschutz

Several seismic measurements for vibration and noise protection for railway tunnel projects in Austria

Diverse side jobs

Guest family manager for student exchange program, delivery services, janitor, event assistance

Special skills

Blaster's certificate of competence successfully completed at University of Natural Resources and Life Sciences, Vienna

Language skills

German (native)
English (good)
Spanish (basics)

Computer literacy

MS Windows and Office, C++, Perl, Fortran77, Matlab, AutoCAD, ProPlan, GoCAD, ArcGis, Omni, Surfer, Grapher, …

Private interests

paragliding, snowboarding, music